

University of Vermont

UVM ScholarWorks

Graduate College Dissertations and Theses

Dissertations and Theses

2014

Surface Gas Permeability of Porous Building Materials: Measurement, Analysis and Applications

David Klein Weibust Grover
University of Vermont

Follow this and additional works at: <https://scholarworks.uvm.edu/graddis>



Part of the [Environmental Engineering Commons](#), and the [Mechanics of Materials Commons](#)

Recommended Citation

Grover, David Klein Weibust, "Surface Gas Permeability of Porous Building Materials: Measurement, Analysis and Applications" (2014). *Graduate College Dissertations and Theses*. 266.
<https://scholarworks.uvm.edu/graddis/266>

This Thesis is brought to you for free and open access by the Dissertations and Theses at UVM ScholarWorks. It has been accepted for inclusion in Graduate College Dissertations and Theses by an authorized administrator of UVM ScholarWorks. For more information, please contact scholarworks@uvm.edu.

SURFACE GAS PERMEABILITY OF POROUS BUILDING MATERIALS:
MEASUREMENT, ANALYSIS AND APPLICATIONS

A Thesis Presented

by

David K. W. Grover

to

The Faculty of the Graduate College

of

The University of Vermont

In Partial Fulfillment of the Requirements
for the Degree of Master of Science
Specializing in Civil and Environmental Engineering

October, 2014

Accepted by the Faculty of the Graduate College, The University of Vermont, in partial fulfillment of the requirements for the degree of Master of Science, specializing in Civil and Environmental Engineering.

Thesis Examination Committee:

_____ **Advisor**
Donna M. Rizzo, Ph.D.

_____ **Co-Advisor**
Mandar M. Dewoolkar, Ph.D.

Eric M. Hernandez, Ph.D.

_____ **Chairperson**
Leslie A. Morrissey, Ph. D.

_____ **Dean, Graduate College**
Cynthia J. Forehand, Ph.D.

Date: May, 16, 2014

ABSTRACT

In many events affecting our civil infrastructure, such as contamination or weathering, it is likely that only the surfaces of the affected building materials will be available for non-destructive measurements. In this work, we describe and analyze surface gas permeability measurements on a variety of natural and engineered building materials using two types of relatively new, non-destructive surface permeameters. It is shown that the surface gas permeability measurements correlate well with each other and could provide rapid estimates of macroscopic gas permeability and degradation of materials due to weathering. It is hypothesized that surface permeability can be used to predict macroscopic wicking of water. The results indicated that macroscopic wicking correlated reasonably well with surface permeability measurements of uniform materials with low permeabilities such as sandstones and clay brick.

Key words: building materials, porous media, permeability, surface permeability, weathering, autocorrelation, geostatistics

ACKNOWLEDGEMENTS

A number of people have supported me throughout this research and deserve my gratitude for their help and influence. First, my advisors Donna Rizzo and Mandar Dewoolkar have guided and encouraged me throughout this process. Donna's enthusiasm for data and analysis has been influential on my view of the world and my professional pursuits. I would like to thank my committee members, Leslie Morrissey and Eric Hernandez for their comments on this research. I thank my parents and brother who have always encouraged me to follow my interests and to think critically about the world. Finally, I would like to thank my wife, Kristie Grover, for her care throughout this work and for inspiring me to be my best. This would not have been possible without her support.

TABLE OF CONTENTS

	Page
ACKNOWLEDGEMENTS	ii
LIST OF TABLES	v
LIST OF FIGURES	vi
CHAPTER 1: Motivation, objectives and literature review	1
1.1 Introduction	1
1.2 Research Objectives and Specific Work Tasks	2
1.3 Literature Review	3
1.4 Organization of Thesis	5
CHAPTER 2: Surface permeability of natural and engineered porous building materials	7
2.1 Abstract	7
2.2 Introduction	8
2.3 Study Materials	10
2.3.1 Natural Materials	11
2.3.2 Engineered Materials	12
2.4 Testing Methods	13
2.4.1 Surface gas permeability using AutoScan II	13
2.4.2 Surface gas permeability using TinyPerm II	16
2.4.3 Macroscopic gas permeability	17
2.4.4 Weathering Effects	18
2.5 Surface Permeability Results	19
2.5.1 AutoScan II Results	19
2.5.2 Surface Effects	24
2.5.3 Comparisons Across Specimens	24
2.6 Comparison of AutoScan II and TinyPerm II Results	26
2.7 Surface versus Macroscopic Permeability	27
2.8 Simulated Weathering Results	28
2.9 Conclusions and Discussion	30
2.10 Acknowledgments	31
2.11 References	31
2.12 Figures and Tables	35
CHAPTER 3: Water Transport in Building Materials: Examining the Relationship Between Macroscopic Wicking of Water and Surface Permeability ...	56
3.1 Abstract	56
3.2 Introduction	57
3.3 Materials	60

3.4 Testing Methods	61
3.4.1 AutoScan II Surface Gas Permeability	61
3.4.2 Macroscopic Wicking.....	62
3.5 Results	63
3.5.1 AutoScan II.....	63
3.5.2 Macroscopic Wicking.....	65
3.5.3 Correlations	66
3.6 Conclusions and Discussion	68
3.7 Works Cited.....	69
3.8 Figures and Tables.....	72
CHAPTER 4: Summary and Future Work.....	82
References	84

LIST OF TABLES

Table 2.1 Theoretical dataset and correlation of for lag = 4 mm.....	54
Table 3.1 Photographs and surface permeability of various building materials. Ten uniform specimens are shown on the left, and seven non-uniform specimens are shown on the right.	73
Table 3.3 Principal Components performed on permeability statistics	75
Table 3.4 Permeability heat map and principal components	77

LIST OF FIGURES

Figure 2.1 The laboratory (a) surface permeameter AutoScan II measuring surface gas permeability on multiple specimens, (b) permeability probe on a brick specimen, and (c) assumed flow path of injected gas (source: New England Research, 2008).	35
Figure 2.2 The (a) portable surface permeameter (TinyPerm II) and components used in this study (source: New England Research, 2008), and (b) example of the device being used in the field.	36
Figure 2.3 Measured surface gas permeability on a 152 mm x 240 mm 3,000psi concrete specimen at 4 mm grid spacing, (a) a photograph of specimen surface, (b) map of gas permeability field, (c) distribution of gas permeability along each y-coordinate, (d) gas permeability probability density function.	37
Figure 2.4 Measured surface gas permeability (a) and correlogram (b) of 3,000 psi concrete specimen along the transect $y = 84$ mm. The range = 36 mm.	38
Figure 2.5 Measured surface gas permeability (a) and correlogram (b) of 3,000 psi concrete specimen along the transect $x = 124$ mm. The range = 88 mm.	39
Figure 2.6 Global correlogram of 3,000 psi concrete specimen showing a geostatistical range of ~80 mm.	40
Figure 2.7 Measured surface gas permeability on a 70 mm diameter Ohio sandstone specimen at 2 mm grid spacing within the circular area shown as a dashed circle, (a) a photograph of the tested surface of the specimen, (b) map of gas permeability, (c) distribution of gas permeability along each y-coordinate, (d) probability density function of gas permeability.	41
Figure 2.8 Measured surface gas permeability (a) and correlogram (b) of Ohio sandstone specimen along the line $y = 24$ mm. The range = 30 mm.	42
Figure 2.9 Measured surface gas permeability (a) and correlogram (b) of Ohio sandstone specimen along the line $x = 24$ mm. The range = 12 mm.	43
Figure 2.10 Global correlogram of Ohio sandstone specimen showing a range of ~ 30 mm.	44
Figure 2.11 Measured surface gas permeability on a 45 mm thick Red Clay Brick over the surface area of 170 mm x 65 mm at 5 mm grid spacing, (a) a photograph of the tested surface of the specimen, (b) map of surface gas permeability, (c) distribution of surface gas permeability along each y-coordinate, (d) probability density function of gas permeability.	45
Figure 2.12 Measured surface gas permeability (a) and correlogram (b) of red clay brick specimen along the line $y = 45$ mm. The range = 22 mm.	46
Figure 2.13 Measured surface gas permeability and correlogram of red clay brick specimen along the line $x = 90$ mm. The range is not detected, i.e. 0.	47

Figure 2.14 Global correlogram of red clay brick specimen. The range = 20mm.....	48
Figure 2.15 Core (70 mm diameter) of 3,000 psi concrete specimen (a) Picture of screeded top, (b) picture of interior about 2 mm below screeded top, (c) surface gas permeability map of the screeded top, (d) surface gas permeability map of on the interior surface. White areas did not return a measurement	49
Figure 2.16 Photographs and surface permeability of various building materials. Ten uniform specimens are shown on the left, and seven non-uniform specimens are shown on the right.....	50
Figure 2.17 TinyPerm II averages (geometric mean) versus AutoScan II averages (geometric mean). Natural materials are shown as dark gray while engineered materials are show as light gray. Both data sets were \log_{10} transformed, and $R^2 = 0.94$	51
Figure 2.18 Macroscopic gas permeability plotted against geometric mean of surface gas permeability.....	52
Figure 2.19 Comparison of most probable permeabilities under unweathered and weathered conditions.....	53
Figure 3.1 Schematic of macroscopic wicking experiment setup.....	72
Figure 3.2 Mass of water wicked in grams over 50 minutes for all specimens.....	76
Figure 3.3 Multivariate linear prediction of mass Principal Component by permeability Principal Components, R^2 adjusted = 0.036, RMSE = 3.7	78
Figure 3.4 Prediction of mass wicked at 50 minutes by geometric mean of surface permeability for uniform, low permeability materials, $R^2 = 0.95$	79
Figure 3.5 Prediction of mass wicked at 50 minutes by geometric mean of surface permeability for non-uniform materials, $R^2 = 0.55$	80
Figure 3.6 Mass wicked at 50 minutes by geometric mean of surface permeability for all materials and their respective relationships	81

CHAPTER 1: MOTIVATION, OBJECTIVES AND LITERATURE REVIEW

1.1 Introduction

The built environment has been constructed from a variety of materials ranging in origin, reliability and upkeep requirements. The continuous functionality of many pieces of this infrastructure, such as dams, bridges and houses, are critical to the economy and the safety of human society. Others, such as historical monuments and buildings, are valued because of their cultural significance. These structures can suffer a variety of problems, both natural, e.g. extreme temperatures, weathering, and manmade, e.g. toxic contamination. Understanding the composition and condition of the materials that make up our built environment is an area of importance and continual research, especially in cases where building materials must be characterized *in situ* and require rapid decisions regarding whether to remediate or raze a structure.

This work examines two methods of nondestructive testing and characterization – surface gas permeability measurements using the AutoScan II and TinyPerm II permeameters. Specimens from a large variety of natural stone and engineered building materials are examined to understand each method's ability to characterize the surface permeability of these building materials. Surface permeability testing can be performed

in both the laboratory and the field. It can be automated to collect a large amount of data and used as a surrogate for other physical characteristics of materials. This thesis adds to the growing literature on surface permeability by exploring a wide variety of materials, examining metrics for characterizing permeability fields, and connecting surface permeability to other areas of research.

1.2 Research Objectives and Specific Work Tasks

The overall thesis objectives are to:

1. Analyze the surface gas permeability data collected using the AutoScan II permeameter and introduce geostatistical metrics of characterization into the materials literature,
2. Compare the laboratory AutoScan II permeameter results to that of the TinyPerm II, a handheld permeameter appropriate for field use, and
3. Examine the potential of the permeameters to rapidly and nondestructively determine macroscopic gas permeability, degree of weathering, and macroscopic wicking of building materials.

The specific work tasks are as follows:

1. I, along with another graduate student and two undergraduate research assistants, collected surface permeability readings at various sampling resolutions on a variety of natural and engineered porous building materials using the AutoScan II surface gas permeameter.

2. The materials studied were also subjected to TinyPerm II measurements, macroscopic gas permeability, simulated weathering experiments, and/or macroscopic wicking tests, with assistance of the two undergraduate researchers.
3. I introduced and used the concepts of geostatistics and spatial autocorrelation to provide detailed characterization of high-resolution surface permeability scans.
4. I examined relationships between the surface permeability testing results and the results of item 2 above, and reduced the large surface permeability datasets into a manageable set of characteristics.

1.3 Literature Review

Fluid transport through porous materials is an area of study relevant to many scientific and engineering disciplines such as hydrogeology, geoenvironmental engineering, petroleum engineering, chemical engineering, physics, biology and medicine (e.g. Dandekar, 2006; Dullien, 1992; Gladden et al., 2003; Jang et al., 2003; Steele and Heinzl, 2001).

Methods of measuring surface permeability through nondestructive means have been an active area of research for many decades (Dykstra and Parsons, 1950; Goggin and Thrasher, 1988). Non-destructive and cost-efficient mini or probe permeametry has become an important tool, providing fast data for both laboratory and *in situ* permeability measurements (Chandler et al., 1989; Davis et al., 1994; Dreyer et al., 1990; Dutton and Willis, 1998; Eijpe and Weber, 1971; Fossen et al., 2011; Goggin, 1993; Hornung and Aigner, 2002; Huysmansa et al., 2008; Sharp Jr. et al., 1994).

Selvadurai and Selvadurai (2010) estimate macroscopic water permeability of a limestone block using surface water permeability. Rogiers et al., (2013) used the surface permeability of outcrop sediments to improve their characterization of saturated hydraulic conductivity of an aquifer.

Surface gas permeameters have recently proven useful in characterizing and comparing porous building materials. Valek, et al. (2000) developed and applied a surface permeability probing method for historic conservation. The device was used to examine the difference in permeability of weathered versus cleaned historic sandstone masonry. Iversen et al. (2003) used a portable air permeameter to determine the variability of macroscopic air and water permeability of soils in the field. Filomena, et al. (2013) compared the results of two permeameter cells suitable for laboratory use with two minipermeameters suitable for the field. The former measured macroscopic gas permeability, while the latter measured surface gas permeability in sandstone. After applying corrections, macroscopic gas permeability and surface gas permeability were found to be strongly correlated. Zaharieva et al. (2003) used surface air permeability as a means of comparing recycled aggregate concrete to a control mix.

This study will add to the body of literature by characterizing additional building materials, relating surface permeability to macroscopic permeability, and examining the effects of simulated weathering across a broad range of materials.

Additionally, surface permeability may be related to macroscopic wicking in that both are related to pore size. Wicking is a relatively well-understood phenomenon,

caused by the capillary action between a fluid and the material walls within pore spaces. Washburn (1921) explains that, for a simplified system with small pore size and laminar flow conditions, the rate of wicking is a function of the capillary radius, among other attributes. This relationship was developed for straight tubes of constant diameter; although, it has also been used to inform research in irregular shaped tubes and beds of glass beads (Staples and Shaffer 2002). Küntz and Lavallée (2001) and Lockington and Parlange (2002) have refined the relationships related to porosity.

Depth of contaminant penetration in building materials is an active area of research. Navaz et al. (2008) investigate droplet spread in porous materials using a finite element analysis. Although mitigation of chemical warfare contamination motivates that research, they point out that the effects of wicking cover many diverse fields. Brownell et al. (2006) investigated a variety of properties on six building materials, with particular focus on the amount of water wicked over time. Anand et al. (2003) compared water absorption in conventional and alternative masonry systems; and Bentz et al. (2001) used it to predict degradation in concrete pavements.

1.4 Organization of Thesis

Chapter 1 introduces the topics of surface gas permeability and the other relevant testing procedures covered in the thesis. It ties these topics together to explain the overall goals of the investigations and presents the study aims and tasks performed to accomplish these aims. It also presents a literature review organized by testing methods.

Chapter 2, formatted as a journal article, presents the results and uses of surface gas permeability sampling. After introducing the AutoScan II permeameter testing apparatus, it examines each of three datasets in-depth and studies how to best characterize the surface permeability. Geostatistical analysis is introduced to examine the spatial autocorrelation of the resulting permeability fields. AutoScan II data are then compared with TinyPerm II measurements, macroscopic gas permeability, and simulated weathering to examine the utility of surface gas permeametry with building materials. Finally, the conclusions are summarized to show that surface gas permeability testing produces a rich dataset, correlates well with macroscopic gas permeability, and may provide a proxy for quantifying the degree of *in situ* weathering.

Chapter 3 examines the relationship between surface gas permeability readings and macroscopic wicking of water. The results indicated that macroscopic wicking correlated reasonably well with surface permeability measurements of uniform materials with low permeabilities such as sandstone, but not for non-uniform materials such as concretes. An overall model that governed both uniform and non-uniform materials was not found.

CHAPTER 2:

SURFACE PERMEABILITY OF NATURAL AND ENGINEERED POROUS BUILDING MATERIALS

2.1 Abstract

Porous building materials are omnipresent in civil infrastructure. Following contamination or weathering, it is likely that only the surfaces of the affected building materials will be available for non-destructive measurements. In this work, we describe and analyze surface gas permeability measurements on a variety of natural and engineered building materials using two types of relatively new, non-destructive surface permeameters. It is shown that the surface gas permeability measurements correlate well with each other and macroscopic gas permeability measurements. This work indicates that surface permeability measurements could provide reliable estimates of macroscopic gas permeability and help quantify degradation of materials from weathering.

Key words: building materials, porous media, permeability, surface permeability, weathering, autocorrelation, geostatistics

2.2 Introduction

Fluid transport through porous materials is an area of study relevant to many scientific and engineering disciplines such as hydrogeology, geoenvironmental engineering, petroleum engineering, chemical engineering, physics, biology and medicine (e.g. Dandekar, 2006; Dullien, 1992; Gladden et al., 2003; Jang et al., 2003; Steele and Heinzl, 2001). Knowledge of permeability and its spatial variability is critical to reliably predicting fluid transport. As a result, there is great interest in quantifying the aqueous and gaseous phases of permeability of natural and engineered porous materials for many practical applications such as water and oil extraction, subsurface contaminant transport, storing fluids in mined caverns for energy conservation, predicting leakage into tunnels, assessing durability, and decontamination of porous building materials from acid rain, toxic spills, and possible chemical and biological agent release, to name a few (Goodman, 1989; Paulini and Nasution, 2007; or Zaharieva, et al., 2002).

Following contamination, demolition is not always an option, especially for structures of historic and cultural significance and emergency facilities; and it is likely that only the surface of the building materials will be available for rapid response measurements and characterization. Therefore, understanding how rapid measurements of surface permeability relate to the macroscopic permeability, fluid transport and the durability of building materials is of great interest. This paper focuses on typical porous building materials including natural rocks (e.g., sandstones and limestones) and engineered materials (e.g. bricks and concrete).

Non-destructive and cost-efficient mini or probe permeametry has become an important tool, providing fast data for both laboratory and *in situ* permeability measurements (Chandler et al., 1989; Davis et al., 1994; Dreyer et al., 1990; Dutton and Willis, 1998; Eijpe and Weber, 1971; Fossen et al., 2011; Goggin, 1988; Goggin, 1993; Hornung and Aigner, 2002; Huysmansa et al., 2008; Iversen et al., 2003; Rogiers et al., 2011; Sharp Jr. et al., 1994). Valek, et al. (2000) developed and applied a surface permeability probing method for historic conservation. The device was used to examine the difference in permeability of weathered versus cleaned historic sandstone masonry. Filomena, et al. (2013) compared sandstone results using two permeameter cells suitable for laboratory measurement of macroscopic gas permeability with two minipermeameters suitable for measuring surface gas permeability in the field. After applying corrections, the two were found to be strongly correlated. However, studies comparing surface permeability with macroscopic permeability across a wide range of materials are not available in the literature. Similarly, studies comparing laboratory surface permeameters with those available for field measurements for a wide range of materials could not be found in the literature.

Every building material is porous to some degree and has inherent heterogeneities and potential anisotropy. Similarly, different specimens of the same material may exhibit different properties. Concrete is used more than any other engineered building material on the planet (Lomborg, 2000) making up one-half to two-thirds of our infrastructure. Although it is typically made of similar constituents, the constituent proportions, curing times, and pore structure may vary significantly

depending on the application. Many building materials such as concrete are regularly exposed to degradation processes that initiate along the surface; and the permeating properties have been recognized as useful for assessing the durability of concrete in construction engineering (e.g. Levitt, 1969; Figg, 1972; Zaharieva, et al., 2003).

In this chapter, we investigate a surface gas permeameter, called the AutoScan II, which is suitable for making laboratory measurements of surface gas permeability at sub-millimeter grid spacing. The resulting measurements are characterized using geostatistics. Particular attention is paid to identifying the specimens' range of spatial autocorrelation and anisotropy to identify transport pathway preferences and the best sample spacing for characterizing these specimens. Next, we characterize 17 specimens of natural and engineered porous building materials by measuring the surface gas permeability over a uniform square grid. Sixteen of these datasets are then compared to those collected with a different permeameter more suitable for field applications, the TinyPerm II. These two permeameters are unique in that they are non-destructive and capable of measuring a wide range of surface gas permeabilities. Next, we examine the relationship between surface permeability and macroscopic gas permeability over the 17 materials. Finally we examine the permeability of six building materials before and after simulated weathering to demonstrate that surface permeability measurements may be used to determine the extent of weathering.

2.3 Study Materials

This study includes natural (i.e., granite, sandstones, and limestones) and engineered materials (i.e., concretes, cement mortar, asphalt, and bricks). The majority

of the concretes and mortar mixtures were hand mixed until the ingredients were uniform, subsequently poured into cylindrical molds (70-78 mm in diameter) or small slabs, and moist cured for a minimum of 28 days, and in many cases much longer. All concrete surfaces were ‘finished’ by hand screeding (removing defects and creating a smooth, finished surface), as is typically done in practice. Cylindrical specimens of natural stone were cored from larger pieces of the stone. Cylindrical brick and paver specimens, and in some cases cylindrical concrete specimens, were cored from commercially available bricks and pavers or cured concrete slabs. In general, the cylindrical specimens were either 70 mm or 78 mm in diameter with heights varying from 40 to 100 mm.

Initial results revealed that natural weathering and the screeding process in concrete affect the surface permeability. Therefore, some specimens (i.e., the top and bottom screeded or weathered sections of the cores) were extracted from the cores. Specimens were cut with a water saw, (i.e., table saw fitted with a constant stream of water) to avoid overheating the specimen. Internal specimens extracted from cores are explicitly identified in the text.

2.3.1 Natural Materials

The *natural* materials examined in this study included: (1) Ohio Sandstone acquired from Granite Importers, Inc., (2) Arkose Sandstone acquired from Granite Importers, Inc., (3) Portland Brownstone acquired from Granite Importers, Inc., (4) Bluestone sandstone acquired from a local landscaping company, (5) Indiana

Limestone from the Indiana Limestone Company, (6) Indiana Limestone of differing colors from Granite Importers, Inc., and (7) Granite of unknown origin.

In some cases, materials of the same type but from different sources were tested; they are denoted as Specimen 1, Specimen 2, and so on.

2.3.2 Engineered Materials

The *engineered* materials examined in this study included: (1) Ready Mix Concrete by Quickrete, (2) 3,000-psi Concrete prepared in the lab, (3) 5,000-psi Concrete prepared in the lab, (4) D04 Concrete from the Idaho National Laboratory, (5) High Strength Concrete mix by Sakrete, (6) Portland Cement prepared in the lab, (7) Red Clay Brick from a Vermont brick yard, (8) Red Colored Concrete Paver from a hardware store, (9) Tan Colored Concrete Paver from a hardware store, (10) Concrete Paver from a hardware store, (11) Asphalt from a road excavation, and (12) Concrete of unknown origin.

The specific composition of some materials is unknown, although they were selected because they represent commonly used building materials. In some cases, the same type of materials from different batches or sources were tested; they are denoted as Specimen 1, Specimen 2, and so on. Concretes of a specified strength were prepared using a recipe for that particular strength, but the strengths were not confirmed through testing.

2.4 Testing Methods

Surface gas permeability was measured on specimens from the building materials listed above using two devices, AutoScan II and Tinyperm II. These surface gas permeability techniques are relatively new, so ASTM standards do not yet exist. These testing procedures are described in detail immediately below. In addition, macroscopic gas permeability was measured on a subset of the above specimens in general accordance to the ASTM D 4525-90 described in section 2.4.3. A different subset of the specimens were subjected to 30 water-saturated freeze-thaw cycles in general accordance with ASTM standards described in section 2.4.4 to assess the effects of weathering on surface permeability.

2.4.1 Surface gas permeability using AutoScan II

Fine-scale gas permeability was measured on specimen surfaces in a laboratory setting using a relatively new, automated surface gas permeameter apparatus AutoScan II (Figure 2.1a) developed by New England Research, Inc., located in White River Junction, VT. The user selects the sample measurement locations along an x-y grid as well as target pressure and flow rates. The rest of the process is automated; measurement data are stored in the computer system. The measurement spacing can be as small as 0.1 mm. The device is capable of measuring permeability that ranges from 0.1 milliDarcy ($9.87 \times 10^{-17} \text{ m}^2$) to 3 Darcy ($2.96 \times 10^{-12} \text{ m}^2$) (New England Research, Inc., 2008) and can be programmed to test multiple specimens in a single run. The permeability probe (Figure 2.1b) has a tip seal made of soft rubber that is pressed

against the specimen at the desired sampling locations and prevents leakage between the probe and the sample surface. Pressurized gas flows down through the specimen surface. Nitrogen gas was used in this work per the manufacturer’s recommendation. The gas is assumed to flow through the specimen to the atmosphere in a roughly hemispherical geometry as depicted in Figure 2.1c. Once steady-state flow is achieved, Darcy’s law is assumed to be valid and the surface gas permeability is computed using the following equation (neglecting gas slippage and high velocity flow effects):

$$K_{apparent} = \frac{2Q\mu P_{atm}}{aG_o(P^2 - P_{atm}^2)}, \quad (2.1)$$

where,

$K_{apparent}$ = apparent permeability (L^2),

Q = flow rate of gas at P_{atm} (L^3/T),

μ = gas viscosity (M/LT),

P = injection pressure of the gas (M/LT^2),

P_{atm} = atmospheric pressure (M/LT^2),

a = internal tip-seal radius (L), and

G_o = geometrical factor (unitless).

For this work, the manufacturer’s default settings were used. The gas viscosity was 1.78×10^{-5} Pa·s, internal tip-seal radius of 0.005 m, and a geometrical factor of 0.0059. The AutoScan II will vary the gas injection pressure (P) and the flow rate (Q) during a sample reading until they reach steady state and then determine the $K_{apparent}$. The user can change the initial P and Q to bring the reading to steady state more

quickly. The user can also specify a maximum time for a sample reading, and the device will not return a reading for that sample point if steady state is not reached in the amount of time allotted. In some cases, where permeability varied greatly across one specimen, the initial P and Q values did not enable readings at many sample points before the reading timed out. In these cases, the specimen was rerun with different initial P and Q values. In cases where the same point was sampled in multiple runs, the earliest sample reading was selected for subsequent analysis.

The apparent permeability is then corrected for gas slippage and high velocity flow effects at low gas injection pressures and high gas flow rates, respectively. The corrected permeability, K_k , for the gas slippage effect is:

$$K_k = \frac{K_{apparent}}{1 + \left(\frac{B}{P_{mean}} \right)}, \quad (2.2)$$

where B is the Klinkenberg slip factor and P_{mean} is the mean measurement pressure $P_{mean} = (P + P_{atm})/2$ (Klinkenberg, 1941).

The actual permeability, K_o , is further corrected for high velocity flow effects using:

$$\frac{1.0}{K_o} = \frac{1.0}{K_k} - F_h \cdot Q, \quad (2.3)$$

where K_k is the permeability obtained from equation (2.2), and K_o is the actual permeability that has been corrected for turbulence and inertial effects (Goggin, et al., 1988). Although the surface permeameter allows the user to adjust both the

Klinkenberg (B) and the Forchheimers (F_h) parameters, these parameters were not adjusted in this work, and the manufacture's defaults were used.

2.4.2 Surface gas permeability using TinyPerm II

The surface gas permeability was also measured using the TinyPerm II developed by New England Research, Inc., located in White River Junction, VT. This handheld (~1.2 kg, 38cm x 12.5cm x 5cm), portable device (Figure 2.2a) measures surface permeability in a field (Figure 2.2b) or laboratory setting. This device has been used by other researchers, e.g. Rogiers, et al. (2013) on soils and Filomena, et al. (2013) on sandstone. The rubber nozzle at the end of the device is pressed against the specimen to form an airtight seal. The operator then pushes the end of the syringe toward the specimen, which creates a vacuum by removing air from the sample. By monitoring the syringe volume and the vacuum pulse at the specimen surface, the TinyPerm II calculates a characteristic value (T) that is related to the gas permeability (K in milliDarcy) per the following manufacturer's equation:

$$K = 10^{\left(\frac{12.8737-T}{0.8206}\right)}. \quad (2.4)$$

Typical T values range between 12.5 and 9.5 yielding permeability measurements between 2 milliDarcy ($1.97 \times 10^{-15} \text{ m}^2$) and 10 Darcy ($9.87 \times 10^{-12} \text{ m}^2$), respectively (New England Research, Inc., 2008). A permeability reading of 10 milliDarcy ($9.87 \times 10^{-15} \text{ m}^2$), the manufacturer's recommended lower limit, takes about five minutes, and materials with smaller permeabilities typically will require longer measurement times. Some materials in this study had measured permeabilities of less

than 10 milliDarcy; testing times for these materials were found to be time consuming and, at times, upwards of 30 minutes. For these specimens, the TinyPerm II would be wedged in place to avoid arm fatigue. Because these measurements are below the manufacture's recommended lower limit, the accuracy and usefulness of these lower readings and their increased measurement times are discussed later.

Of the 17 specimens tested with AutoScan II at 1 mm grid spacing, 16 were re-sampled using the TinyPerm II, which is well suited for field use. The 3,000 psi concrete was not tested with the Tinyperm II due to its low permeability. Typically 23 readings were taken on the specimen surface with the exception of the two specimens with exceptionally low permeability (i.e. granite and bluestone have only 12 readings). This is compared with the 1,296 points measured with AutoScan II. Given the large range in measurement values collected with both the TinyPerm II and AutoScan II, data in graphical form are often transformed using a base-10 logarithm. However, all statistics were performed on the raw, i.e. not transformed, measurements. The geometric mean of the AutoScan II and the TinyPerm II measurements is used to characterize the specimens to avoid the effects of aberrant readings.

2.4.3 Macroscopic gas permeability

The macroscopic gas permeability was measured in accordance with ASTM D4525-90: Standard Test Method for Permeability of Rocks by Flowing Air (ASTM International, 2002). The Wykeham Farrance permeability cell was used with two identical pressure transducers measuring the pressure drop across the specimen. A high

confining pressure (~275 kPa) was applied to the cell to ensure the air would pass through and not between the specimen and the latex membrane encasing it. A regulated supply of compressed air was applied to the specimen, while the exiting airflow was measured with a calibrated bubble-flow meter. The gas permeability was calculated as follows:

$$K = \frac{2Q_e P_e \mu L}{(P_i^2 - P_e^2) A}, \quad (2.5)$$

where,

K = coefficient of permeability (L^2),

Q_e = exit flow rate of air (L^3/T),

P_e = exit pressure of air (M/LT^2),

μ = viscosity of air at temperature of test (M/LT),

L = length of specimen (L),

P_i = entrance pressure of air (M/LT^2), and

A = cross-sectional area of specimen (L^2).

Macroscopic permeability of each specimen was measured five times, with the average reported as the measured macroscopic gas permeability for that specimen.

2.4.4 Weathering Effects

Five specimens from each of nine materials (n = 45 specimens) were subjected to accelerated weathering of 30 freeze-thaw cycles (-24°C and 20°C) submerged in water within a mechanical refrigeration chamber in general accordance with ASTM C666-97. Specimens were placed at random locations within the chamber and relocated

between cycles to reduce the effects of placement within the freeze-thaw chamber. All specimens were approximately 75 mm in diameter and 65-100 mm in height. Surface gas permeability was measured using AutoScan II before and after weathering using 3 mm grid spacing.

2.5 Surface Permeability Results

Surface gas permeability measurements were collected for a variety of specimens and at a variety of spatial resolutions to demonstrate the versatility and comparability of the AutoScan II and TinyPerm II in characterizing a broad range of natural and engineered building materials.

2.5.1 AutoScan II Results

The results of sampling 17 specimens at 1 mm grid spacing are presented to demonstrate the capability of, and type of data obtained from, the AutoScan II. Three specimens are investigated at high spatial resolution to characterize the spatial structure (i.e., identify the spatial autocorrelation and anisotropy) as well as the optimal spacing of the materials. Finally, surface effects are investigated by comparing the permeability at the surface to the permeability just below the surface.

3,000 psi Concrete

Surface gas permeability was measured along one side of a 260 mm x 180 mm x 75 mm slab of 3,000 psi concrete (Figure 2.3a). The measurement grid was 240 mm by 152 mm with 4 mm spacing, resulting in a total of 2,331 gas permeability

measurements in mD (milliDarcy) in Figure 2.3b (white squares indicate no reading). The same data are plotted in Figure 2.3c, where the permeability measurements for a particular y-coordinate are distributed along the horizontal axis. Figure 2.3d shows the probability density function (pdf) of the specimen's permeability with the peak (most observed value) at approximately 40 mD.

For this research, the peak of the pdf, i.e. the value most likely to be observed, is often used to globally characterize the data. Unlike the arithmetic mean, it is not influenced by aberrant values. This statistic is best for distributions with a single, identifiable peak and may be less appropriate for a dataset whose pdf is relatively flat, contains multiple peaks, or is spread over many orders of magnitude.

Surface permeability readings are generally between 10 and 80 mD, with a few points outside this range. The lowest values are located in the lower-middle portion of the specimen. The most observed value, 40 mD, is close to the arithmetic mean, 42.89 mD, geometric mean, 40.21 mD, and the median, 42.90 mD. The maximum, minimum, and standard deviation are 166.95 mD, 7.6 mD, and 15.2 mD, respectively.

These “global-scale” statistics do not characterize the local spatial distribution, autocorrelation, or anisotropy of the material. To summarize this type of variability, geostatistics were employed. The permeability field of Figure 2.3b suggests that measurements close to each other are more likely to have a similar value than measurements further apart, i.e. the points are autocorrelated in space. The semivariogram or correlogram captures the distance at which points are no longer autocorrelated; this distance is called the range.

Figure 2.4a plots the surface permeability values measured along the horizontal dashed transect $y=84$ of Figure 2.3b. As expected, points closer in space are more similar. To create the correlogram (Figure 2.4b), all data pairs are assigned to bins based on their spatial separation, also called a lag. For example, a spatial lag of 4 mm in the horizontal direction would pair a measurement value, termed the tail, with a measurement 4 mm to the right, called the head (e.g., a tail (24.5 mD) at 20 mm would have a corresponding head (22.0 mD) at 24 mm). Similarly, a tail located at 24 mm would have a head (20.4 mD) at 28 mm, and a tail (67.7 mD) at 88 mm has a head (72.6 mD) at 92 mm. All measurement pairs with similar lags are binned together and the correlation of the tails to the heads is calculated. If the above were the only point pairs that were 4 mm apart, then the permeability dataset for a horizontal lag = 4 mm would be as shown in Table 2.1, and the correlation for lag = 4 mm would be 0.9998 indicating that measurements separated in the horizontal direction by 4 mm are highly correlated. The correlation may also be calculated for paired data (i.e., heads and tails) at other lag distances, and, finally, these correlations may be plotted against their corresponding lags (i.e., separation distances) creating what is known as a correlogram. The range is defined as the distance on the correlogram at which measurements are no longer autocorrelated. Some correlograms have multiple ranges. See Isaaks and Srivastava, 1989; Goovaerts, 1998 for a detailed discussion of geostatistics.

Figure 2.4b shows the correlogram for the data in Figure 2.4a. Measurements at points close to each other are highly correlated and become less correlated (-0.499) as the distance increases up to a lag of 36 mm (i.e., the range). In this particular specimen,

the spatial autocorrelation begins to increase again after the first range of ~32 mm, and the correlogram is sinusoidal with a period of approximately 72 mm.

Graphs in Figure 2.5 are produced in a similar manner to Figure 2.4 except the data are sampled along the vertical transect $x=124$ mm in Figure 2.3b. The vertical range is 88 mm, and it appears that the surface permeability autocorrelation varies in a regular, cyclical pattern in the direction of the x-axis but not in the direction of the y-axis. The correlogram for all data points with lags in all directions (omni-directional correlogram of Figure 2.6) shows a global range of about 80 mm.

The correlogram and the range are useful in characterizing specimens. Repeating this geostatistical analysis along multiple transects would further confirm the directional dependence of the autocorrelation, known as anisotropy, across the entire specimen. This exercise has also shown that, when examining the specimen as a whole (Figure 2.6), measurements beyond a range of ~80 mm are generally not spatially autocorrelated; but this may not hold when only looking at points along a single transect. Yfantis et al. (1987) recommend a maximum sampling interval be approximately equal to the geostatistical range, so the distance between sample points should be on the order of 80 mm or less for this specimen.

Ohio Sandstone

The permeability of a 70 mm diameter Ohio sandstone core (Figure 2.7a) was measured over a 50 mm circular area with 2 mm grid spacing (Figure 2.7b). The distribution of permeability about the y-axis and the pdf are presented in panels c and d, respectively. The pdf peak is easily identified at 63 mD. Lower permeabilities in the

40s and 50s mD are located in the lower-right area of the surface, but most of the measurements are distributed between 60 and 90 mD.

Figures 2.8 – 2.10 display the geostatistical analysis associated with the Ohio sandstone specimen in a manner similar to the 3,000 psi concrete specimen. Again, the permeability measurements exhibit directional spatial autocorrelation. The readings appear more variable in the y-direction. This is reflected in the longer range of spatial autocorrelation (range = 30 mm) on the x-axis compared with the 12 mm range which oscillates along the y-axis. The global correlogram shows a steep decline to a lag of about 10 mm and then a more gradual decline until reaching its range at 30 mm.

Red Clay Brick

The red clay brick specimen (Figure 2.11) is more heterogeneous than the previous two specimens. Measured permeability values span over 3 orders of magnitude, so permeability readings have been transformed by log base-10. Furthermore, there appears to be less spatial autocorrelation between the permeability readings compared with the two previous specimens. All three correlograms (Figures 2.12-2.14) quantify this lack of spatial autocorrelation. Figure 2.12b shows less pronounced signs of an oscillating correlation with a range of 20 mm, but the largest correlation is lower (<0.5) than the other specimens. Similarly, the global correlogram shows a range of 20 mm, but the largest correlation is only about 0.12. Figure 2.13b shows no spatial autocorrelation. Measurements were spaced 5 mm apart on this specimen, so it is possible that stronger autocorrelation could be detected with smaller

spacing. Along the y-axis, the range of this specimen may be less than the grid spacing, and therefore, undetected by the correlogram.

2.5.2 Surface Effects

The relationship between the permeability of the screeded concrete surface (Figure 2.15a) and the interior surface ~2 mm below the screeded top (Figure 2.15b) was investigated on a 70 mm core of 3,000 psi concrete. The $\log_{10}(\text{mD})$ permeability fields of each surface (Figures 2.15c and 2.15d, respectively) were measured over a 35mm x 35 mm grid with 0.5 mm spacing.

Both the screeded surface and the interior surface show similar patterns (i.e., less permeable islands surrounded by thinner, more permeable threads). While the emerging shapes suggest similar patterns of permeability, the magnitudes of the values differ. Most notable is that the surface permeability measurements (Figure 2.15c) made on the screeded surface are approximately one order of magnitude greater than the surface permeability measurements of the interior surface (Figure 2.15d), despite the consistency in spatial patterns. The presence of aggregates near the measurement surface probably limited the ability of the gas to pass directly through the specimen from entry to exit point, which may cause deviations from the assumed hemispherical flow path (Figure 2.1c) resulting in smaller permeability.

2.5.3 Comparisons Across Specimens

The AutoScan II was used to characterize 17 different cored specimens using a consistent 35 mm x 35 mm grid with 1 mm spacing. All cores were extracted from the

middle of their specimens, which eliminated surface manifestations such as the process of screeding. These specimens are different than those listed previously, even in the cases where the specimens share the same parent material. Table 2.2 summarizes the measurement results along with global statistics used to characterize the materials; and Figure 2.16 shows a photograph of each specimen and a map of its surface permeability. The range and sill (another geostatistic) were found using semivariograms rather than correlograms (see Isaaks and Srivastava, 1989; Goovaerts, 1998). The data range over more than five orders of magnitude, which can make comparing the results difficult. All statistics in Table 2.2 were performed on the raw data; however, all permeability maps use the same $\log_{10}(\text{mD})$ color scale (bottom of Figure 2.16) for comparison, where dark blue is less than 1 mD and dark red is greater than 100,000 mD. Sample points that did not return a reading are shown in white.

The specimens show a variety of permeability readings ranging from less than 1 mD to over 140,000 mD. Granite is the least permeable with a geometric mean of 0.76 mD, and the red colored brick paver is the most permeable overall with a geometric mean of 23,689 mD. Asphalt has the largest number of missing measurements, likely due to the many holes and air pockets on the surface.

It should be noted that categorization of the global surface permeability may be related, in part, to whether the material is natural or engineered. The four most permeable materials are all engineered and not designed for strength. Most of the natural materials have very low permeabilities, as do the two concretes specifically cured for specified strengths. The 5,000 psi concrete specimen does show a small circle

of highly permeability readings, and this may be indicative of an indentation along the surface.

Global statistics reported are the arithmetic mean (mD), geometric mean (mD), most probable (pdf peak in mD), maximum (mD), minimum (mD), standard deviation (mD), range (mm), and sill (mD^2). The first five statistics are commonly used throughout the literature. As explained in detail above, the range is the distance at which measurements are no longer spatially autocorrelated. Non-uniform specimens with less variability have a larger range (e.g., asphalt is more non-uniform and has the smallest range (4.44 mm), while red clay brick is uniform and has the largest range (45.10 mm) of these 17 specimens). The sill is the variance between paired measurements that are not spatially autocorrelated (i.e., separated by distances larger than the range). The materials have also been categorized as natural or engineered and uniform (i.e. without aggregate) or non-uniform (i.e. containing aggregates).

2.6 Comparison of AutoScan II and TinyPerm II Results

To investigate how well the TinyPerm II can characterize a specimen in the field compared to the AutoScan II laboratory measurements, the averaged (geometric mean) TinyPerm II measurements for each specimen are plotted against their specimens' respective averaged (geometric mean) AutoScan II permeability values (Figure 2.17). The 1:1 line, $y=x$, is provided for comparison. The two values are highly correlated with the adjusted R^2 of 0.94 suggesting, that overall, the global permeability measurements on specimens using each of the devices are very similar.

As noted above, the TinyPerm II manufacturer recommends the device for specimens with a surface permeability greater than 10 mD, yet many of the measurements were below that threshold and required measurement times longer than five minutes. Our results show overall characterization of the specimen to be accurate below the manufacturer's recommended 10 mD, so the limiting factor when characterizing low permeability materials is the time required to perform sampling and not the accuracy of the measurements themselves.

2.7 Surface versus Macroscopic Permeability

Macroscopic gas permeability is plotted against surface gas permeability for 15 materials (see the legend of Figure 2.18). Four specimens were cored from each material resulting in 60 specimens tested. The geometric mean was used to characterize the AutoScan II surface permeability of each specimen, and the average of the four specimens for each material is plotted against the average geometric mean of macroscopic permeability in Figure 2.18 with a one-to-one line and the least-squared regression model. Note that the \log_{10} transform was applied to all data, and that the adjusted R^2 of 0.61 was computed using the $n=60$ values for each specimen. The solid, horizontal lines indicate the range of the four most probable surface gas permeability values for each material, while the vertical dashed lines indicate the range of the macroscopic gas permeability measurements associated with that material. The latter are within one order of magnitude of each other, with the exception of 3,000 psi concrete, which spans almost two orders of magnitude. Natural materials are plotted with dark lines while engineered materials are plotted with light gray shapes.

The natural materials (Ohio sandstone, Arkose sandstones, Indiana limestone), red clay brick and Portland cement, are made up of relatively homogeneous materials and plot close to the one-to-one line, indicating that differences between the surface and macroscopic gas permeability measurements are relatively small.

The remaining materials all fairly non-uniform (at least compared to the size of the specimens) man-made materials (ready mix concrete, 3,000 psi concrete, 5,000 psi concrete, D04 concrete, and red colored brick paver), and contain aggregates. These plot further from the one-to-one line, suggesting that the entire specimen permeability is somewhat different than that on the specimen surface. Given that the concrete specimen surfaces were smoothed and finished with the screeding process while the interior is a heterogeneous mixture, the interior aggregates likely create a longer and more tortuous flow path in macroscopic permeability measurements resulting in the smaller observed values of macroscopic permeability.

With the exception of the Arkose sandstone 2 and clay brick, all other materials had greater surface gas permeability measurements than macroscopic permeability measurements. This bias is likely due to the more tortuous flow path through the entire specimen.

2.8 Simulated Weathering Results

Surface permeability was tested before and after simulated weathering. Initially five specimens were cored from nine different materials for a total of 45 specimens to be tested. However, after weathering, specimens from three materials were degraded to

the point where they were unable to be tested. Thus, only specimens from the six materials still fairly intact after weathering are presented.

Figure 2.19 shows a scatter plot of most probable values with unweathered specimens on the x-axis and weathered specimens on the y-axis; a 1:1 line is shown for comparison. The natural materials (Indiana Limestone and Arkose Sandstone) are depicted with the black symbols x and +, respectively, while the engineered materials (ready mix, 5,000 psi concrete, high strength concrete, and red colored brick paver) are depicted with gray shapes. The natural materials both fall on or close to the 1:1 line. The ready mix is also close to the 1:1 line, but not as close as the natural materials. The other specimens are all substantially above the 1:1 line indicating their surface permeability has increased with weathering. It is hypothesized that the weathering process increased the size of the pores in the specimens or generated cracks, increasing the amount of air that could flow through the specimen. Consequently, the materials were found to have higher surface permeability after weathering, i.e. plot above the 45-degree line.

The natural materials were much less affected by weathering than the engineered materials. This robustness to weathering may be due to the extended period of time involved in their formation compared to the relatively quick cure time of engineered materials. The heterogeneous materials were also more affected than the more homogeneous. It is important to note that the 5,000 psi concrete had similar surface permeability to the natural materials before weathering, so unweathered surface permeability is probably not an indicator of resistance to weathering effects.

2.9 Conclusions and Discussion

Surface permeability has been shown to be a non-destructive method of characterizing porous building materials both in the laboratory and in the field. Automated collection and small measurement grid spacing make this technique useful for characterizing specimen surfaces in detail and comparing surface characteristics (e.g. geometric mean, most probable, maximum, and minimum values) across specimens. Geostatistics are particularly well suited for characterizing the spatial autocorrelation in a material as well as the anisotropy. Knowing the latter is indicative of preferential flow paths and knowing the range of spatial autocorrelation can be particularly useful in the field since the maximum distance between measurements should approximately equal the range for accurate material characterization. The TinyPerm II is well suited to field use, and it may provide a way to rapidly characterize materials *in situ*.

In general, the measured permeabilities (surface and macroscopic) compared better to each other for the relatively uniform materials (natural stones, clay brick and cement) tested in this study than the more non-uniform engineered materials such as concretes. For such materials, the surface permeability differed significantly from the macroscopic permeability. Surface permeability may be easier to measure *in situ*, but it may not be an appropriate surrogate for macroscopic gas permeability in all situations.

The surface permeability measurements are useful in quantifying relative changes on the exposed surfaces of porous building materials from effects such as weathering. If the additional weathering is indicative of reduced strength of the

materials, characterizing a change in surface permeability might be used as an indicator of a material's strength/durability over time, especially in harsh climates. These measurements illustrate the operational usefulness of the surface permeability measurement techniques, which is particularly relevant for investigations involving surface effects.

2.10 Acknowledgments

This work was funded through the Defense Threat Reduction Agency, which is gratefully acknowledged.

2.11 References

- [1] ASTM International. (2002), Annual Book of ASTM Standards: section four, volume 04.08. Soil and Rock (I).
- [2] Chandler, M. A., Goggin, D. J., and Lake, L. W. (1989) A mechanical field permeameter for making rapid, non-destructive, permeability measurements, *J. Sediment. Petrol.*, 59, 613–615.
- [3] Dandekar, A. Y. (2006), *Petroleum reservoir rock and fluid properties*. CRC Press, 496. ISBN 0849330432.
- [4] Davis, J. M., Wilson, J. L., and Phillips, F. M. (1994) A portable air-minipermeameter for rapid in situ field measurements, *Ground Water*, 32, 258–266.
- [5] Dreyer, T., Scheie, A., and Jensen, J. L. (1990) Minipermeameter-based study of permeability trends in channel sand bodies, *AAPG Bull.*, 74, 359–374.

- [6] Dullien, F. A. L. (1992), *Porous Media Fluid Transport and Pore Structure*, 2nd ed. Academic Press, 574. ISBN 0122236505.
- [7] Dutton, S. P. and Willis, B. J. (1998) Comparison of outcrop and subsurface sandstone permeability distribution, Lower Cretaceous Fall River Formation, South Dakota and Wyoming, *J. Sediment. Res.*, 68, 890–900.
- [8] Eijpe, R. and Weber, K. J. (1971) Mini-permeameters for consolidated rock and unconsolidated sand, *AAPG Bull.*, 55, 307–309.
- [9] Figg J. W. (1972). Determining the water content of concrete panels. *Magazine of Concrete Research*. 24(79): 94-96.
- [10] Filomena, C. M., J. Hornung, and H. Stollhofen (2013) Assessing accuracy of gas-driven permeability measurements: a comparative study of diverse Hassler-cell and probe permeameter devices, *Solid Earth Discuss.*, 5, 1163–1190.
- [11] Fossen, H., Schultz, R. A., and Torabi, A. (2011) Conditions and implications for compaction band formation in the Navajo Sandstone, Utah, *J. Struct. Geol.*, 33, 1477–1490.
- [12] Gladden, L. F., M. H. M. Lim, M. D. Mantle, A.J. Sederman, and E. H. Stitt (2003), MRI visualization of two-phase flow in structured supports and trickle-bed reactors, *Catalysis Today* 79, doi:10.1016/S0920-5861(03)00006-3.
- [13] Goggin, D. J. (1993) Probe permeametry: is it worth the effort?, *Mar. Petrol. Geol.*, 10, 299–308.

- [14] Goggin, D.J., R.L. Thrasher, and L. W. Lake (1988), A theoretical and experimental analysis of minipermeameter response including gas slippage and high velocity flow effects, *In Situ*, 12, 79-116.
- [15] Goovaerts, P., (1998) Geostatistical tools for characterizing the spatial variability of microbiological and physico-chemical soil properties *Biol Fertil Soils*, 27: 315–334.
- [16] Hornung, J. and Aigner, T. (2002) Reservoir architecture in a terminal alluvial plain: an outcrop analogue study (Upper Triassic, Southern Germany). Part 1: Sedimentology and petrophysics, *J. Petrol. Geol.*, 2, 3–30.
- [17] Huysmansa, M., Peetersa, L., Moermansa, G., and Dassarguesa, A. (2008) Relating small-scale sedimentary structures and permeability in a cross-bedded aquifer, *J. Hydrol.*, 361, 41–51.
- [18] Isaaks, E. H. and Srivastava, R. M. (1989), *Introduction to applied geostatistics*, Oxford Press, New York, 561 pp.
- [19] Iversen, Bo V., P. Moldrup, P. Schjønning, and O. H. Jacobsen (2003) Field Application of a Portable Air Permeameter to Characterize Spatial Variability in Air and Water Permeability, *Vadose Zone Journal* 2:618–626.
- [20] Jang, S. H., M. G. Wientjes, D. Lu, and L. S. A. Jessie (2003), Drug delivery and transport to solid tumors, *Pharmaceutical Research*, 20 (9), 1337-1350.
- [21] Klinkenberg, L. J. (1941), The permeability of porous media to liquids and gases, *Drilling and Productions Practices*, 200-213.

- [22] Lomborg, Bjørn (2000). *The Skeptical Environmentalist: Measuring the Real State of the World*. Cambridge University Press, 138. ISBN 0521804477.
- [23] New England Research, Inc., (2008), *AutoScan Automatic Multi-Sample Measurement Platform; Gas Permeability manual*.
- [24] Paulini, P., and F. Nasution (2007), *Air Permeability of near-surface concrete, Consec '07 Tours, France*, 8pp.
- [25] Rogiers, B., Beerten, K., Smeeckens, T., and Mallants, D. (2011) *Air permeability measurements on Neogene and Quaternary sediments from the Campine area: using outcrop analogues for determining hydrodynamic aquifer properties*, Belgian Nuclear Research Center, Mol, Belgium, External Report SCKCEN-ER-177.
- [26] Sharp Jr., J. M., Fu, L., Cortez, P., and Wheeler, E. (1994) *An electronic minipermeameter for use in the field and laboratory*, *Ground Water*, 32, 41–46.
- [27] Steele, B. C. H., and A. Heinzl (2001), *Materials for fuel-cell technologies*, *Nature*, 414, 345-352.
- [28] Valek, J., J. J. Hughes and P. J. M. Bartos, (2000), *Portable probe gas permeability: a non-destructive test for the in-situ characterization of historic masonry*, *Mat. and Struc.*, 33, 194-197.
- [29] Zaharieva, R., B.B. François, S. Frederic and E. Wirquin (2003), *Assessment of the surface permeation properties of recycled aggregate concrete*, *Cement & Concrete Composites*, 25, 223-232.

2.12 Figures and Tables

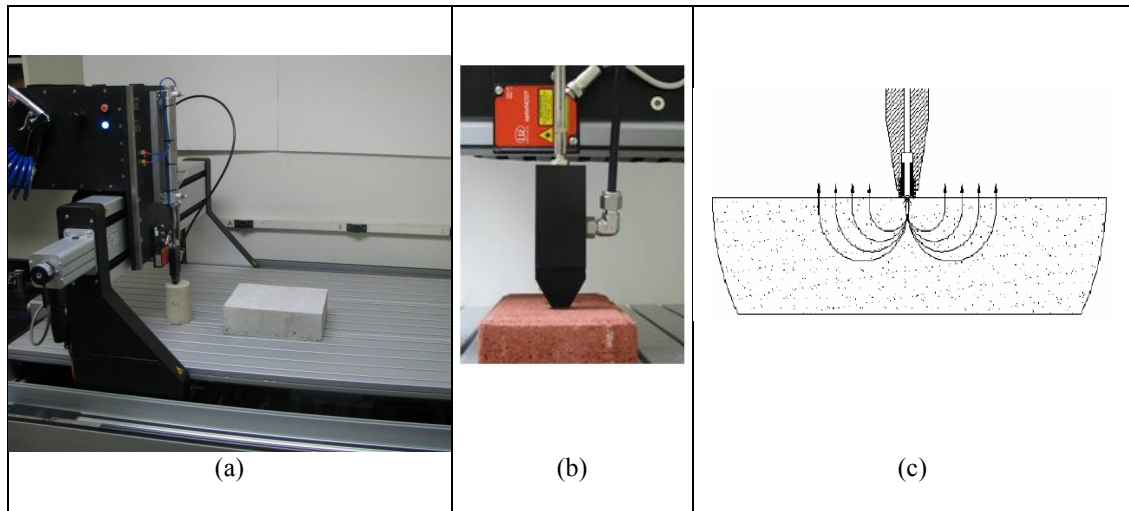


Figure 2.1 The laboratory (a) surface permeameter AutoScan II measuring surface gas permeability on multiple specimens, (b) permeability probe on a brick specimen, and (c) assumed flow path of injected gas (source: New England Research, 2008).

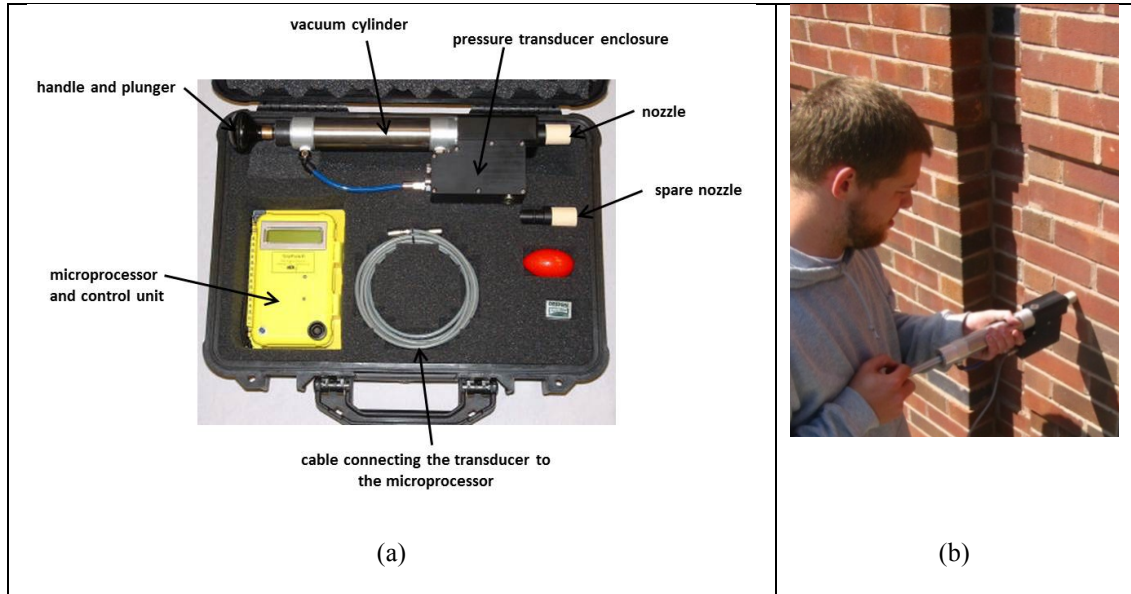


Figure 2.2 The (a) portable surface permeameter (TinyPerm II) and components used in this study (source: New England Research, 2008), and (b) example of the device being used in the field.

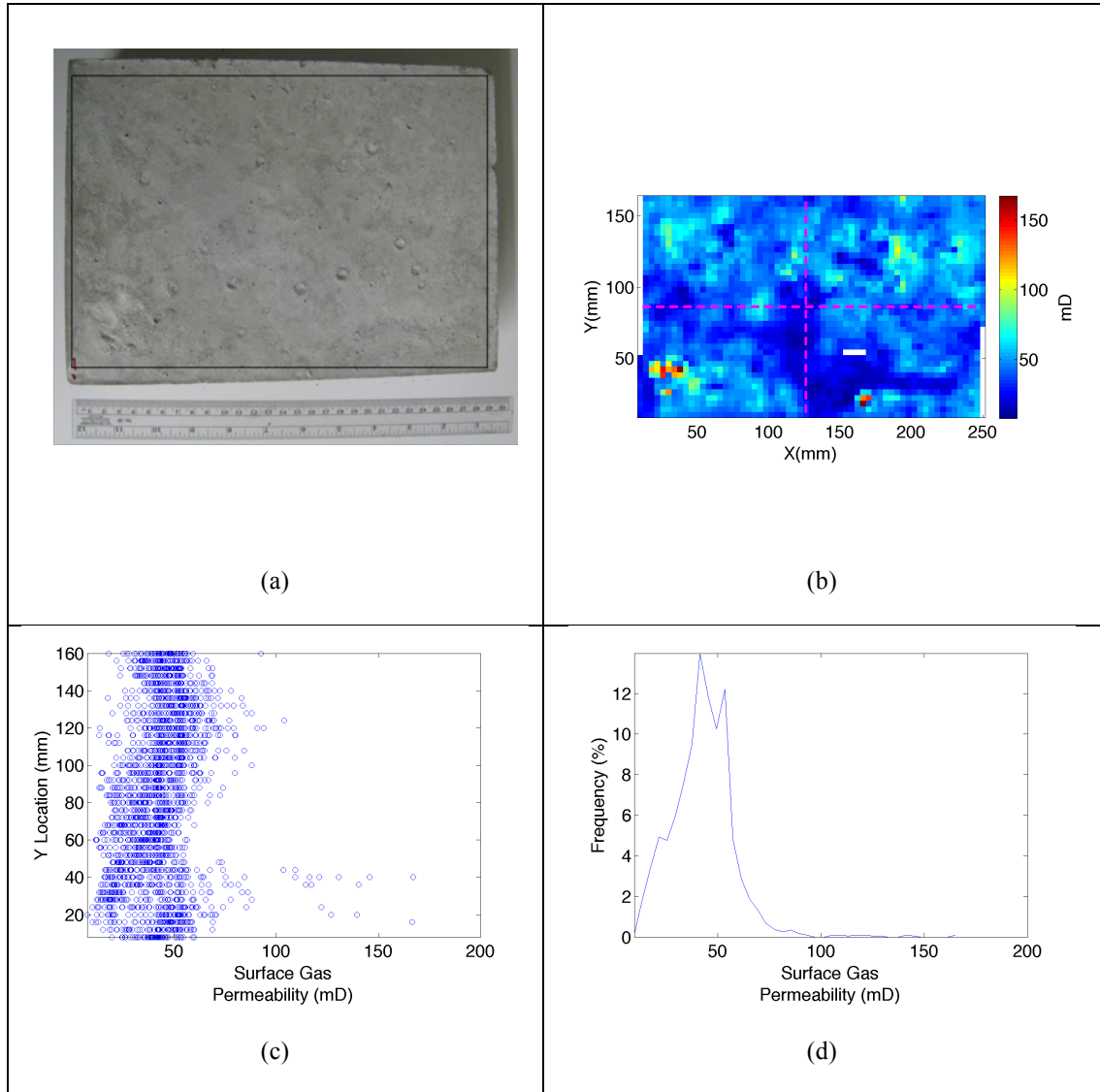


Figure 2.3 Measured surface gas permeability on a 152 mm x 240 mm 3,000psi concrete specimen at 4 mm grid spacing, (a) a photograph of specimen surface, (b) map of gas permeability field, (c) distribution of gas permeability along each y-coordinate, (d) gas permeability probability density function.

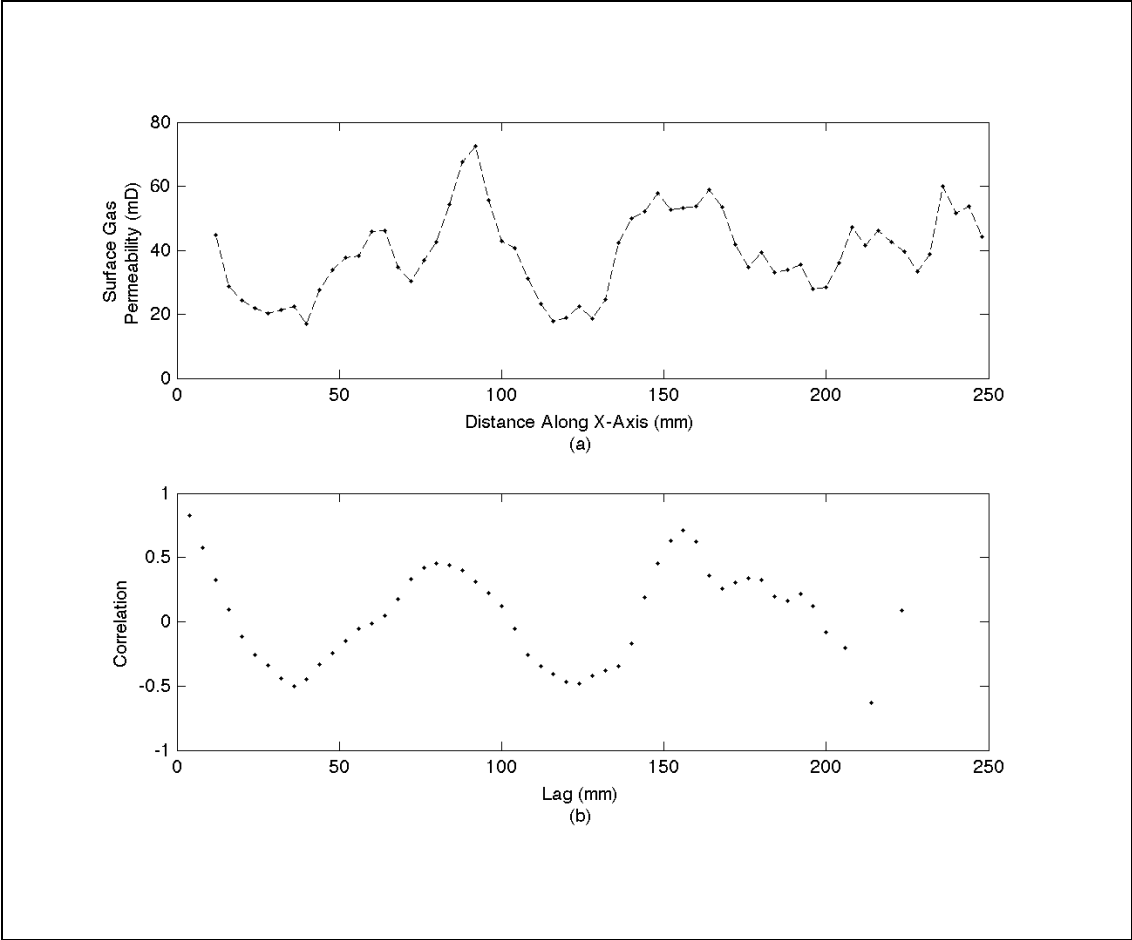


Figure 2.4 Measured surface gas permeability (a) and correlogram (b) of 3,000 psi concrete specimen along the transect $y = 84$ mm. The range = 36 mm.

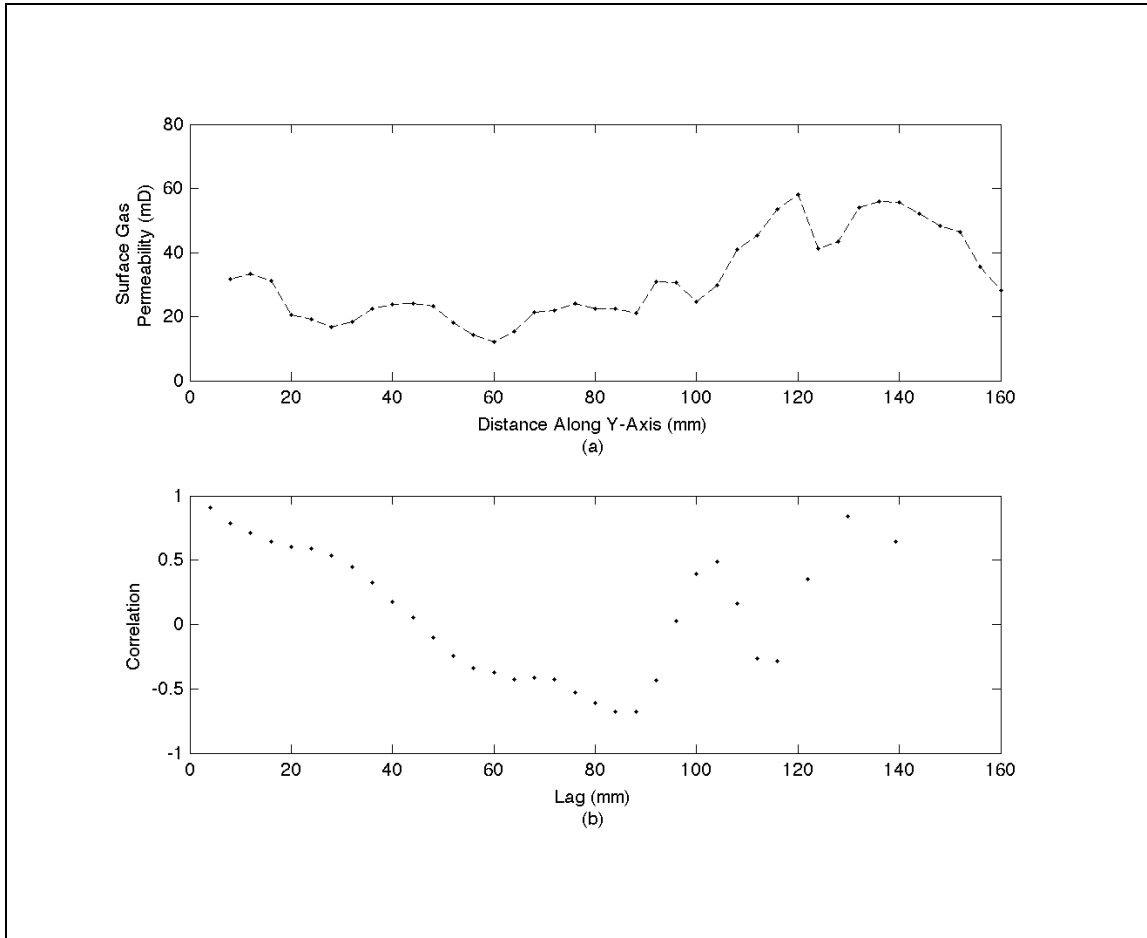


Figure 2.5 Measured surface gas permeability (a) and correlogram (b) of 3,000 psi concrete specimen along the transect $x = 124$ mm. The range = 88 mm.

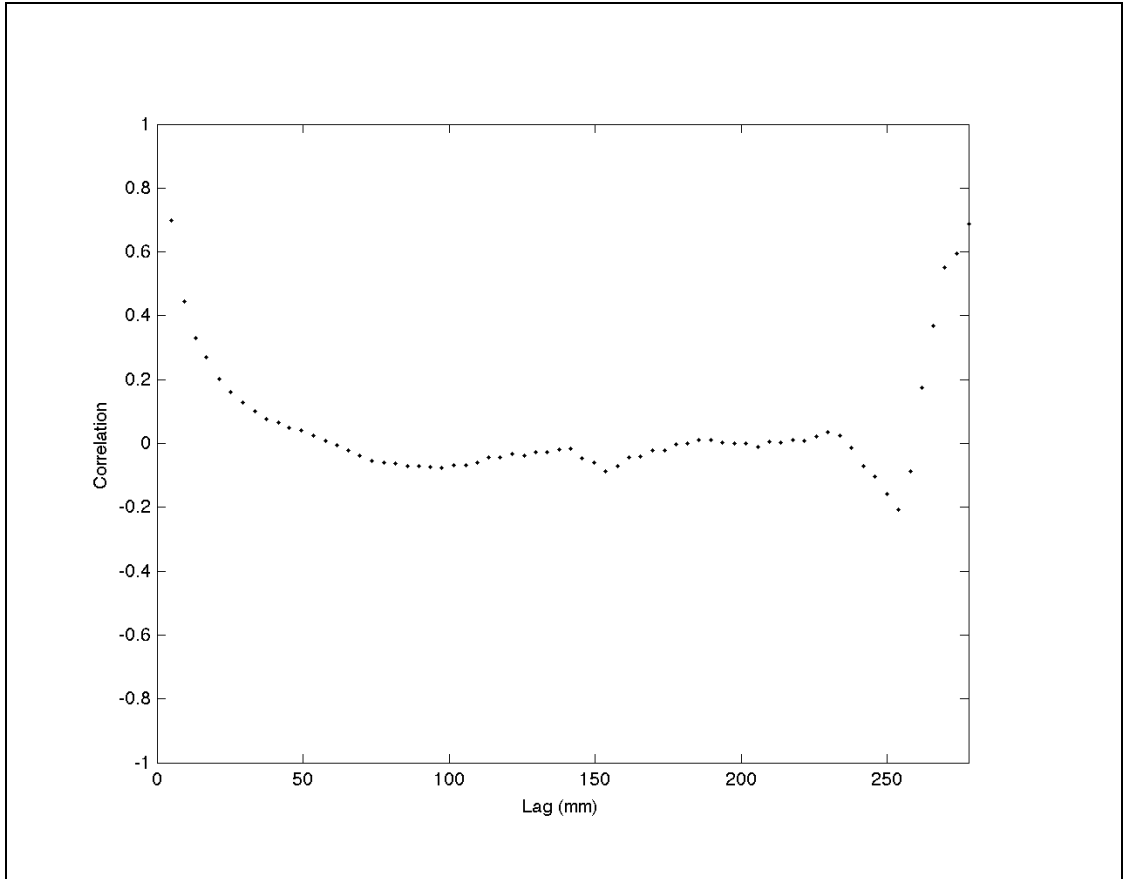


Figure 2.6 Global correlogram of 3,000 psi concrete specimen showing a geostatistical range of ~80 mm.

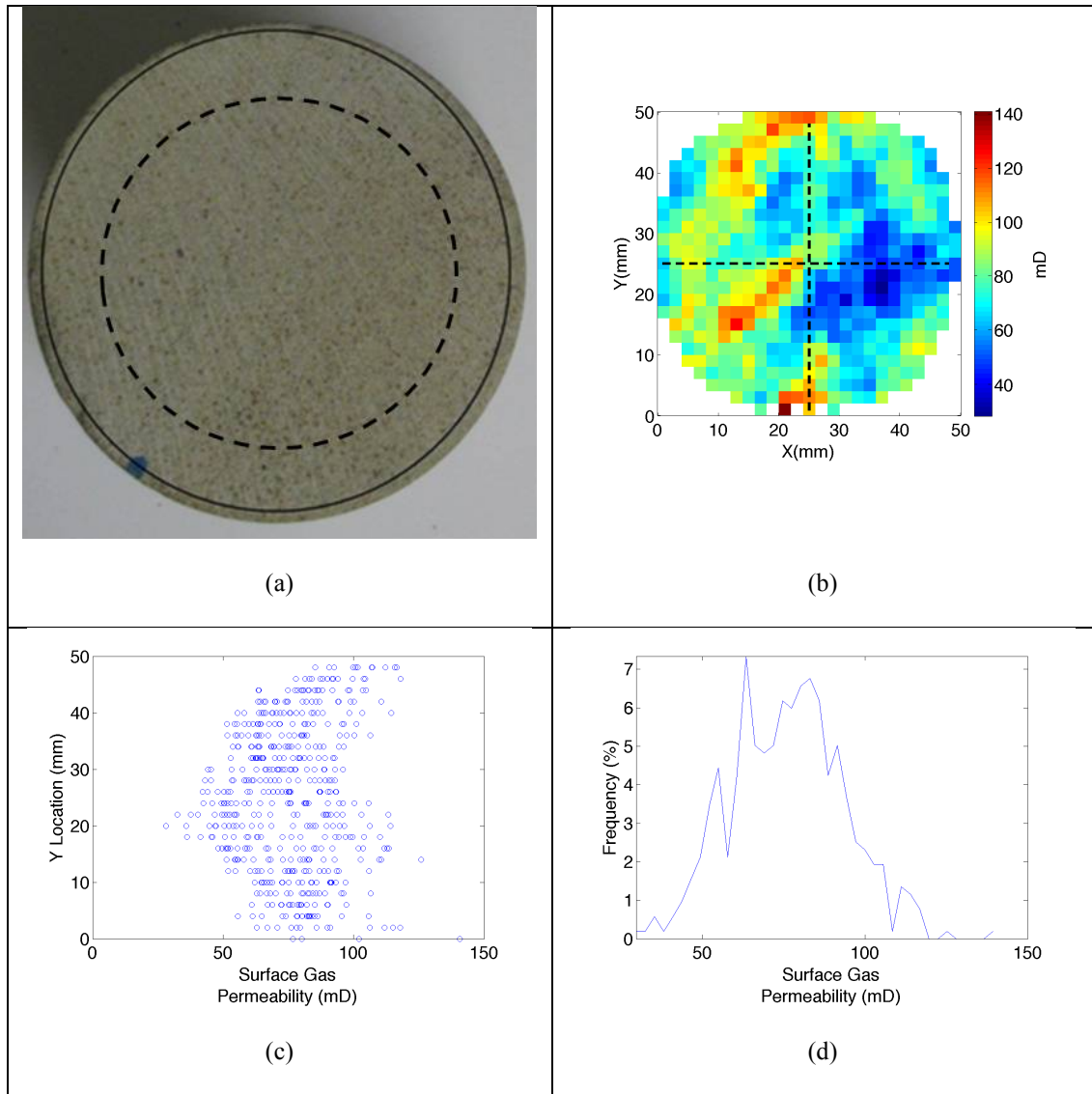


Figure 2.7 Measured surface gas permeability on a 70 mm diameter Ohio sandstone specimen at 2mm grid spacing within the circular area shown as a dashed circle, (a) a photograph of the tested surface of the specimen, (b) map of gas permeability, (c) distribution of gas permeability along each y-coordinate, (d) probability density function of gas permeability.

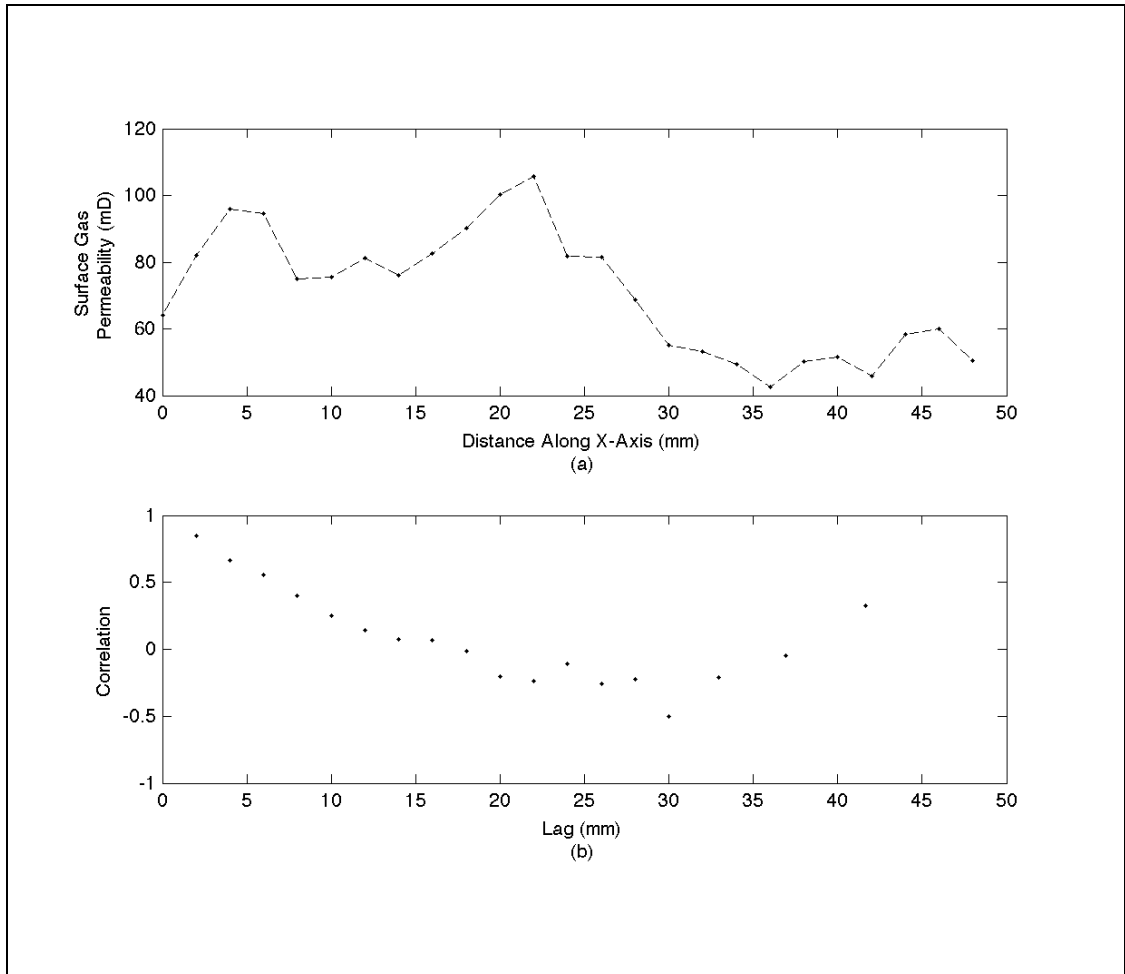


Figure 2.8 Measured surface gas permeability (a) and correlogram (b) of Ohio sandstone specimen along the line $y = 24$ mm. The range = 30 mm.

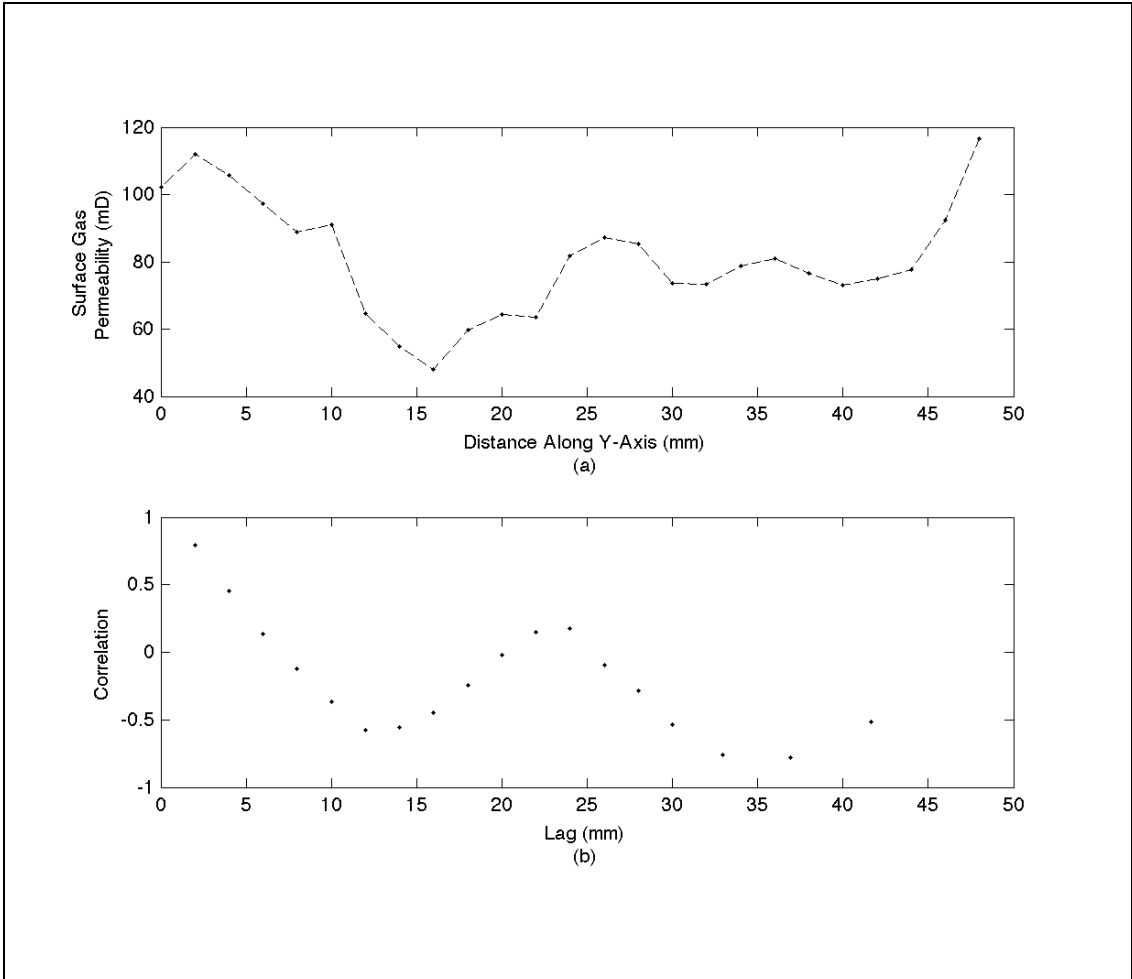


Figure 2.9 Measured surface gas permeability (a) and correlogram (b) of Ohio sandstone specimen along the line $x = 24$ mm. The range = 12 mm.

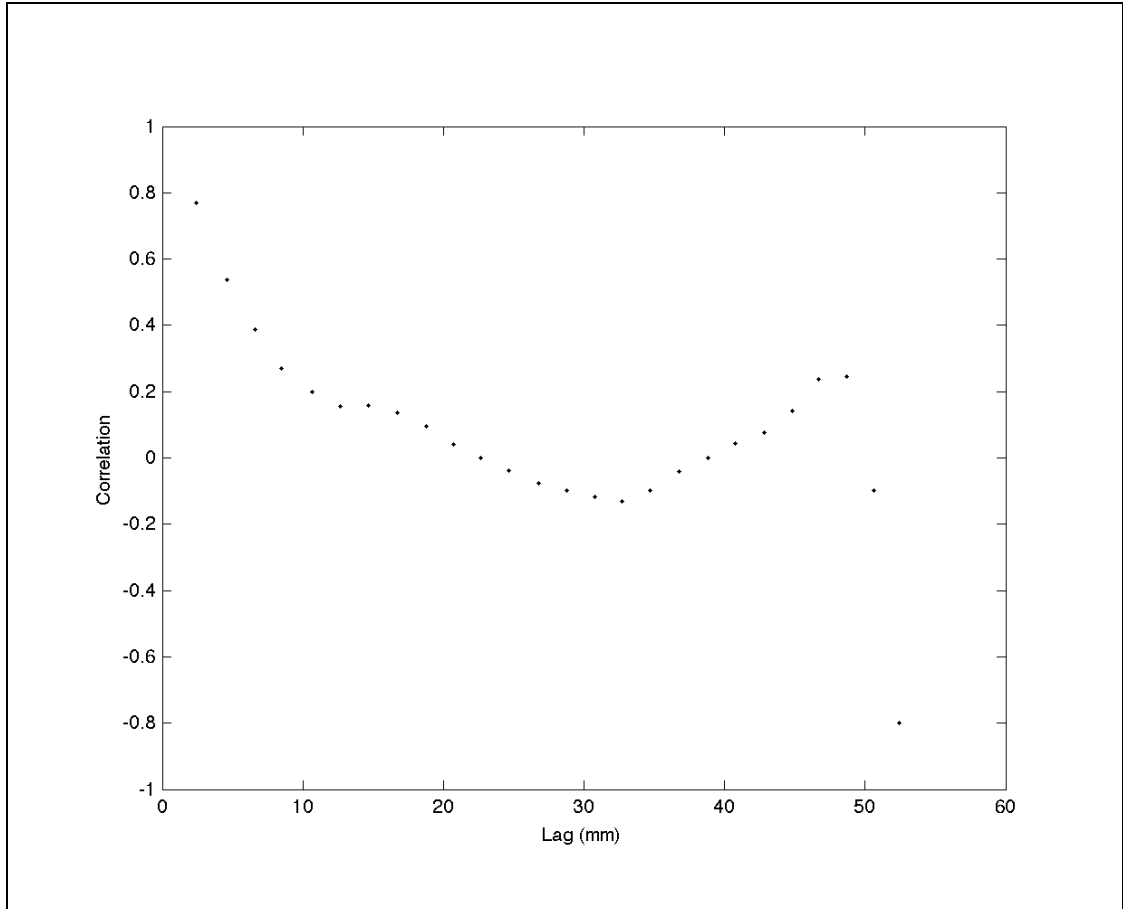


Figure 2.10 Global correlogram of Ohio sandstone specimen showing a range of ~ 30 mm.

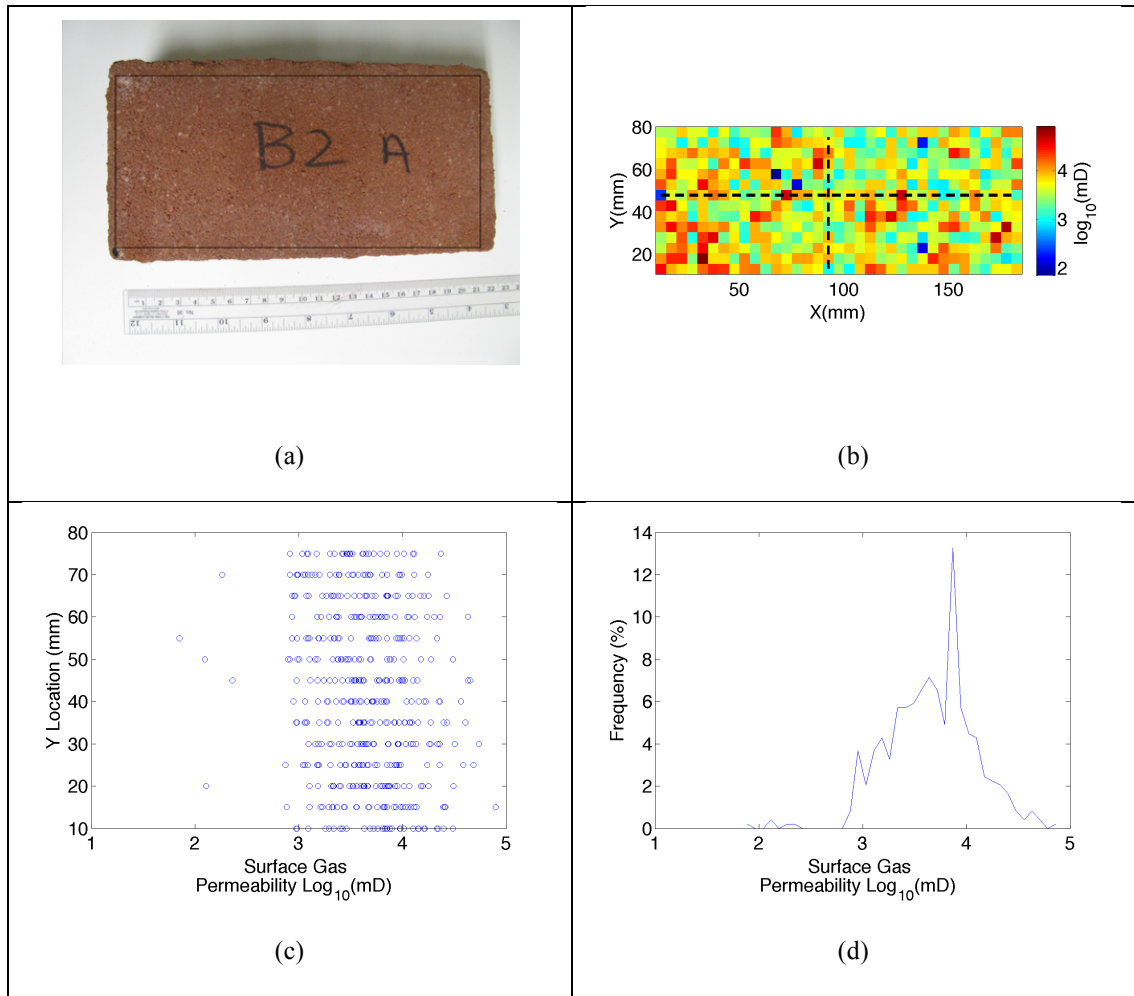


Figure 2.11 Measured surface gas permeability on a 45 mm thick Red Clay Brick over the surface area of 170 mm x 65 mm at 5 mm grid spacing, (a) a photograph of the tested surface of the specimen, (b) map of surface gas permeability, (c) distribution of surface gas permeability along each y-coordinate, (d) probability density function of gas permeability.

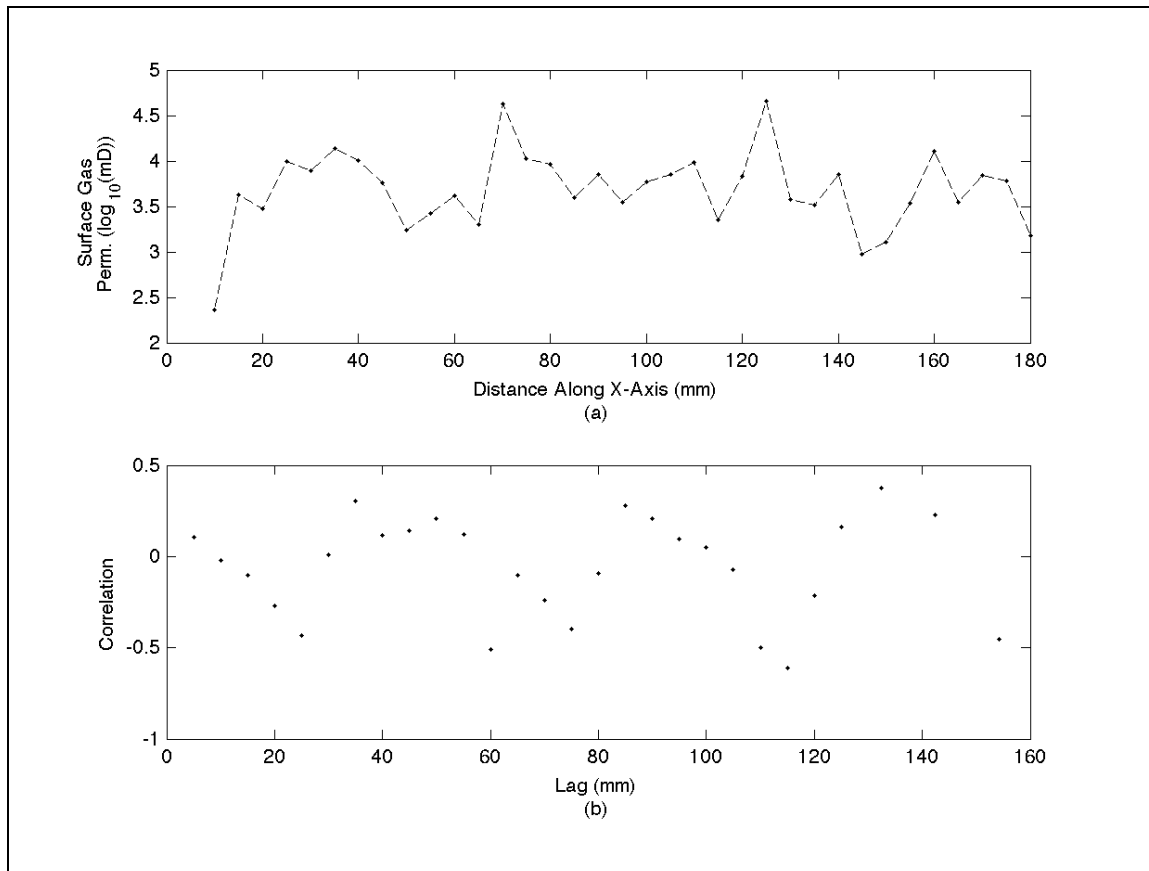


Figure 2.12 Measured surface gas permeability (a) and correlogram (b) of red clay brick specimen along the line $y = 45$ mm. The range = 22 mm.

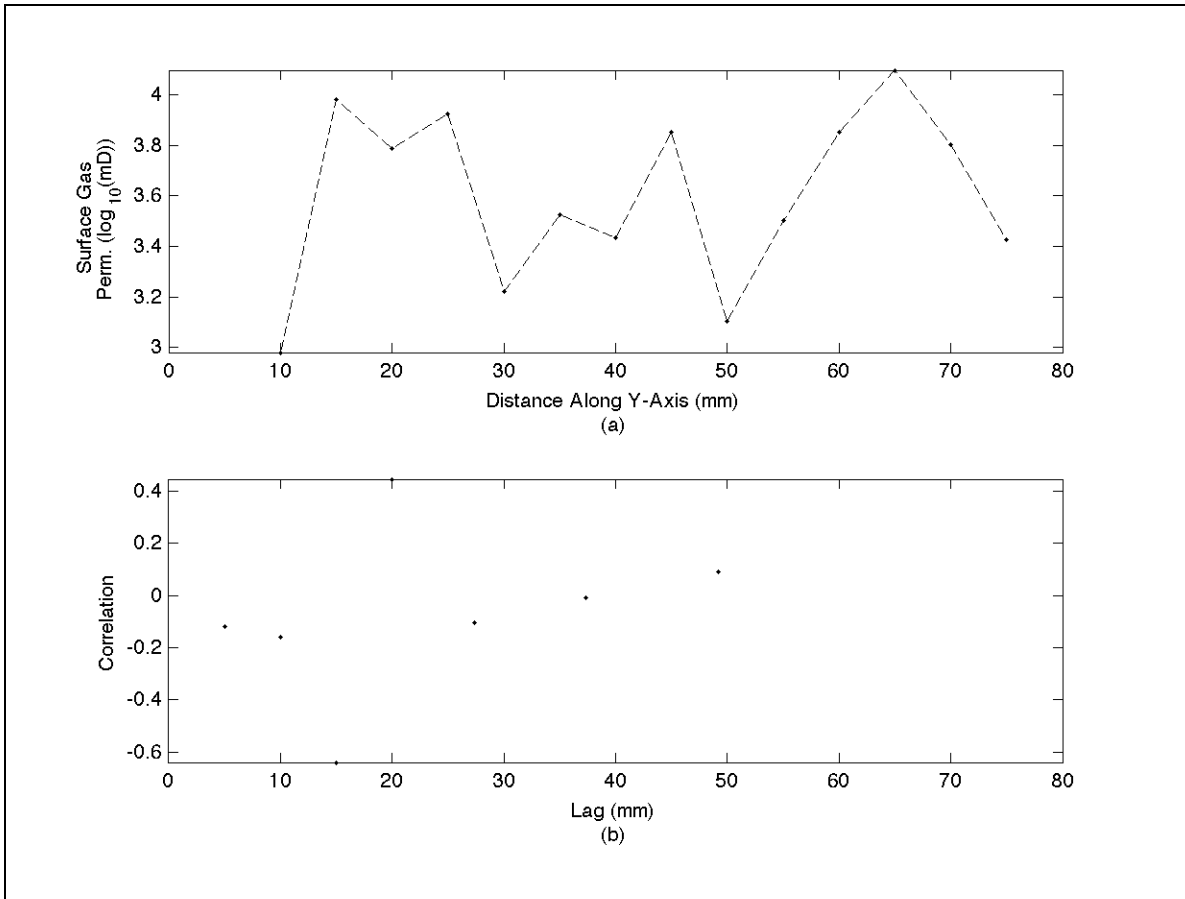


Figure 2.13 Measured surface gas permeability and correlogram of red clay brick specimen along the line $x = 90$ mm. The range is not detected, i.e. 0.

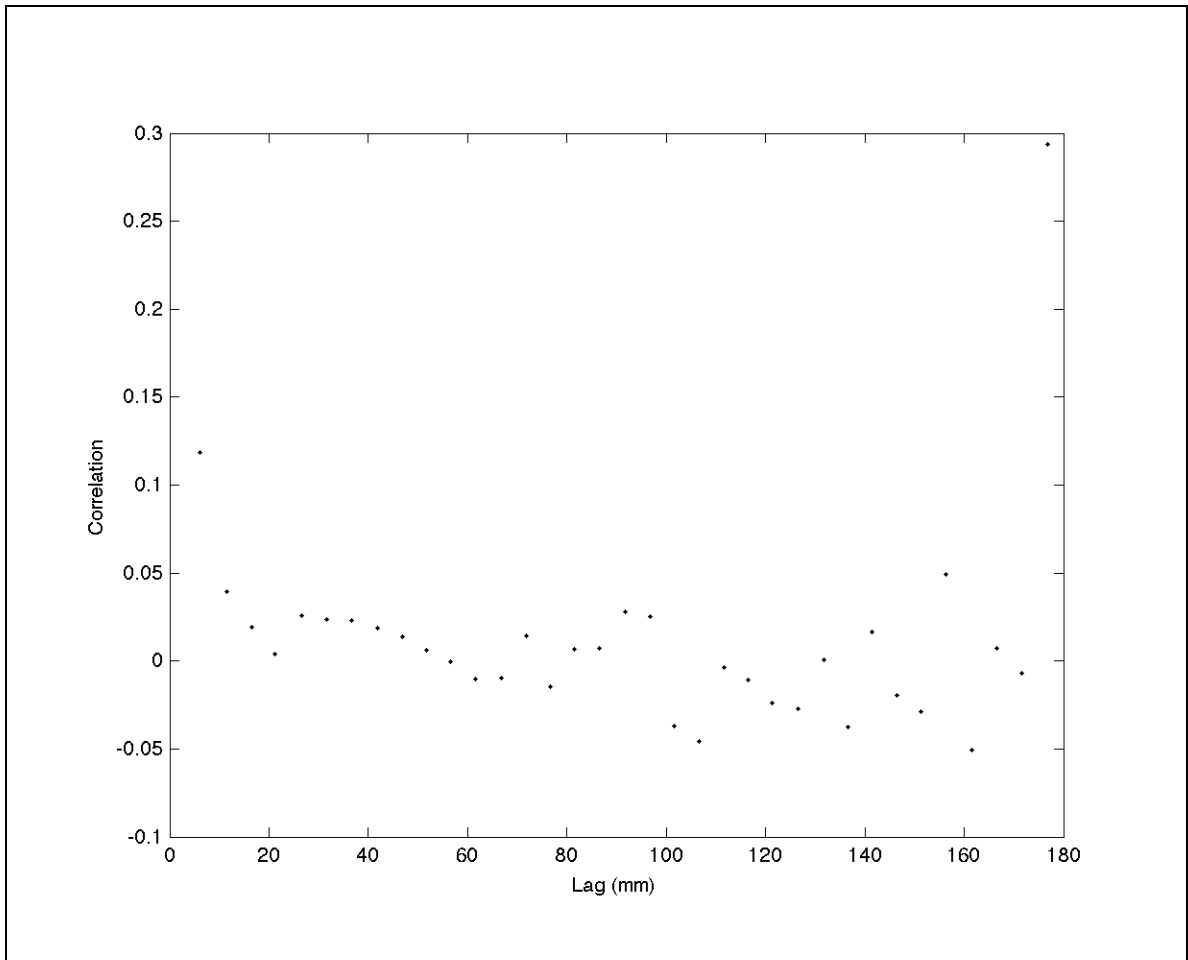


Figure 2.14 Global correlogram of red clay brick specimen. The range = 20mm.

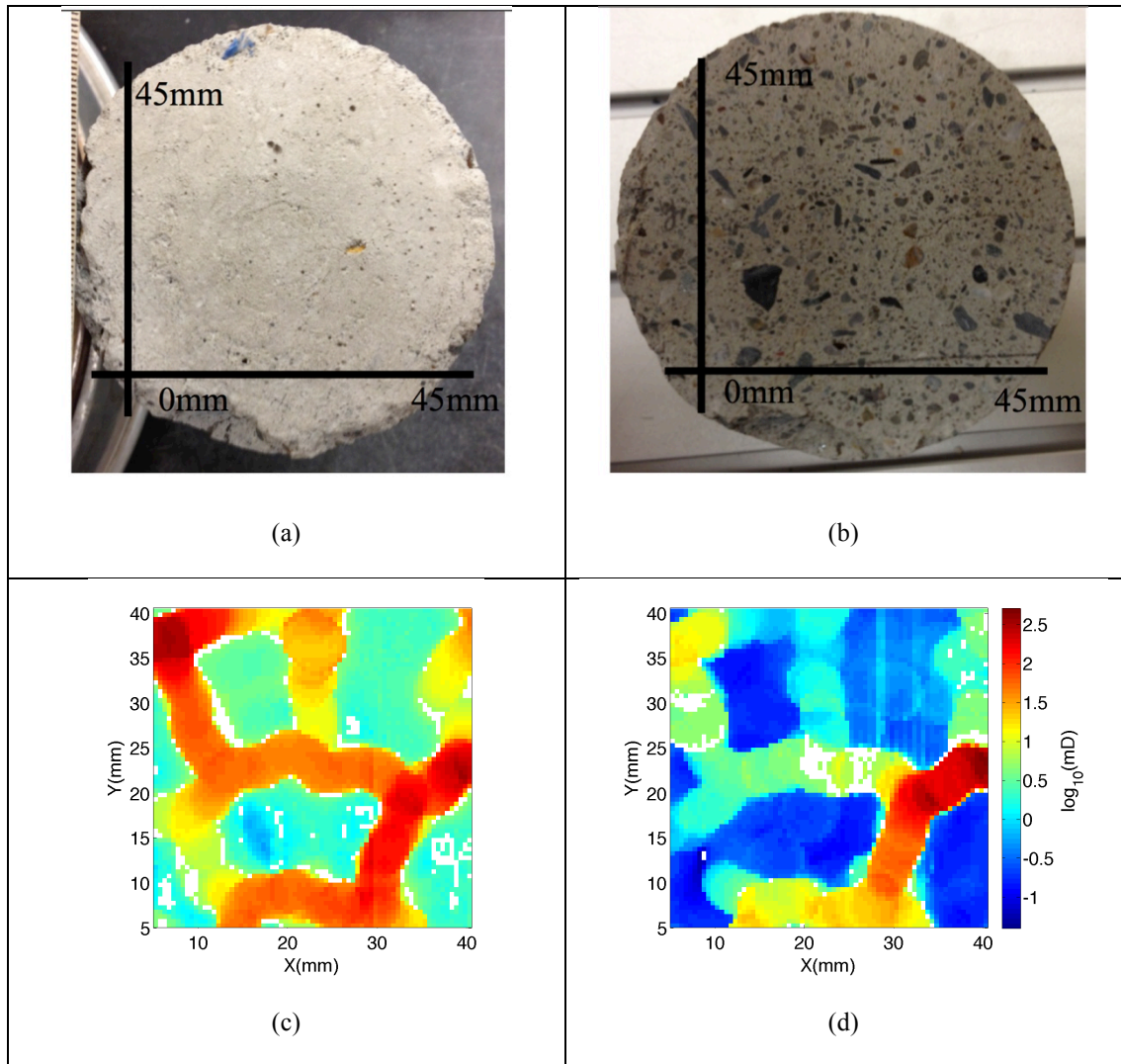


Figure 2.15 Core (70 mm diameter) of 3,000 psi concrete specimen (a) Picture of screeded top, (b) picture of interior about 2 mm below screeded top, (c) surface gas permeability map of the screeded top, (d) surface gas permeability map of on the interior surface. White areas did not return a measurement

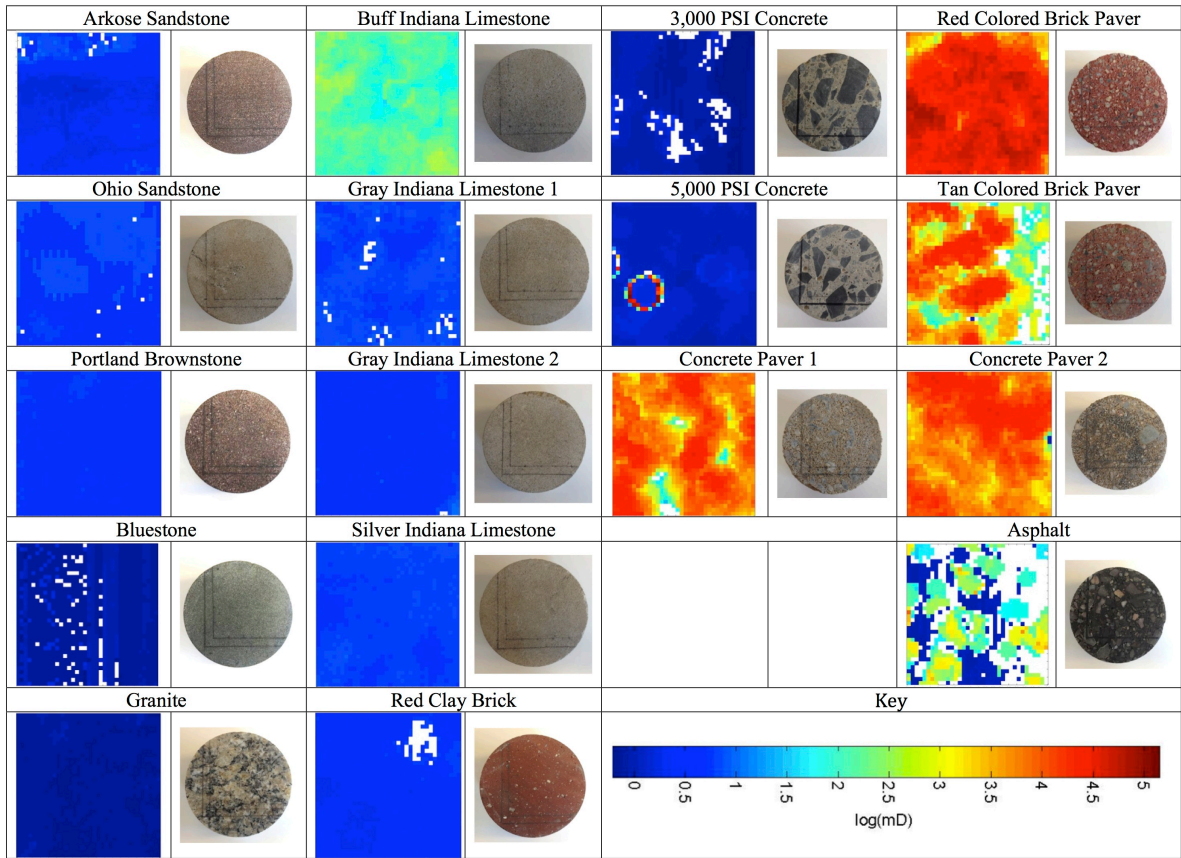


Figure 2.16 Photographs and surface permeability of various building materials. Ten uniform specimens are shown on the left, and seven non-uniform specimens are shown on the right.

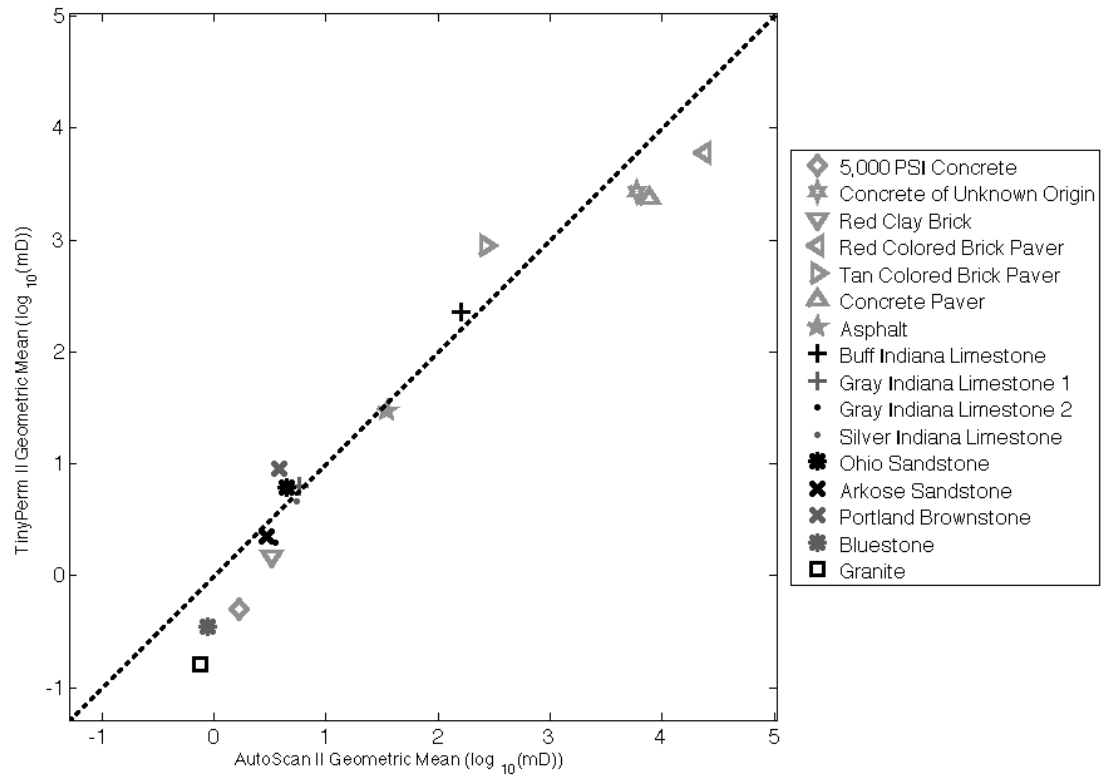


Figure 2.17 TinyPerm II averages (geometric mean) versus AutoScan II averages (geometric mean). Natural materials are shown as dark gray while engineered materials are shown as light gray. Both data sets were \log_{10} transformed, and $R^2 = 0.94$.

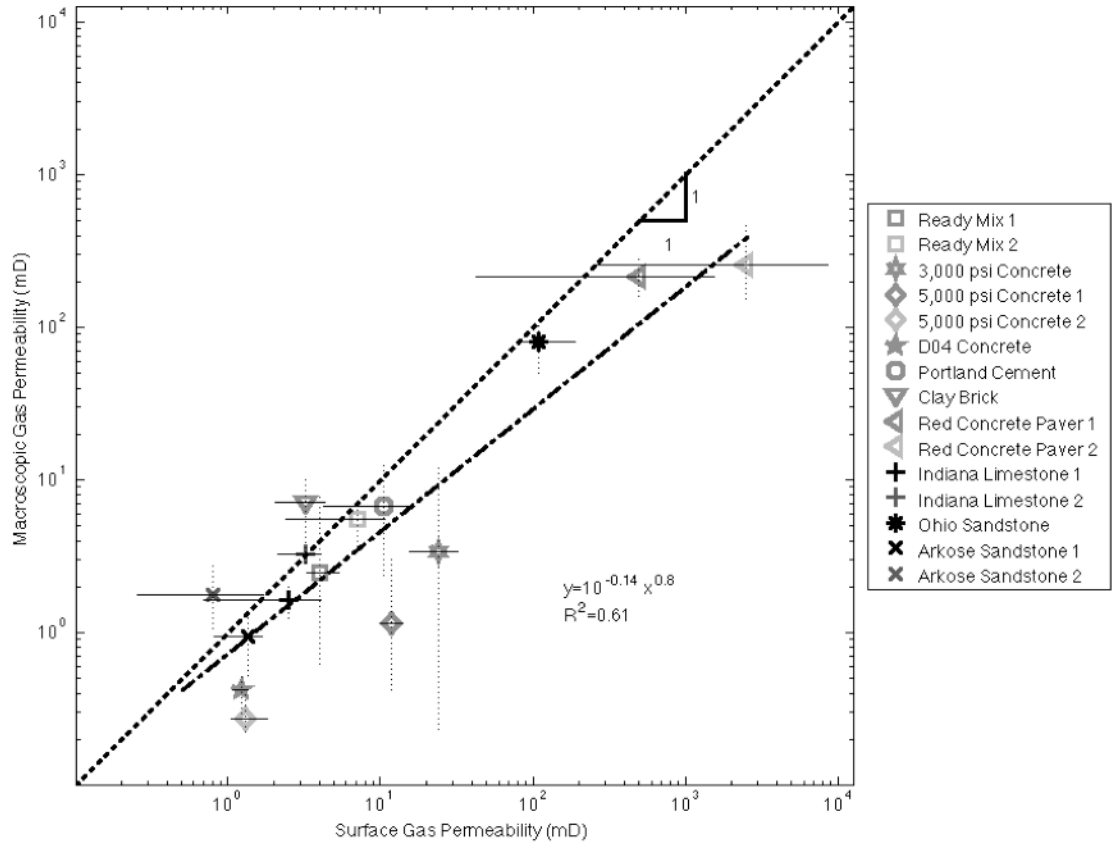


Figure 2.18 Macroscopic gas permeability plotted against geometric mean of surface gas permeability.

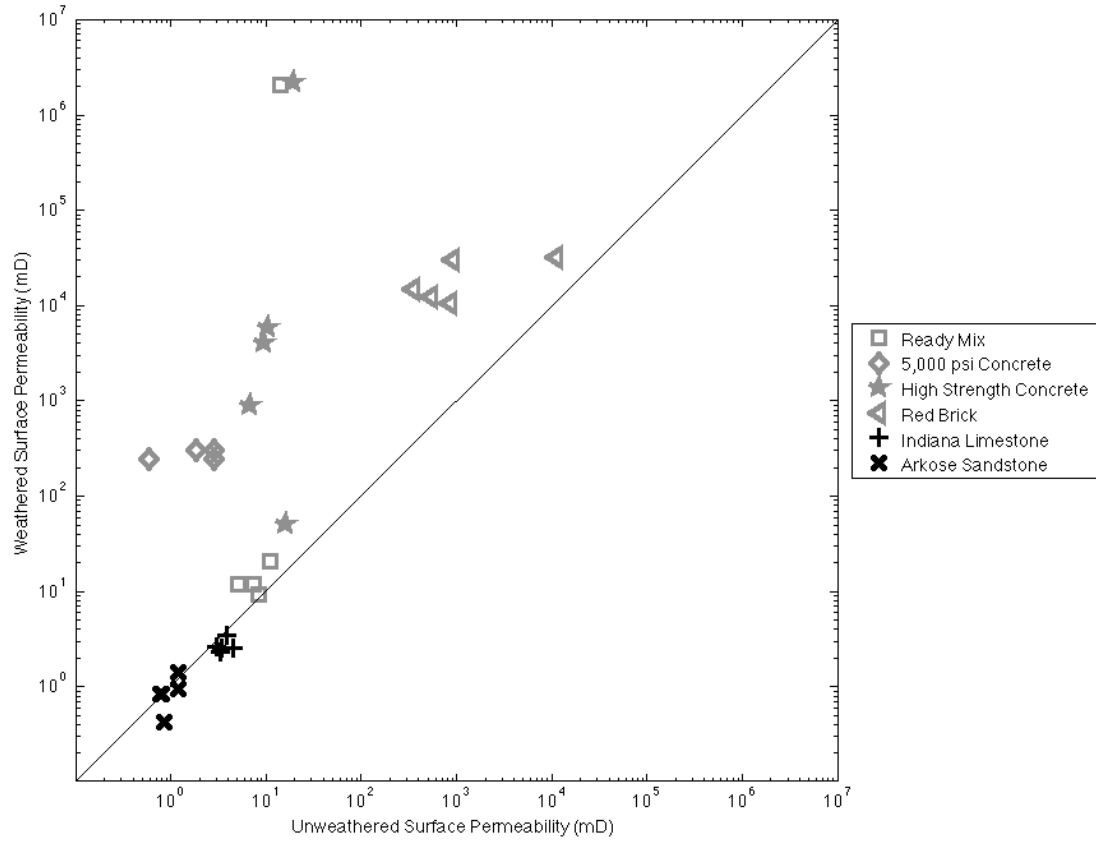


Figure 2.19 Comparison of most probable permeabilities under unweathered and weathered conditions.

Table 2.1 Theoretical dataset and correlation of for lag = 4 mm.

Pair Locations (mm)	Permeability Measurements	
	Tail (mD)	Head (mD)
20, 24	24.5	22.0
24, 28	22.0	20.4
88, 92	67.7	72.6
Correlation between heads and tails = 0.9998		

Table 2.2 Properties of specimens with 1 mm grid spacing.

Name	Origin	Structural Uniformity	Arithmetic Mean (mD)	Geometric Mean (mD)	Most Probable (mD)	Maximum (mD)	Minimum (mD)	Standard Deviation (mD)	Range (mm)	Sill (mD ²)
Arkose Sandstone	Natural	Uniform	3.21	2.94	2.05	9.23	1.39	1.50	14	2.12
Ohio Sandstone	Natural	Uniform	4.74	4.44	6.82	8.63	2.23	1.68	13	2.99
Portland Brownstone	Natural	Uniform	3.84	3.80	3.55	6.00	2.59	0.54	9	0.26
Bluestone	Natural	Uniform	0.89	0.87	0.74	1.90	0.68	0.21	4	0.43
Granite	Natural	Uniform	0.76	0.76	0.75	1.23	0.64	0.06	11	0.0029
Buff Indiana Limestone	Natural	Uniform	176.71	160.45	137.74	575.49	39.47	82.32	29	8497
Gray Indiana Limestone 1	Natural	Uniform	5.79	5.72	6.20	8.38	2.68	0.85	10	0.79
Gray Indiana Limestone 2	Natural	Uniform	3.64	3.57	3.21	10.47	2.25	0.80	9	0.48
Silver Indiana Limestone	Natural	Uniform	5.49	5.46	5.53	7.66	2.55	0.56	9	0.26
Red Clay Brick	Engineered	Uniform	3.35	3.26	2.76	5.67	1.95	0.79	27	0.92
Concrete 3k PSI	Engineered	Non-Uniform	0.98	0.95	1.08	6.08	0.62	0.35	12	0.14
Concrete 5k PSI	Engineered	Non-Uniform	799.77	1.66	2,343.99	140,583.00	0.95	7,963.94	5	0.020
Concrete Paver 1	Engineered	Non-Uniform	8,376.25	5,974.08	5,738.14	31,181.20	26.43	5,605.01	10	38256867
Red Colored Brick Paver	Engineered	Non-Uniform	29,319.86	23,688.76	33,227.79	86,016.90	412.94	14,698.34	11	194910243
Tan Colored Brick Paver	Engineered	Non-Uniform	6,654.13	2,664.46	637.03	38,151.30	1.20	7,574.85	9	68141303
Concrete Paver 2	Engineered	Non-Uniform	9,987.96	7,757.72	4,227.31	36,225.20	1.17	6,634.86	19	54143304
Asphalt	Engineered	Non-Uniform	316.63	34.71	139.70	8,324.67	0.98	584.85	16	344270

CHAPTER 3:
WATER TRANSPORT IN BUILDING MATERIALS:
EXAMINING THE RELATIONSHIP BETWEEN
MACROSCOPIC WICKING OF WATER AND SURFACE
PERMEABILITY

3.1 Abstract

Fluid transport in building materials has broad significance in areas of scientific research ranging from contaminant transport to the freezing of moisture in pore spaces. Reliable prediction of fluid transport through substrates in operational conditions requires knowledge of substrate properties that, primarily, can only be determined experimentally. In addition, obtaining representative specimens of the substrates of interest for laboratory testing is not always feasible. Therefore, an *in situ* method of characterizing transport properties (e.g. surface permeability) that correlate with the fluid transport into the substrate is desirable. This research attempts to correlate the amount of water penetration in typical porous building materials with the surface permeability of those materials. It is intuitively plausible that the fluid transport, especially near the surface of a porous substrate, may have a strong correlation to the substrate's surface permeability. Macroscopic capillary forces (or wicking) are examined by recording the mass of water entering cylindrical specimens for a variety of

building materials as a function of time. The material surface permeabilities were determined using the automated gas permeability measurement device, Autoscan II. A variety of methods, including ordinary linear regression, geostatistical analysis, and multiple linear regressions, explored correlations between substrate surface permeability and water wicked into them. Structurally uniform (i.e. without aggregate) specimens of similar permeabilities demonstrated a strong relationship between wicking and surface permeability, while non-uniform (i.e. containing aggregates) specimens demonstrated a weak relationship between wicking and surface permeability. Consistent with the complicated relationship between pore size, wicking, and surface permeability, a unique relationship was not found across all specimens.

3.2 Introduction

In the event of a disaster involving contaminant transport into building materials, whether from an accidental spill, contaminated flood waters, or an agent release, it would be critical to reliably and rapidly characterize the amount and extent of contaminant that migrates into the affected building material, such that a decontamination strategy can be developed in a timely manner. This research will examine the suitability of using surface permeability readings as a surrogate for macroscopic wicking.

Macroscopic wicking is caused by the capillary action, i.e. surface tension, between a fluid and material walls within pore spaces. This property is relatively well understood to be a function of two opposing forces: the attraction of the fluid to the material walls or pore spaces and the force of gravity pulling the fluid down. Washburn

(1921) explained that, for a simplified system with small pore size and laminar flow conditions, the rate of wicking is a function of the capillary radius, the contact angle between the fluid and the material, the surface tension, the fluid's viscosity, and the height the fluid capillary rise. Pinder and Gray (2008) simplified this concept and showed that the final height of capillary rise, h (m), can be determined by:

$$h = \frac{2\gamma_{wn}\cos\theta}{r\rho_w g}, \quad (3.1)$$

where,

γ_{wn} = Water-air interface surface tension (N/m),

θ = contact angle between fluid and material,

r = the pore radius of the material (m),

ρ_w = the density of water (kg/m^3), and

g = the acceleration of gravity (m/s^2).

Equation (3.1) applies to straight tubes of constant diameter, although it has also been used to inform research in irregular shaped tubes and beds of glass beads (Staples and Shaffer 2002). Pores within building materials are presumed to be less hydraulically connected than in glass tubes or packed beads and would therefore likely permit less fluid movement. Furthermore, the pores in building materials are neither straight nor of constant size. This research focuses on the rapid assessment of macroscopic wicking *in situ*; so it is unlikely that the variables needed for equation (3.1) would be available; and as a result, the equation could only be used as a guide, and not the sole method of predicting h .

Depth of contaminant penetration in building materials is an active area of research. Navaz et al. (2008) investigated droplet spread in porous materials using finite element analysis. Although mitigation of chemical warfare contamination motivates that research, they point out that the effects of wicking cover many diverse fields. Brownell et al. (2006) investigated various properties of six building materials, with particular focus on the amount of water wicked over time. Anand et al. (2003) compared water absorption in conventional and alternative masonry systems.

Similar to wicking, permeability is a function of pore size and pore connectedness. While it is difficult to measure these properties in the field, methods of measuring surface permeability through nondestructive means have been an active area of research for many decades (Dykstra and Parsons 1950; Goggin and Thrasher 1988). Recently, surface permeability has been used to examine material degradation in historic conservation by Valek et al (2000) and compared to overall specimen permeability for both gas and water (Filomena et al. 2013; Selvadurai and Selvadurai 2010).

This research hypothesizes that surface permeability and macroscopic wicking are related by pore size such that surface permeability, as measured by the Autoscan II device, may be used to approximate the volume and depth of fluid wicked over time.

3.3 Materials

In Chapter 2, a variety of building materials were characterized in greater detail. This chapter includes a subset of those materials; specifically, the following *natural* materials were used:

1. **Arkose Sandstone** acquired from Granite Importers, Inc
2. **Ohio Sandstone** acquired from Granite Importers, Inc.,
3. **Portland Brownstone** acquired from Granite Importers, Inc.
4. **Bluestone** sandstone acquired from a local landscaping company
5. **Granite** of unknown origin
6. **Indiana Limestone** from the Indiana Limestone Company.
7. **Indiana Limestone** of differing colors from Granite Importers, Inc.

The following *engineered* materials were tested:

1. **Red Clay Brick** from a Vermont brick yard,
2. **3,000-psi concrete** prepared in the lab,
3. **5,000-psi concrete** prepared in the lab,
4. **Concrete Pavers 1** from a hardware store,
5. **Red Colored Concrete Paver** from a hardware store,
6. **Tan Colored Concrete Paver** from a hardware store,
7. **Concrete Pavers 2** from a hardware store,
8. **Asphalt** from a road excavation,

Although the specific compositions of some of the above materials are unknown (i.e., brick, pavers, asphalt), they are included here because they represent commonly

used building materials. In some cases, materials of the same type but from different batches or different sources were tested; they are noted as Specimen 1, Specimen 2, and so on.

All specimens in this study were cored (68 mm in diameter) from a parent material. The ends were then cut off with a water saw such that the final specimens were approximately 50 mm tall. Cutting the ends ensured that surface effects from weathering or screeding would not influence the results.

3.4 Testing Methods

3.4.1 AutoScan II Surface Gas Permeability

To investigate surface permeability of each specimen, surface permeability was measured along a regularized grid along the specimen surface using the AutoScan II device. The AutoScan II device, the methodology and advantages are described in detail in Chapter 2. The 17 specimens described in section 2.5.3 were examined using a consistent 35mm x 35mm grid with 1mm spacing resulting in n=1,296 sample points. Measurement spacing was designed to be conservative (i.e., overly small) to attempt to capture any spatial autocorrelation that might exist in the specimen surface permeability. Cressie (1993) states that a regular triangular, square, or hexagonal sampling design is usually the most efficient. Autoscan II uses a square sampling design as the default; as a result, the latter was chosen for this work.

3.4.2 Macroscopic Wicking

Macroscopic wicking was also observed and measured in the same 17 specimens of subsection 3.4.1. Figure 3.1 shows a schematic of the experimental setup.

The following procedure was implemented:

1. Horizontal lines, spaced 5 mm apart, were denoted in permanent marker along the side of each specimen.
2. The specimen was suspended on a wire hanger attached to a stand and placed on a scale such that the specimen hovered above a shallow dish filled with water.
3. The wire hanger was lowered until the bottom of the specimen rested in ~1 mm of water; this water level was held constant via the addition of water throughout the experiment.
4. Both the height and the mass of water wicked into the specimen were recorded at five minute intervals over a period of 100 minutes.

The pilot studies showed that, in some cases, water wicked into the center of the specimen migrated more quickly than water along the edges and likely formed a small cone of saturation within the specimen. It was not possible to observe the depth of penetration within the core (i.e. it was only possible to record the time of break through along the top surface), thus the discrepancy in water rise between the sides and center is unknown. For most tests in this study, the water never reached the top of the specimen, and for this research, only the height along the edge of the specimen was recorded.

Since wicking is the result of attraction between the material and the fluid, and since there is less material surrounding the fluid along the core edges than in the center of the specimen, a faster rise within the center is to be expected. Despite the inability to measure the relationship between the two wicking rates, it is assumed that materials with faster wicking along the core edges will also wick faster within the core center. This assumption is sufficient to explore whether a correlation exists between surface permeability and macroscopic wicking, or whether one might be used as a surrogate for the other.

3.5 Results

3.5.1 AutoScan II

The AutoScan II measurement data range over more than five orders of magnitude making visual comparison of the results difficult (Table 3.1). All data are represented using the same $\log_{10}(\text{mD})$ color scale (bottom of Table 3.1) where dark blue is less than 1 mD and dark red is greater than 100,000 mD. Sample points that did not return a permeability value are shown in white. To obtain a metric representative of the entire surface, the following statistics were computed for each specimen: the arithmetic mean (mD); geometric mean (mD), most probable (peak of pdf) (mD), maximum (mD); minimum (mD); standard deviation (mD), and geostatistical metrics known as the range and sill (see Chapter 2 or Isaaks and Srivastava 1990 for details). These are summarized in Table 3.2. Yfantis et al. (1987) recommend that the maximum sampling interval should be about equal to the geostatistical range of the data as

determined by a semivariogram. Since our measurement interval (1 mm) was smaller than the geostatistical ranges observed, we were able to confirm this recommendation in our results.

Many of these statistics are correlated due to data being spread over five orders of magnitude. For example, if a specimen had a large mean, it was also likely to have a large maximum, large standard deviation, and large sill. A principal component analysis was performed on the permeability statistics to generate new variables (i.e., principal components or eigen vectors) that are not co-linear with each other (Table 3.3).

The statistics are used to characterize the surface permeability of each specimen. The principal component analysis enables these characteristics to be reduced into three new variables (or PCs) that are weighted combinations of the original correlated variables. The sill, arithmetic and geometric mean, minimum, standard deviation and, to a lesser extent, maximum value are represented in principal component 1 (PC1). These statistics all have units of mD or mD²; and given the wide range of observed permeability readings, many metrics are highly correlated. PC2 has high weightings for normalized standard deviation and, to a lesser extent, the range and maximum variables. PC3 also represents the range and normalized standard deviation, but the range is more prominent in PC3, while normalized standard deviation is more prominent in PC2.

3.5.2 Macroscopic Wicking

Figure 3.2 shows the volume of water wicked over a 50 minute time period. Although measurements were recorded for 100 minutes, in some cases water reached the maximum height of the specimen after 50 minutes. Concrete of unknown origin was excluded because water had broken through the top of the specimen in less than 50 minutes. As a result, the following analyses only consider the first 50 minutes of the test. These analyses were repeated using concrete of unknown origin and the full 100 minutes for data, and similar results were found.

Similar to the surface permeability tests, the macroscopic wicking tests generated multiple readings for each specimen – specifically, height and mass of water wicked at five-minute intervals for 50 minutes. To examine correlations, we collapsed these measurements into a single metric. This was again accomplished using principal component analysis. Measurements at all time steps were weighted approximately equally in the first principal component. Thus, the first mass principal component (MPC) corresponds to mass wicked at each time step. The MPC is largest (~5) for specimens with a high amount of wicking and grows smaller as the amount of wicking decreases to about -3. This confirms that the MPC is a good surrogate for wicking over time. Table 3.4 shows the principal components of each specimen beside the permeability heat map.

In some cases (e.g., Red Colored Brick Paver versus Silver Indiana Limestone) a larger MPC corresponds to a lower total mass of wicked water after the 50-minute test period. However, over most of the times shown, the Red Colored Brick Paver had a

greater mass wicked, so it is reasonable that the Red Colored Brick Paver has a higher MPC. Regardless, these MPC are much larger than the MPC with less wicking when compared to the entire MPC data set. Although only results for mass wicked over the 50-minute time period are presented here, similar figures and principal components were observed for mass measured over the full 100-minute test period. The height of water rise exhibited similar behavior over both the 50- and 100-minute test periods.

3.5.3 Correlations

The first three principal components from the permeability statistics (PC1, PC2, PC3) and the first principal component of the mass wicked (MPC1) are compared in Table 3.3. Note that permeability maps of similar coloring have similar PCs. This observation serves as visual confirmation that PC1, PC2, and PC3 can be used to characterize each permeability map. If permeability and wicking are correlated, then specimens with similar MPCs should have similarly colored permeability maps; yet that is not the case. See, for example, the third column of Table 3.4. The light blue surface permeability maps have similar PCs, but very different MPCs. Indeed, Gray Indiana Limestone 1 had one of the largest amount of wicking, while Gray Indiana Limestone 2 had one of the smallest.

Figure 3.3 shows the multivariate linear correlation between all three PCs and MPC. As expected given the results of Table 3.3, there is little predictive capability; the adjusted R^2 is only 0.036. The plot of Actual by Predicted shows that actual (i.e., observed) MPC values have a large range (between -4 and 10), while predicted values

are mainly between 0 and 2. Similar results were obtained for height of water wicked and when using single-variable linear regression.

Since wicking behavior can be highly variable and dependent on multiple variables such as pore size and tortuosity, it was hypothesized that materials with similar permeabilities would have similar pore sizes and therefore similar wicking behavior. Similarly, materials with similar structural uniformity, i.e. with and without aggregate, would have similar flow paths and therefore similar wicking behavior. A second set of analyses was performed to model wicking using two separate groups of materials. Group one was structurally uniform materials, i.e. without aggregates, of low (approximately < 10 mD) surface permeability, (i.e., bluestone, ohio sandstone, gray Indiana limestone 1 and 2, silver Indiana limestone, Portland brownstone, and red clay brick). This confined the analysis to specimens with visually similar particle sizes and structure and therefore likely similar pore sizes and tortuosity. Group 2 was structurally non-uniform materials (i.e. the concretes and pavers). Buff Indiana limestone and asphalt were excluded because the former was uniform but had relatively high permeability and the latter is a material that is known to be hydrophobic.

To further simplify the analysis, only the volume of water wicked at 50 minutes was considered in this second set of analyses. This simplification ignores the relationship between time and pore size on wicking and creates a simpler analysis.

A clear relationship between wicking and surface permeability in group 1 is shown in Figure 3.4 with $R^2 = 0.95$ where the mass of water wicked at 50 minutes is plotted against the geometric mean of surface permeability. Figure 3.5 shows a similar

plot with a log-scale x-axis for group 2 specimens with $R^2 = 0.55$. Figure 3.6 shows all specimens considered and their respective relationships.

3.6 Conclusions and Discussion

This research did not find a global relationship between surface permeability, as measured by the AutoScan II, and wicking potential over all the specimens measured which is consistent with the complicated relationship between pore size and wicking. For example, smaller pores can be so small as to restrict flow while larger pores have less surface area and therefore reduced capillarity. Consequently, both too large and too small pores can hinder wicking. Given the non-linear relationship between pore size and wicking potential, it is reasonable that we were unable to find a unique relationship between surface permeability and wicking potential that governed over the wide range of materials and permeabilities measured in this study.

However, for uniform specimens of similarly low permeability, a clear relationship was observed. Indeed, a wide range of wicking potential was observed over a small range of permeabilities. This relationship provides a promising indication that surface permeability can be used to predict mass wicked under certain circumstances. It should be cautioned that this relationship is based on only nine observations, so additional research is needed to determine how robust the relationship is and under what conditions it is relevant.

The relationship between wicking potential and surface permeability in non-uniform materials was less pronounced and occurred over a large range of

permeabilities with sparse data. Additional research is required to determine if this relationship remains with permeabilities in between those observed here.

3.7 Works Cited

- [1] Anand, K. B., Vasudevan, V., and Ramamurthy, K. (2003). “Water permeability assessment of alternative masonry systems.” *Building and Environment*, 38(7), 947–957.
- [2] Brownell, M., Dewoolkar, M., Hayden, N., Rizzo, D., and Porter, D. (2006). “Interactions of Contaminating Agents with Building Materials: Literature Review and Preliminary Experiments.” Report.
- [3] Cressie, N. A. C. (1993). *Statistics for Spatial Data*. Wiley series in probability and mathematical statistics, Wiley, New York.
- [4] Dykstra, H. & Parsons, R. 1950 The prediction of oil recovery by waterflood. Secondary recovery of oil in the United States. *J. Pet. Tech.* 8 , 55–56.
- [5] Filomena, C. M., J. Hornung, and H. Stollhofen (2013) Assessing accuracy of gas-driven permeability measurements: a comparative study of diverse Hassler-cell and probe permeameter devices, *Solid Earth Discuss.*, 5, 1163–1190.
- [6] Goggin, D. J., Thrasher, R. L. & Lake, L. W. 1988 A theoretical and experimental analysis of minipermeameter response including gas slippage and high velocity flow effects. *In situ* 12, 79–116.
- [7] Goovaerts, P., (1998) Geostatistical tools for characterizing the spatial variability of microbiological and physico-chemical soil properties *Biol Fertil Soils*, 27: 315–334.

- [8] Isaaks, E. H., and Srivastava, R. M. (1990). *An Introduction to Applied Geostatistics*. Oxford University Press, USA.
- [9] Navaz, H. K., Markicevic, B., Zand, A. R., Sikorski, Y., Chan, E., Sanders, M., and D’Onofrio, T. G. (2008). “Sessile droplet spread into porous substrates—Determination of capillary pressure using a continuum approach.” *Journal of Colloid and Interface Science*, 325(2), 440–446.
- [10] New England Research, Inc. (ND). *AutoScan Automatic Multi-Sample Measurement Platform Gas Permeability Manual*. White River Junction, VT.
- [11] Pinder, G. F. and W. G. Gray (2008). *Essentials of Multiphase Flow and Transport in Porous Media*. Wiley, Hoboken, N.J.
- [12] Selvadurai, A. P. S. and P. A. Selvadurai (2010) Surface permeability tests: experiments and modelling for estimating effective permeability, *Proc. R. Soc. A* doi:10.1098/rspa.2009.0475.
- [13] Staples, T. L., and Shaffer, D. G. (2002). “Wicking flow in irregular capillaries.” *Colloids and Surfaces A: Physicochemical and Engineering Aspects*, 204(1–3), 239–250.
- [14] Valek, J., J. J. Hughes and P. J. M. Bartos, (2000), Portable probe gas permeability: a non-destructive test for the in-situ characterization of historic masonry, *Mat. and Struc.*, 33, 194-197.
- [15] Washburn, E. W. (1921). “The Dynamics of Capillary Flow.” *Physical Review*, 17(3), 273–283.

- [16] Yfantis, E. A., Flatman, G. T. and Behar, J. V. (1987). Efficiency of Kriging Estimation for Square, Triangular, and Hexagonal Grids. *Mathematical Geology*. 19(3), 183-205.

3.8 Figures and Tables

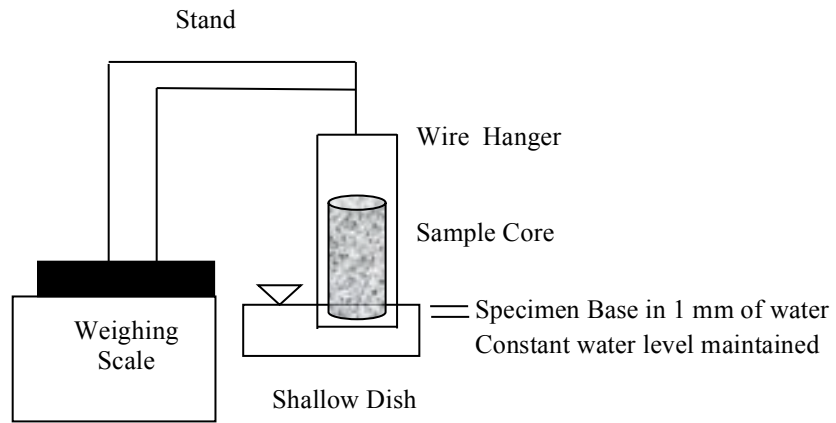


Figure 3.1 Schematic of macroscopic wicking experiment setup.

Table 3.1 Photographs and surface permeability of various building materials. Ten uniform specimens are shown on the left, and seven non-uniform specimens are shown on the right.

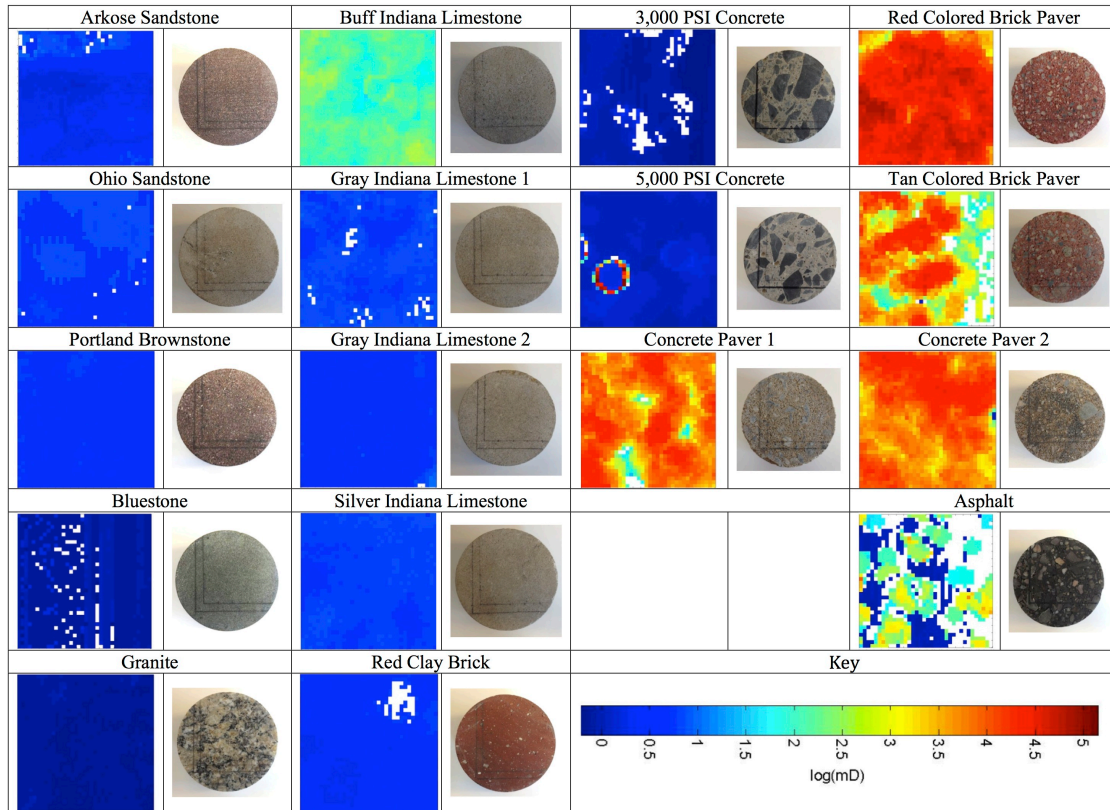


Table 3.2 Properties of specimens with 1 mm grid spacing.

Name	Origin	Structural Uniformity	Arithmetic Mean (mD)	Geometric Mean (mD)	Most Probable (mD)	Maximum (mD)	Minimum (mD)	Standard Deviation (mD)	Range (mm)	Sill (mD2)	Volume of Water Wicked at 50 Minutes (cm ³)	Height of Water Wicked at 50 Minutes (mm)
Arkose Sandstone	Natural	Uniform	3.21	2.94	2.05	9.23	1.39	1.50	14	2.12	1.8	5
Ohio Sandstone	Natural	Uniform	4.74	4.44	6.82	8.63	2.23	1.68	13	2.99	14.5	28
Portland Brownstone	Natural	Uniform	3.84	3.80	3.55	6.00	2.59	0.54	9	0.26	2.5	14
Bluestone	Natural	Uniform	0.89	0.87	0.74	1.90	0.68	0.21	4	0.43	0.4	1
Granite	Natural	Uniform	0.76	0.76	0.75	1.23	0.64	0.06	11	0.0029	0.4	15
Buff Indiana Limestone	Natural	Uniform	176.71	160.45	137.74	575.49	39.47	82.32	29	8497	12	34
Gray Indiana Limestone 1	Natural	Uniform	5.79	5.72	6.20	8.38	2.68	0.85	10	0.79	17	39
Gray Indiana Limestone 2	Natural	Uniform	3.64	3.57	3.21	10.47	2.25	0.80	9	0.48	4	13
Silver Indiana Limestone	Natural	Uniform	5.49	5.46	5.53	7.66	2.55	0.56	9	0.26	16	32
Red Clay Brick	Engineered	Uniform	3.35	3.26	2.76	5.67	1.95	0.79	27	0.92	3.5	8
Concrete 3k PSI	Engineered	Non-Uniform	0.98	0.95	1.08	6.08	0.62	0.35	12	0.14	4	0
Concrete 5k PSI	Engineered	Non-Uniform	799.77	1.66	2,343.99	140,583.00	0.95	7,963.94	5	0.020	2.4	14
Concrete Paver 1	Engineered	Non-Uniform	8,376.25	5,974.08	5,738.14	31,181.20	26.43	5,605.01	10	38256867	18	47
Red Colored Brick Paver	Engineered	Non-Uniform	29,319.86	23,688.76	33,227.79	86,016.90	412.94	14,698.34	11	194910243	15	47
Tan Colored Brick Paver	Engineered	Non-Uniform	6,654.13	2,664.46	637.03	38,151.30	1.20	7,574.85	9	68141303	4	14
Concrete Paver 2	Engineered	Non-Uniform	9,987.96	7,757.72	4,227.31	36,225.20	1.17	6,634.86	19	54143304	6	28
Asphalt	Engineered	Non-Uniform	316.63	34.71	139.70	8,324.67	0.98	584.85	16	344270	0	0

Table 3.3 Principal Components performed on permeability statistics

	Principal Component 1	Principal Component 2	Principal Component 3
Range	-0.09	0.45	0.89
Sill	0.46	0.24	-0.09
Arithmetic Mean	0.46	0.24	0.05
Maximum	0.38	-0.43	0.24
Minimum	0.42	0.26	-0.08
Standard Deviation (SD)	0.47	-0.07	0.08
Normalized SD	0.14	-0.65	0.36
Cumulative Percent	59.1	86.5	97.0

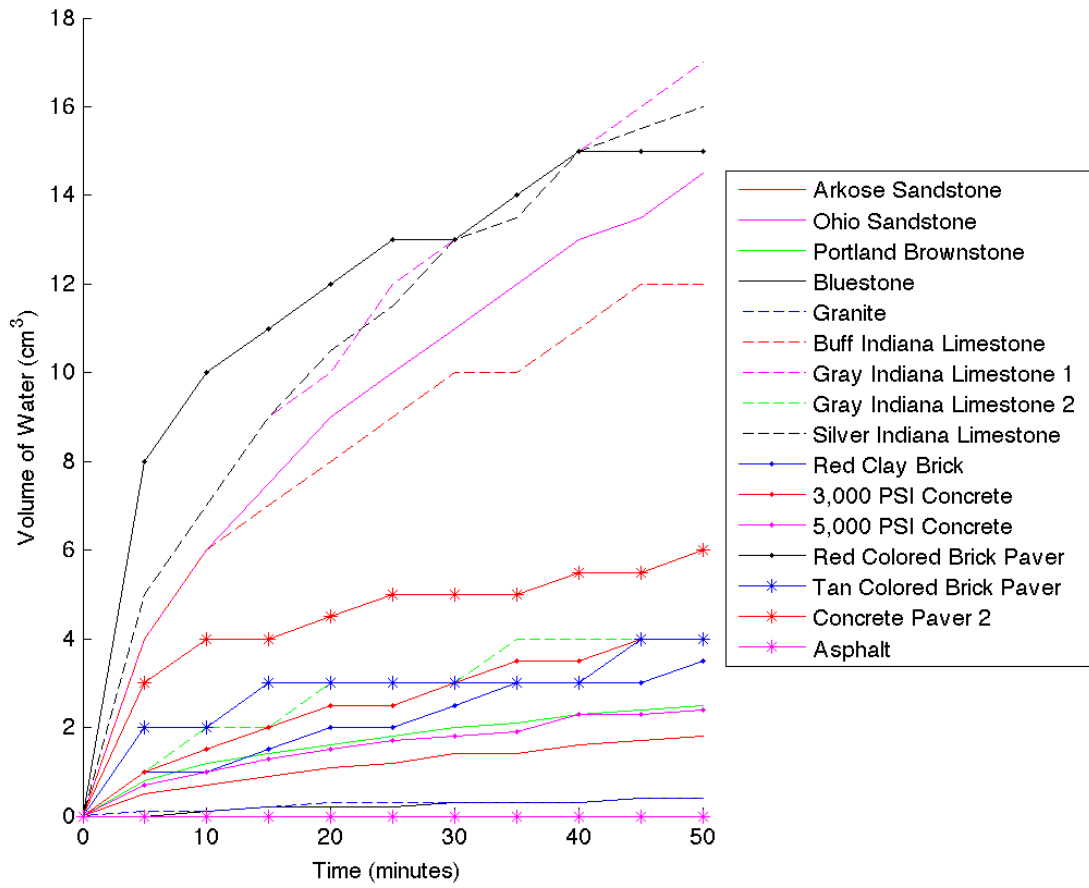
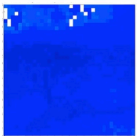
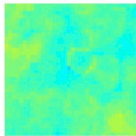
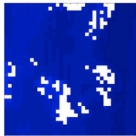
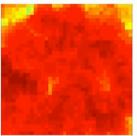
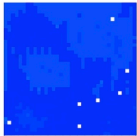
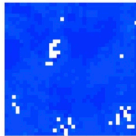
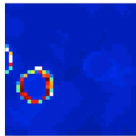
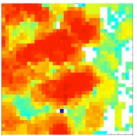
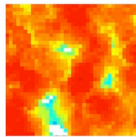
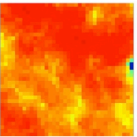
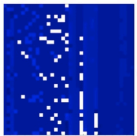
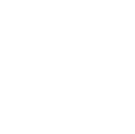
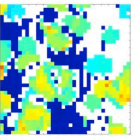
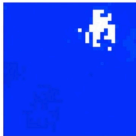
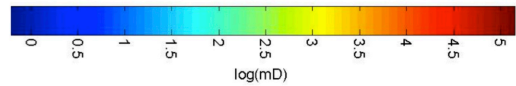


Figure 3.2 Mass of water wicked in grams over 50 minutes for all specimens.

Table 3.4 Permeability heat map and principal components

<p>Arkose Sandstone</p>  <p>Permeability PC PC1 -1.046 PC2 0.260 PC3 0.055 Mass PC MPC1 -2.420</p>	<p>Buff Indiana Limestone</p>  <p>Permeability PC PC1 -1.043 PC2 1.238 PC3 1.781 Mass PC MPC1 2.831</p>	<p>3,000 PSI Concrete</p>  <p>Permeability PC PC1 -1.028 PC2 0.156 PC3 -0.222 Mass PC MPC1 -1.411</p>	<p>Red Colored Brick Paver</p>  <p>Permeability PC PC1 6.798 PC2 1.831 PC3 -0.368 Mass PC MPC1 5.658</p>
<p>Ohio Sandstone</p>  <p>Permeability PC PC1 -1.032 PC2 0.214 PC3 -0.123 Mass PC MPC1 3.523</p>	<p>Gray Indiana Limestone 1</p>  <p>Permeability PC PC1 -1.006 PC2 0.099 PC3 -0.500 Mass PC MPC1 4.720</p>	<p>5,000 PSI Concrete</p>  <p>Permeability PC PC1 1.985 PC2 -4.884 PC3 0.866 Mass PC MPC1 -2.106</p>	<p>Tan Colored Brick Paver</p>  <p>Permeability PC PC1 1.299 PC2 -0.248 PC3 -0.249 Mass PC MPC1 -1.128</p>
<p>Portland Brownstone</p>  <p>Permeability PC PC1 -0.995 PC2 0.043 PC3 -0.616 Mass PC MPC1 -2.014</p>	<p>Gray Indiana Limestone 2</p>  <p>Permeability PC PC1 -0.993 PC2 0.026 PC3 -0.593 Mass PC MPC1 -1.230</p>	<p>Concrete Paver 1</p>  <p>Permeability PC PC1 0.910 PC2 0.044 PC3 -0.231 Mass PC MPC1 9.053</p>	<p>Concrete Paver 2</p>  <p>Permeability PC PC1 1.100 PC2 0.559 PC3 0.847 Mass PC MPC1 0.114</p>
<p>Bluestone</p>  <p>Permeability PC PC1 -0.890 PC2 -0.505 PC3 -1.631 Mass PC MPC1 -3.094</p>	<p>Silver Indiana Limestone</p>  <p>Permeability PC PC1 -0.994 PC2 0.037 PC3 -0.657 Mass PC MPC1 4.617</p>	<p>Asphalt</p>  <p>Permeability PC PC1 -1.046 PC2 0.260 PC3 0.055 Mass PC MPC1 -2.420</p>	<p>Asphalt</p>  <p>Permeability PC PC1 -0.818 PC2 -0.121 PC3 0.514 Mass PC MPC1 -3.246</p>
<p>Granite</p>  <p>Permeability PC PC1 -1.032 PC2 0.172 PC3 -0.395 Mass PC MPC1 0.0029</p>	<p>Red Clay Brick</p>  <p>Permeability PC PC1 -1.215 PC2 1.079 PC3 1.521 Mass PC MPC1 -1.746</p>	<p>Key</p>  <p>log(mD)</p>	

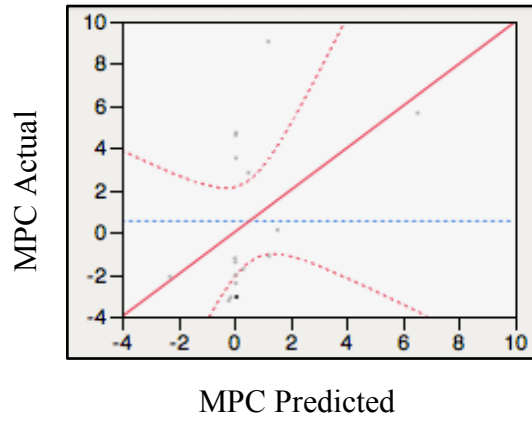


Figure 3.3 Multivariate linear prediction of mass Principal Component by permeability Principal Components, R^2 adjusted = 0.036, RMSE = 3.7

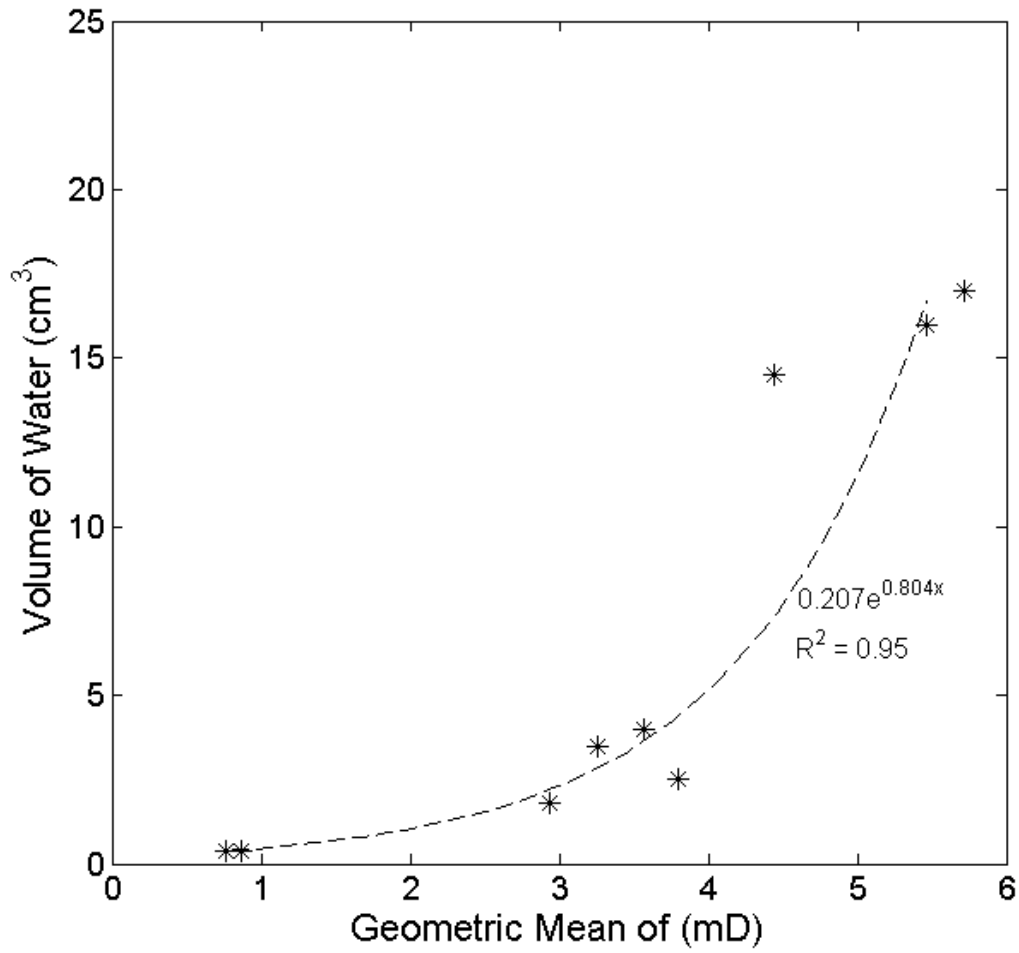


Figure 3.4 Prediction of mass wicked at 50 minutes by geometric mean of surface permeability for uniform, low permeability materials, $R^2 = 0.95$

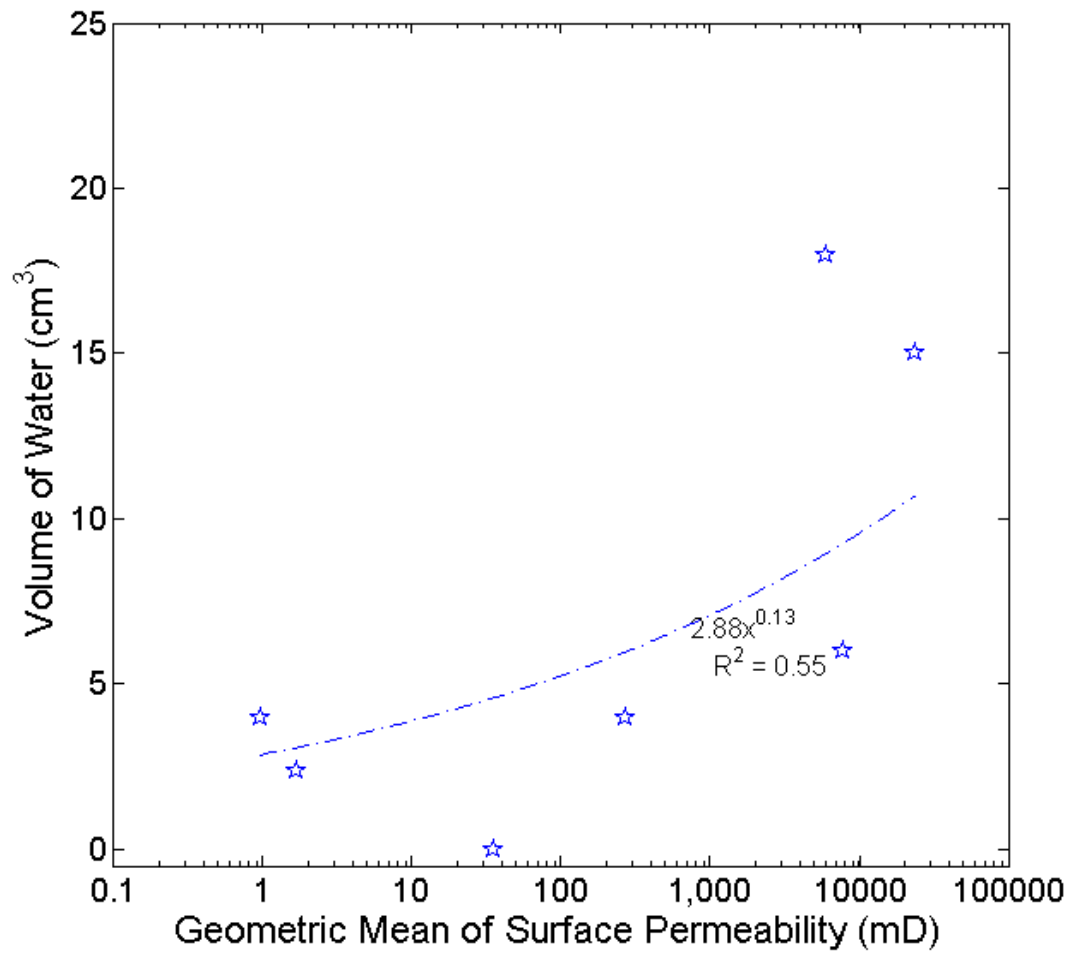


Figure 3.5 Prediction of mass wicked at 50 minutes by geometric mean of surface permeability for non-uniform materials, $R^2 = 0.55$

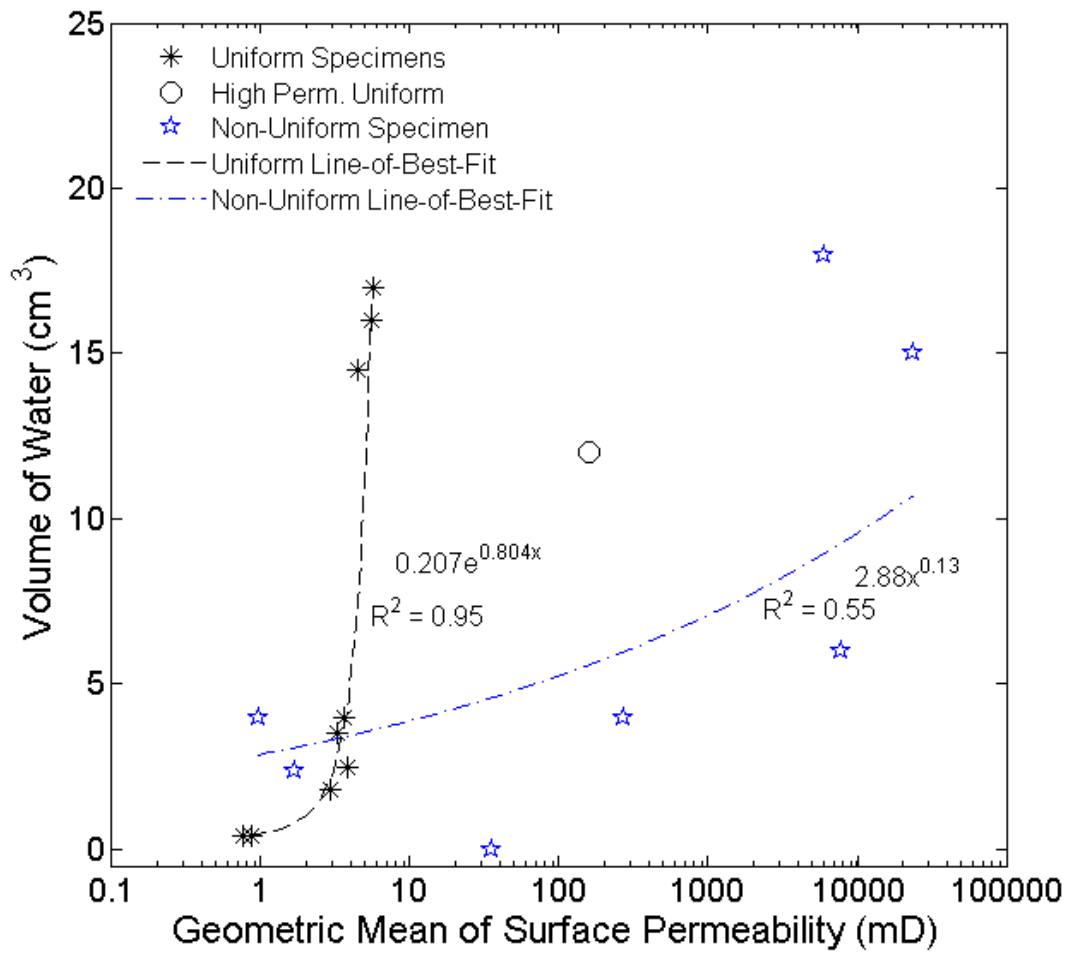


Figure 3.6 Mass wicked at 50 minutes by geometric mean of surface permeability for all materials and their respective relationships

CHAPTER 4: SUMMARY AND FUTURE WORK

In this thesis we analyzed the results of a versatile surface permeameter, the AutoScan II, and assessed its usefulness in determining surface permeabilities of a variety of porous building materials and estimating fluid transport within these materials. In Chapter 2, it was shown that the AutoScan II could measure surface permeability across many different materials at varying resolutions with minimal experimenter involvement. The results can be highly detailed and benefit from the use of geostatistics to characterize the spatial homogeneity of the data, anisotropy, and spatial autocorrelation. It was found that a second surface permeameter suitable for field use, the TinyPerm II, is capable of characterizing specimens, using the geometric mean, in a manner similar to the AutoScan II. Characterizations of 16 different specimens by the two devices were highly correlated.

Chapters 2 and 3 examine practical applications for surface permeametry. It was found that the structurally uniform materials tested here have similar surface and macroscopic gas permeabilities, but surface permeability is non-destructive and significantly easier to measure than the macroscopic gas permeability. Thus, surface permeability measurements may be used as a surrogate for macroscopic gas permeability. More research is needed to determine if the surface permeability of non-uniform (with aggregates) materials can be used in the same manner. It is possible that a geometric correction factor or a regression model may produce a useable relationship.

It was found that engineered materials that have undergone weathering tended to have higher surface permeabilities than prior to weathering while natural materials tended to maintain their surface permeability over the same number of freeze-thaw cycles. This effect was found regardless of the material's surface permeability before weathering. We hypothesize that the increased surface permeability in engineered materials is indicative of larger void spaces or cracks caused by the weathering, which would mean that aggregate particles might have separated from the cement in some places.

Finally, we studied the relationship between surface permeability and wicking. Capillary forces are affected by a number of factors, and it is likely that the surface permeability values used in this study were too broad to find a unique relationship between all of the permeabilities and wicking. Focusing on specimens with a smaller range of surface permeability values and similar structure reduced some of the non-linear dynamics associated with pore size in the wicking equation and allowed us to find a relationship between wicking and surface permeability. This relationship was observed over a small range of permeabilities (<10 mD) and was confined to relatively uniform materials. Future work should look at many specimens within similar permeability ranges. A study examining the pore structures of the various porous building materials at the microscopic level would benefit this investigation. The technique of X-ray computed tomography could be employed for this purpose.

REFERENCES

- [1] Anand, K. B., Vasudevan, V., and Ramamurthy, K. (2003). “Water permeability assessment of alternative masonry systems.” *Building and Environment*, 38(7), 947–957.
- [2] ASTM International. (2002), *Annual Book of ASTM Standards: section four, volume 04.08. Soil and Rock (I)*.
- [3] Brownell, M., Dewoolkar, M., Hayden, N., Rizzo, D., and Porter, D. (2006). “Interactions of Contaminating Agents with Building Materials: Literature Review and Preliminary Experiments.” Report.
- [4] Chandler, M. A., Goggin, D. J., and Lake, L. W. (1989) A mechanical field permeameter for making rapid, non-destructive, permeability measurements, *J. Sediment. Petrol.*, 59, 613–615.
- [5] Cressie, N. A. C. (1993). *Statistics for Spatial Data*. Wiley series in probability and mathematical statistics, Wiley, New York.
- [6] Dandekar, A. Y. (2006), *Petroleum reservoir rock and fluid properties*. CRC Press, 496. ISBN 0849330432.
- [7] Davis, J. M., Wilson, J. L., and Phillips, F. M. (1994) A portable air-minipermeameter for rapid in situ field measurements, *Ground Water*, 32, 258–266.

- [8] Dreyer, T., Scheie, A., and Jensen, J. L. (1990) Minipermeameter-based study of permeability trends in channel sand bodies, AAPG Bull., 74, 359–374.
- [9] Dullien, F. A. L. (1992), Porous Media Fluid Transport and Pore Structure, 2nd ed. Academic Press, 574. ISBN 0122236505.
- [10] Dutton, S. P. and Willis, B. J. (1998) Comparison of outcrop and subsurface sandstone permeability distribution, Lower Cretaceous Fall River Formation, South Dakota and Wyoming, J. Sediment. Res., 68, 890–900.
- [11] Dykstra, H. & Parsons, R. 1950 The prediction of oil recovery by waterflood. Secondary recovery of oil in the United States. J. Pet. Tech. 8, 55–56.
- [12] Eijpe, R. and Weber, K. J. (1971) Mini-permeameters for consolidated rock and unconsolidated sand, AAPG Bull., 55, 307–309.
- [13] Figg J. W. (1972). Determining the water content of concrete panels. *Magazine of Concrete Research*. 24(79): 94-96.
- [14] Filomena, C. M., J. Hornung, and H. Stollhofen (2013) Assessing accuracy of gas-driven permeability measurements: a comparative study of diverse Hassler-cell and probe permeameter devices, Solid Earth Discuss., 5, 1163–1190.
- [15] Fossen, H., Schultz, R. A., and Torabi, A. (2011) Conditions and implications for compaction band formation in the Navajo Sandstone, Utah, J. Struct. Geol., 33, 1477–1490.
- [16] Gladden, L. F., M. H. M. Lim, M. D. Mantle, A.J. Sederman, and E. H. Stitt (2003), MRI visualization of two-phase flow in structured supports and trickle-bed reactors, Catalysis Today 79, doi:10.1016/S0920-5861(03)00006-3.

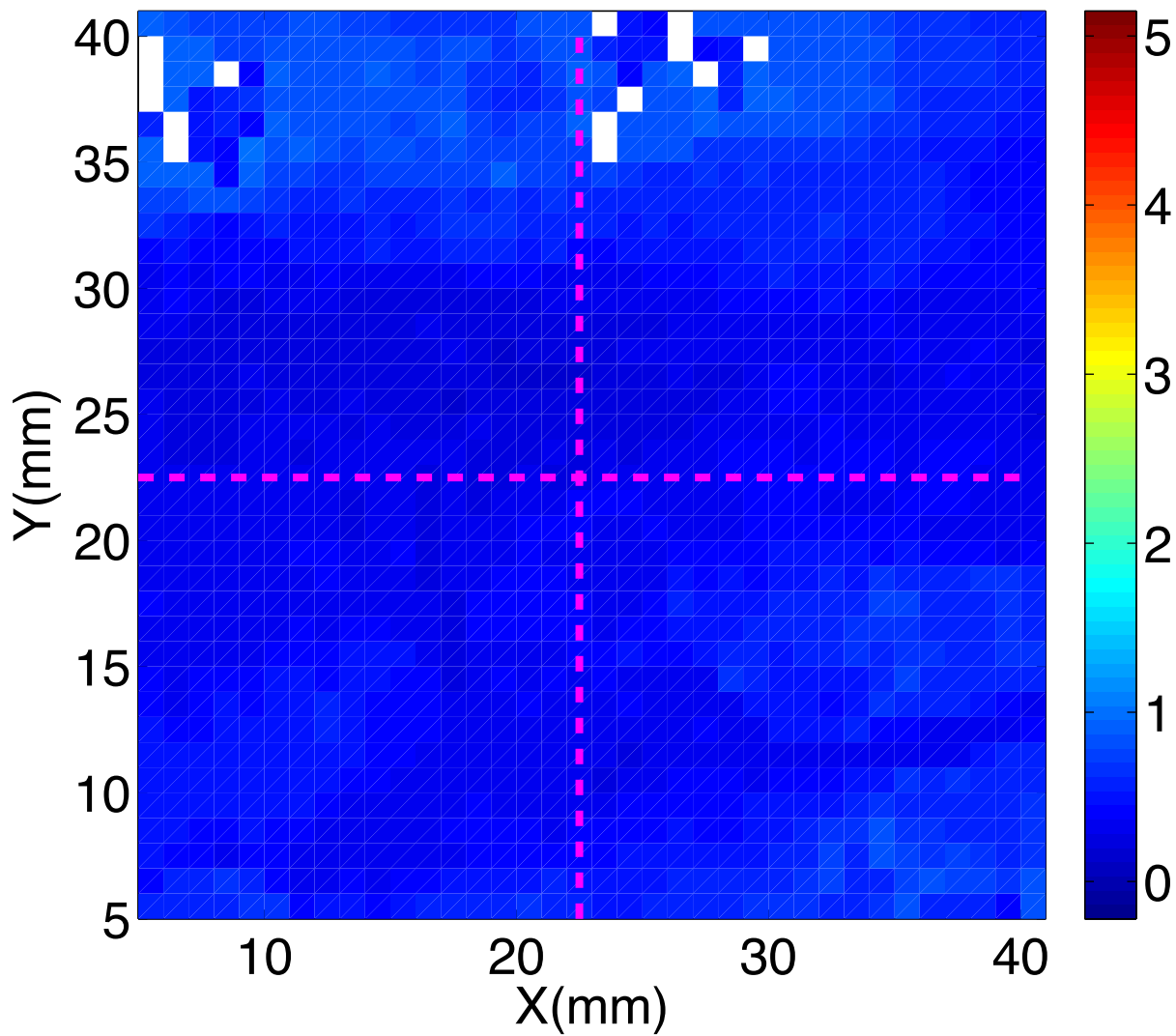
- [17] Goggin, D. J. (1993) Probe permeametry: is it worth the effort?, *Mar. Petrol. Geol.*, 10, 299–308.
- [18] Goggin, D.J., R.L. Thrasher, and L. W. Lake (1988), A theoretical and experimental analysis of minipermeameter response including gas slippage and high velocity flow effects, *In Situ*, 12, 79-116.
- [19] Goovaerts, P., (1998) Geostatistical tools for characterizing the spatial variability of microbiological and physico-chemical soil properties *Biol Fertil Soils*, 27: 315–334.
- [20] Hornung, J. and Aigner, T. (2002) Reservoir architecture in a terminal alluvial plain: an outcrop analogue study (Upper Triassic, Southern Germany). Part 1: Sedimentology and petrophysics, *J. Petrol. Geol.*, 2, 3–30.
- [21] Huysmansa, M., Peetersa, L., Moermansa, G., and Dassarguesa, A. (2008) Relating small-scale sedimentary structures and permeability in a cross-bedded aquifer, *J. Hydrol.*, 361, 41–51.
- [22] Isaaks, E. H. and Srivastava, R. M. (1989), *Introduction to applied geostatistics*, Oxford Press, New York, 561 pp.
- [23] Iversen, Bo V., P. Moldrup, P. Schjønning, and O. H. Jacobsen (2003) Field Application of a Portable Air Permeameter to Characterize Spatial Variability in Air and Water Permeability, *Vadose Zone Journal* 2:618–626.
- [24] Jang, S. H., M. G. Wientjes, D. Lu, and L. S. A. Jessie (2003), Drug delivery and transport to solid tumors, *Pharmaceutical Research*, 20 (9), 1337-1350.

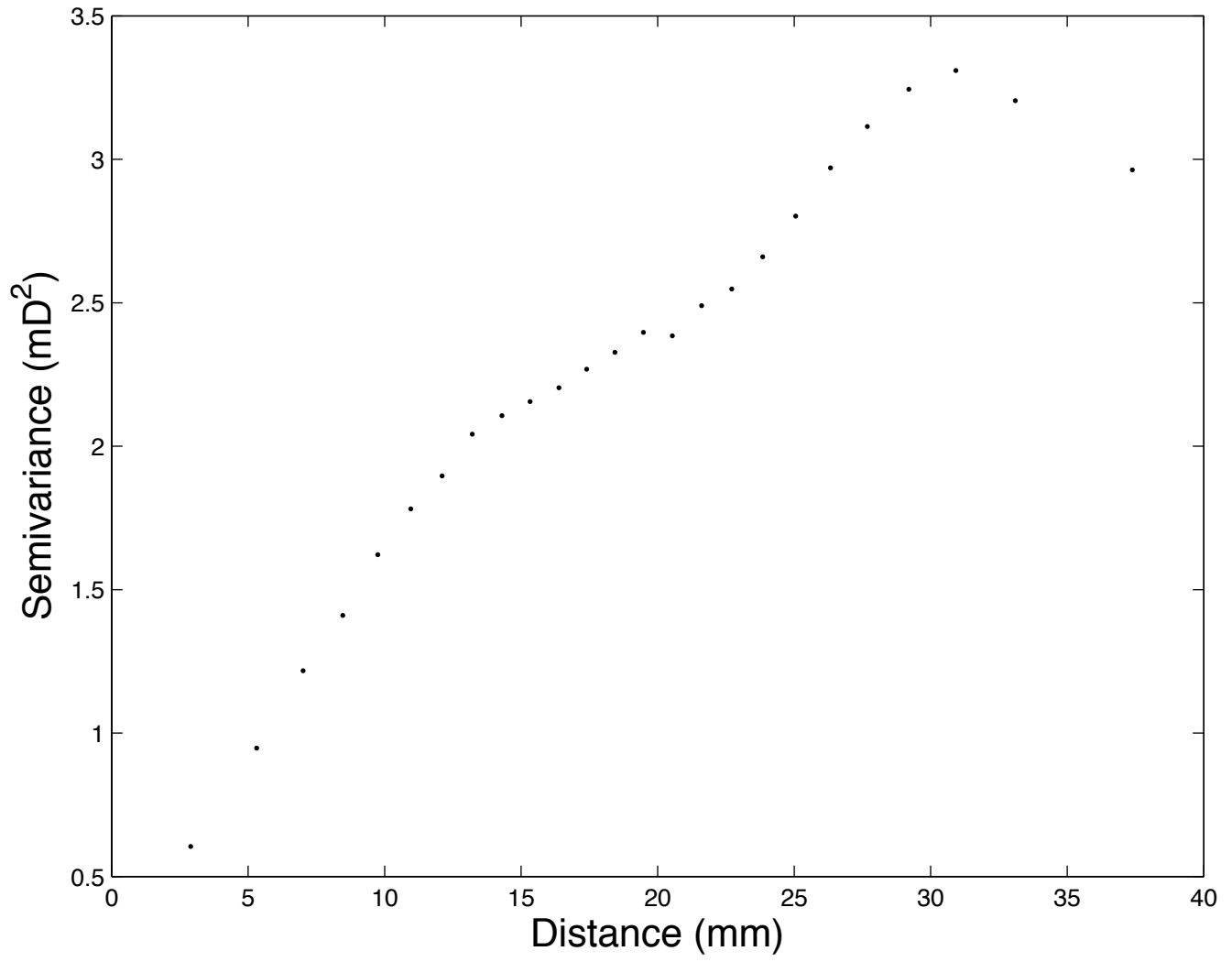
- [25] Klinkenberg, L. J. (1941), The permeability of porous media to liquids and gases, *Drilling and Productions Practices*, 200-213.
- [26] Lomborg, Bjørn (2000). *The Skeptical Environmentalist: Measuring the Real State of the World*. Cambridge University Press, 138. ISBN 0521804477.
- [27] Navaz, H. K., Markicevic, B., Zand, A. R., Sikorski, Y., Chan, E., Sanders, M., and D’Onofrio, T. G. (2008). “Sessile droplet spread into porous substrates—Determination of capillary pressure using a continuum approach.” *Journal of Colloid and Interface Science*, 325(2), 440–446.
- [28] New England Research, Inc., (2008), *AutoScan Automatic Multi-Sample Measurement Platform; Gas Permeability manual*.
- [29] Paulini, P., and F. Nasution (2007), *Air Permeability of near-surface concrete, Consec ’07 Tours, France*, 8pp.
- [30] Pinder, G. F. and W. G. Gray (2008). *Essentials of Multiphase Flow and Transport in Porous Media*. Wiley, Hoboken, N.J.
- [31] Rogiers, B., Beerten, K., Smeekens, T., and Mallants, D. (2011) *Air permeability measurements on Neogene and Quaternary sediments from the Campine area: using outcrop analogues for determining hydrodynamic aquifer properties*, Belgian Nuclear Research Center, Mol, Belgium, External Report SCKCEN-ER-177.
- [32] Selvadurai, A. P. S. and P. A. Selvadurai (2010) *Surface permeability tests: experiments and modelling for estimating effective permeability*, *Proc. R. Soc. A* doi:10.1098/rspa.2009.0475.

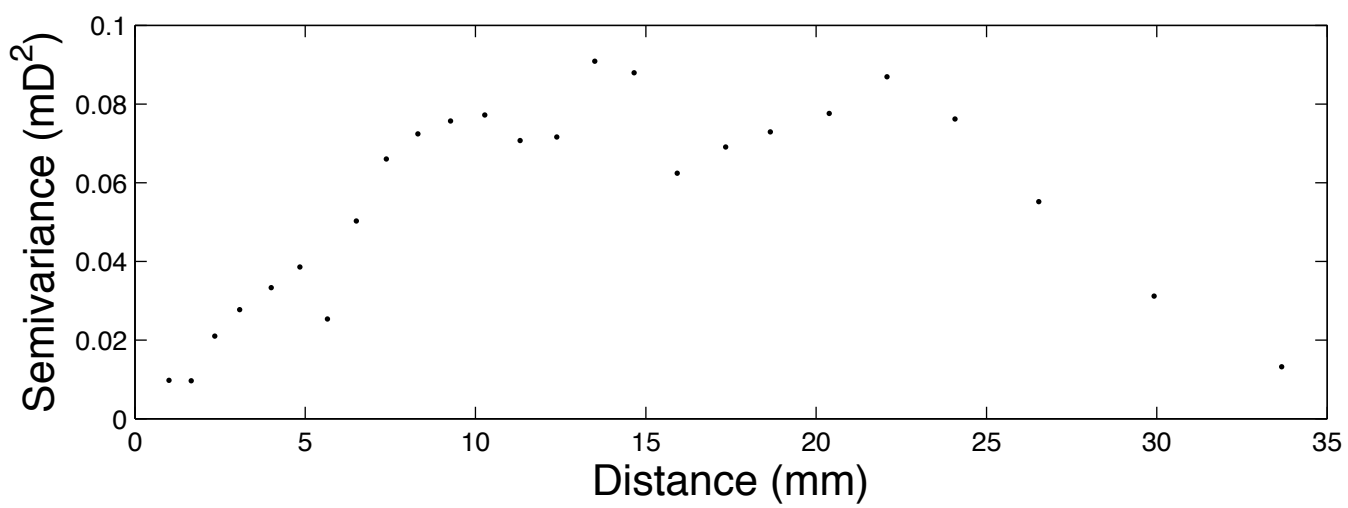
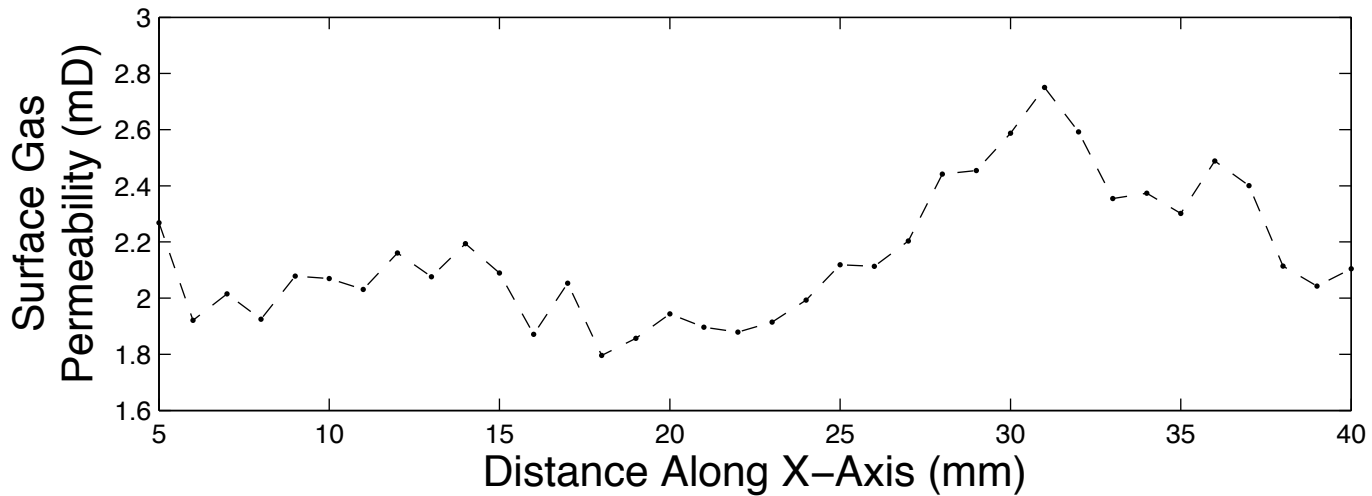
- [33] Sharp Jr., J. M., Fu, L., Cortez, P., and Wheeler, E. (1994) An electronic minipermeameter for use in the field and laboratory, *Ground Water*, 32, 41–46.
- [34] Staples, T. L., and Shaffer, D. G. (2002). “Wicking flow in irregular capillaries.” *Colloids and Surfaces A: Physicochemical and Engineering Aspects*, 204(1–3), 239–250.
- [35] Steele, B. C. H., and A. Heinzl (2001), *Materials for fuel-cell technologies*, *Nature*, 414, 345-352.
- [36] Valek, J., J. J. Hughes and P. J. M. Bartos, (2000), Portable probe gas permeability: a non-destructive test for the in-situ characterization of historic masonry, *Mat. and Struc.*, 33, 194-197.
- [37] Washburn, E. W. (1921). “The Dynamics of Capillary Flow.” *Physical Review*, 17(3), 273–283.
- [38] Zaharieva, R., B.B. François, S. Frederic and E. Wirquin (2003), Assessment of the surface permeation properties of recycled aggregate concrete, *Cement & Concrete Composites*, 25, 223-232.

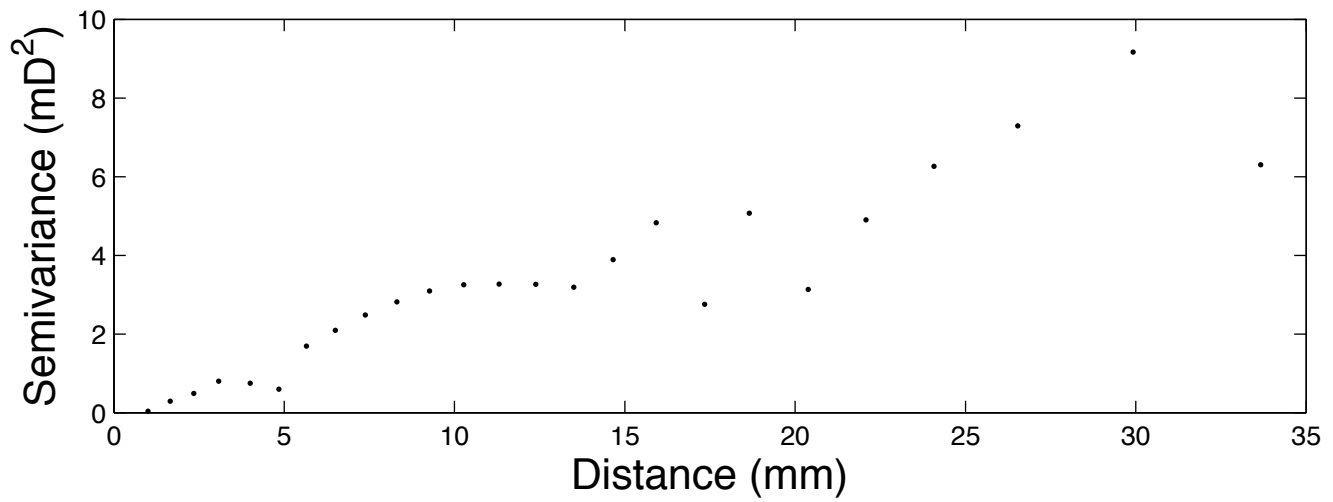
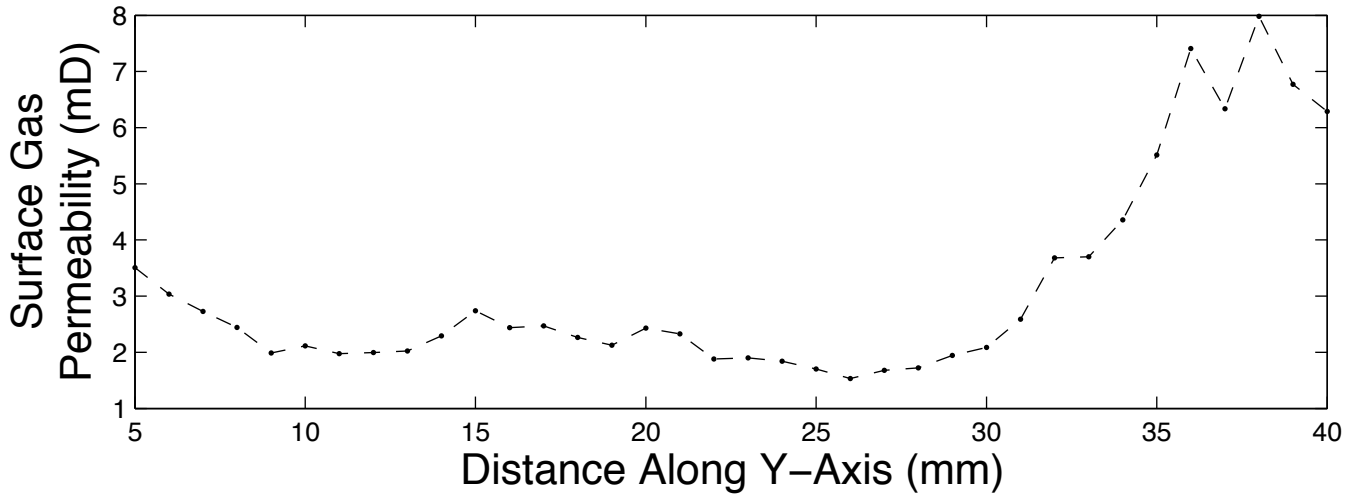
Appendix

Arkose Sandstone

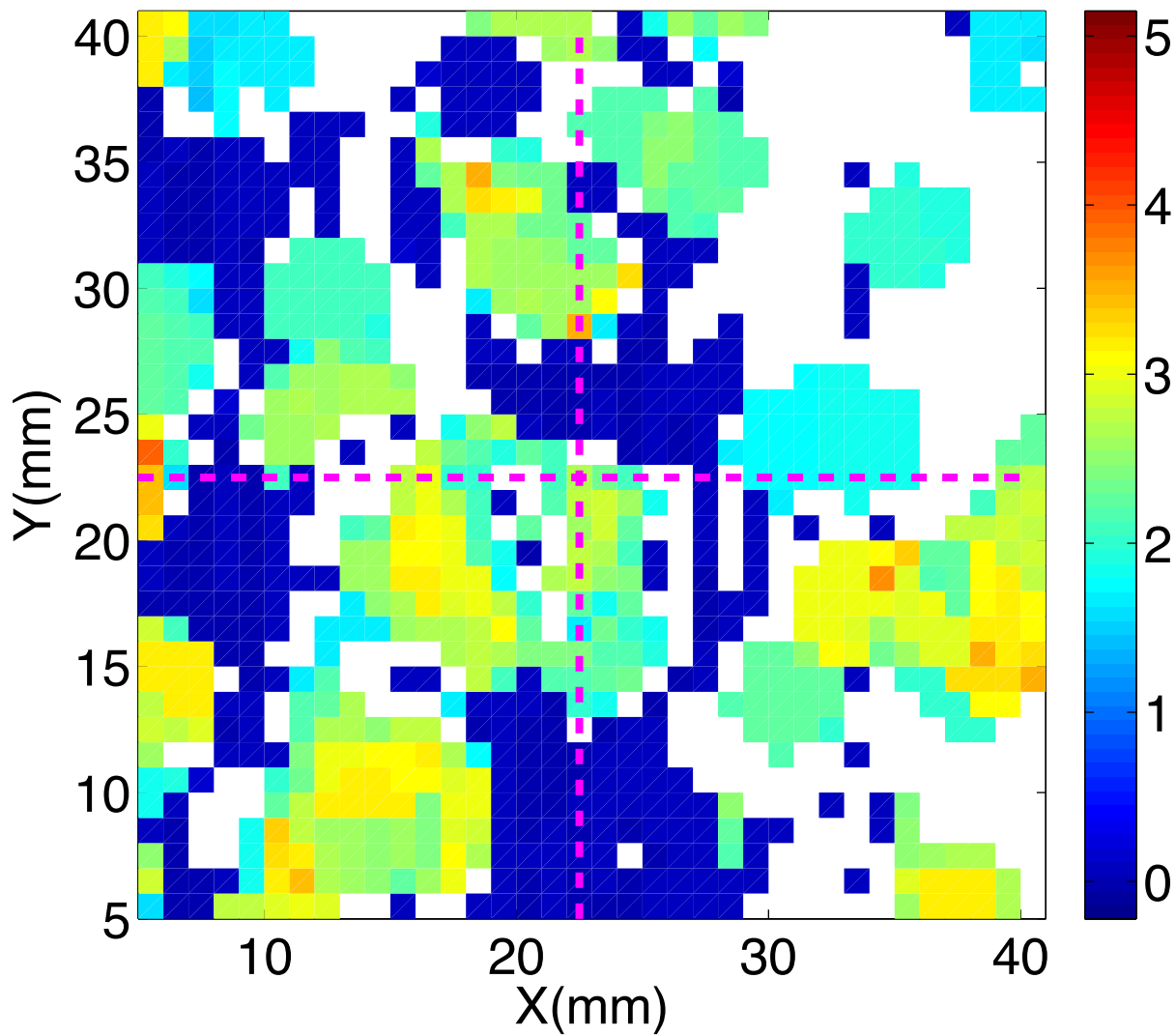


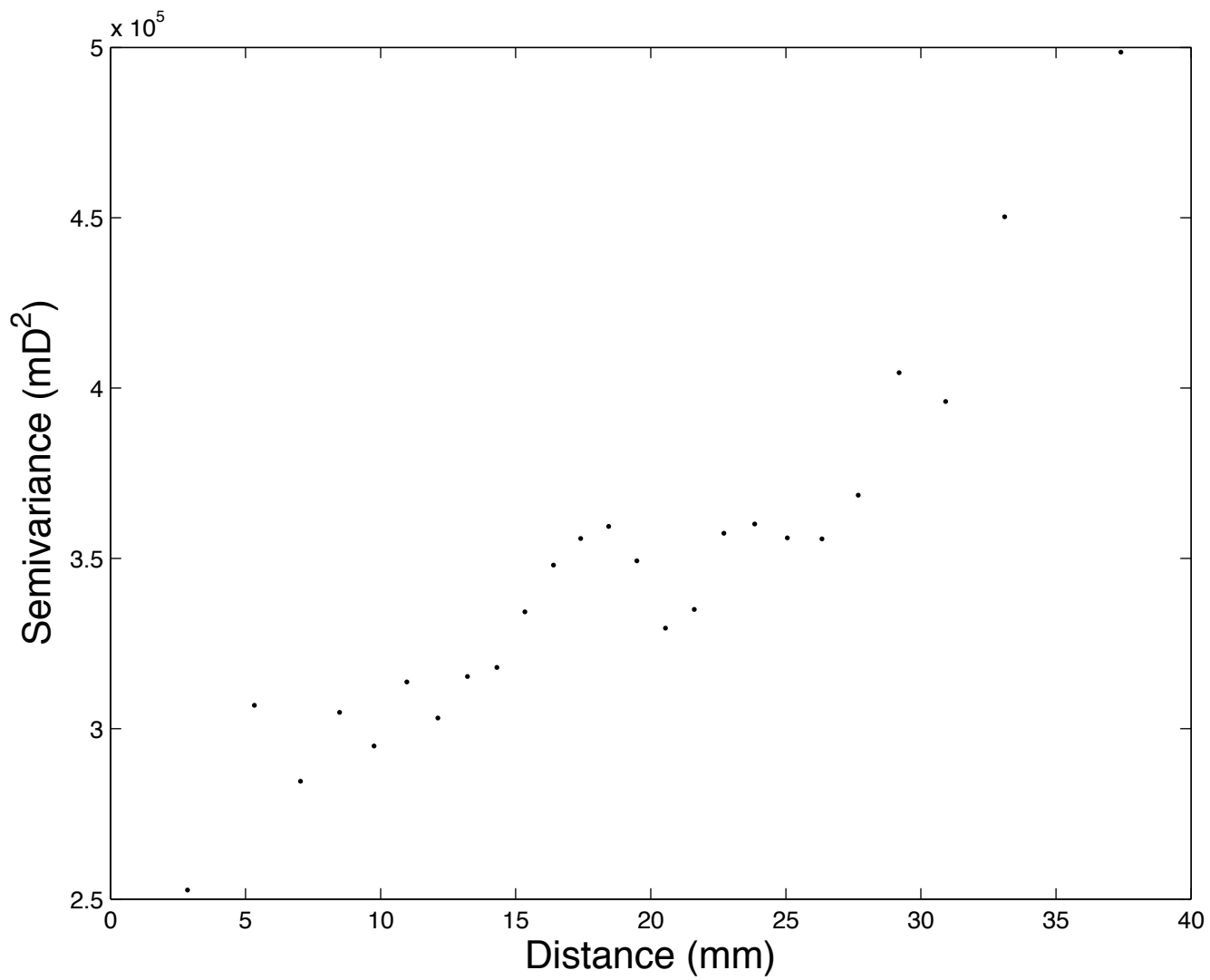


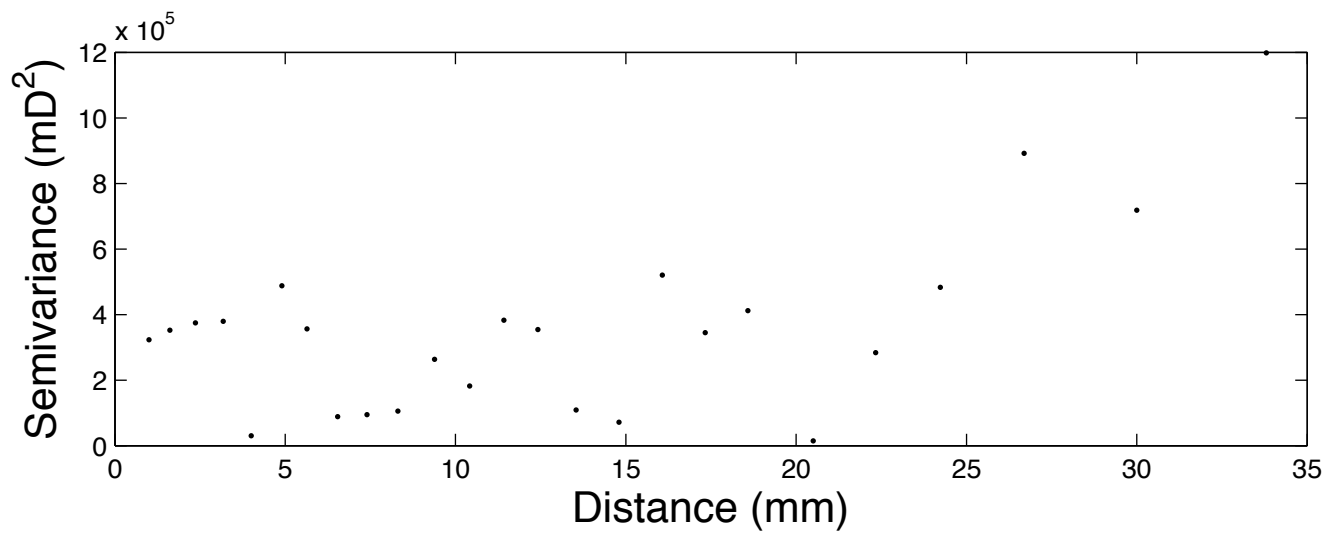
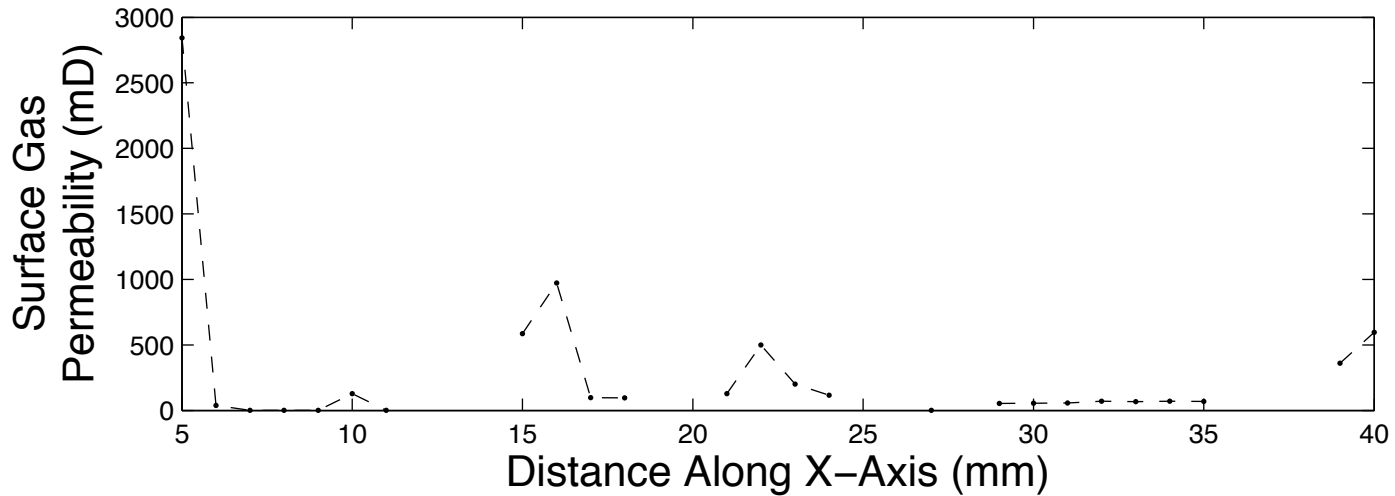


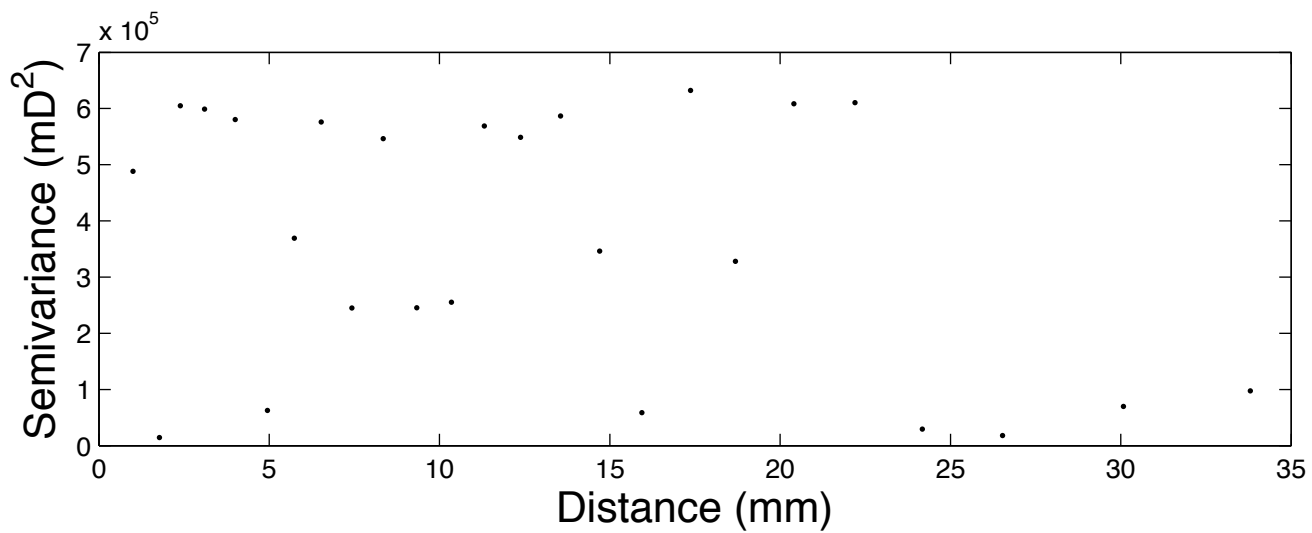
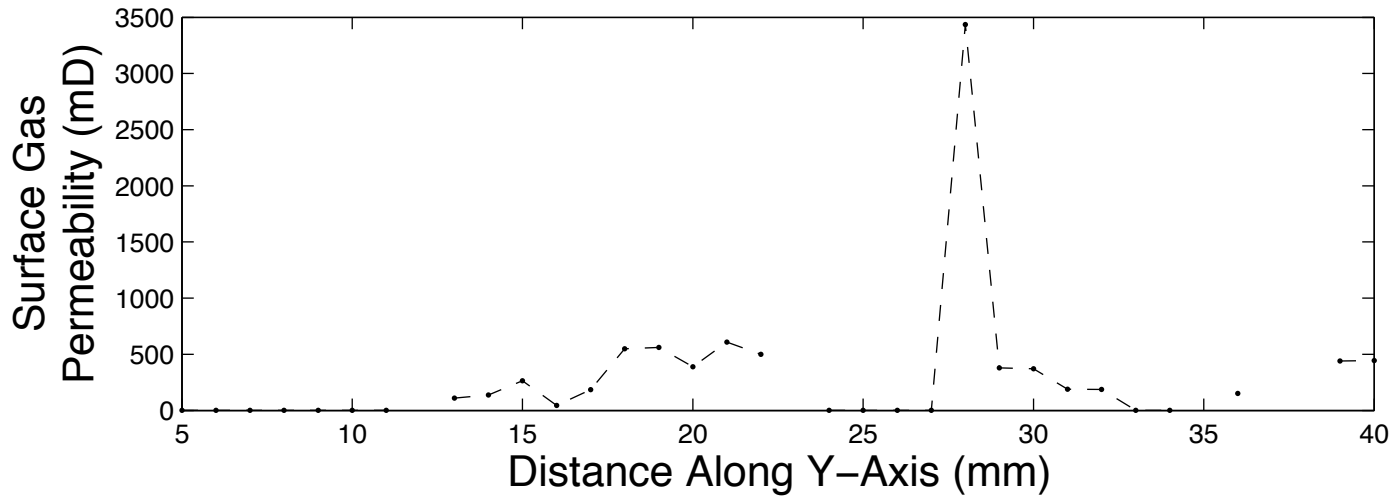


Asphalt

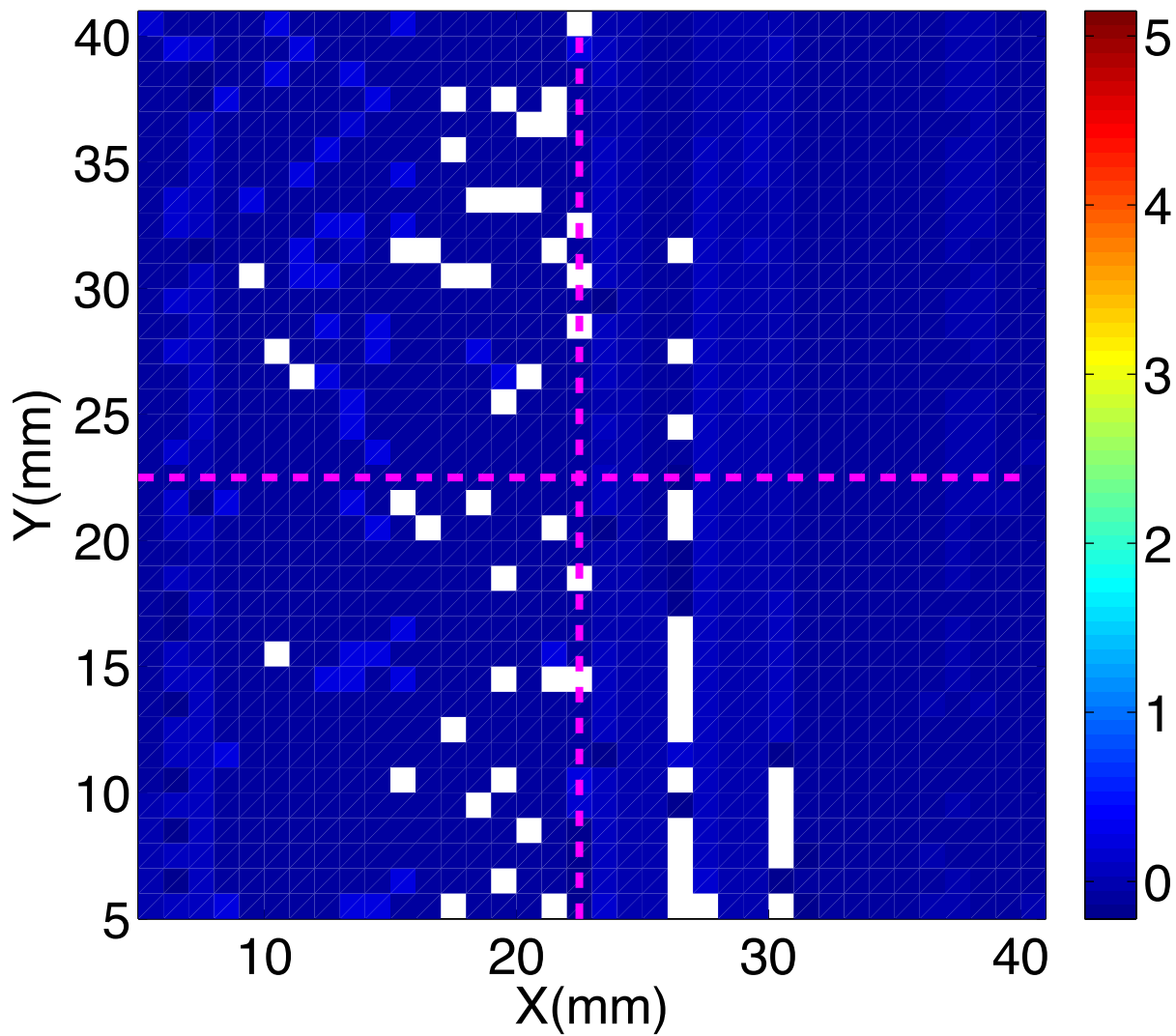


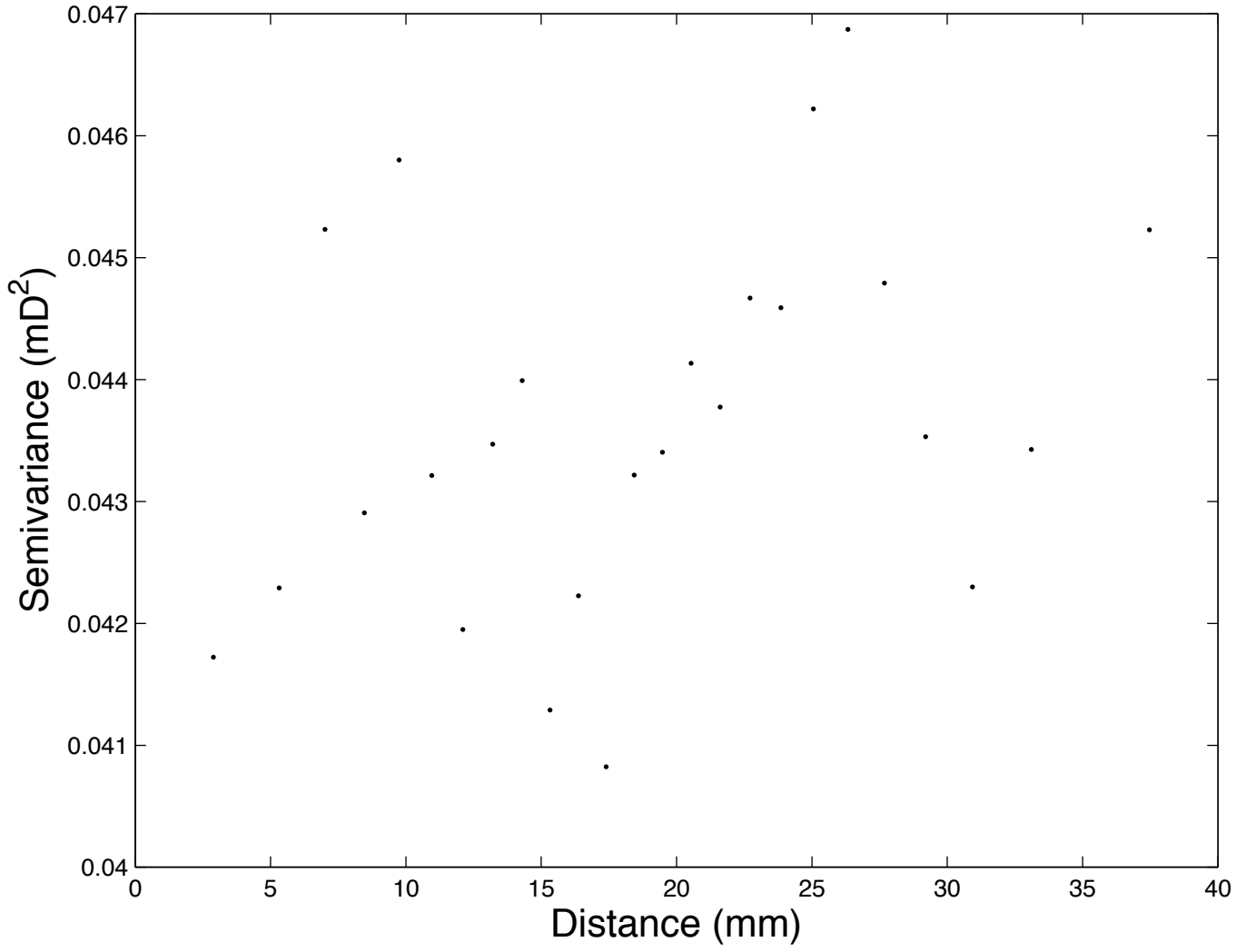


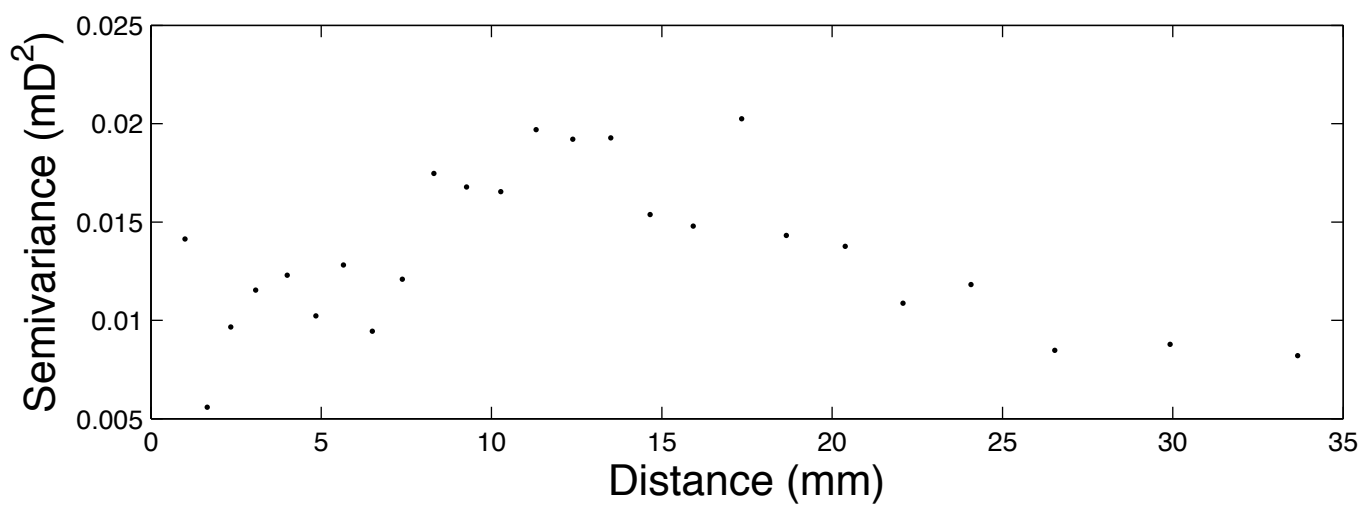
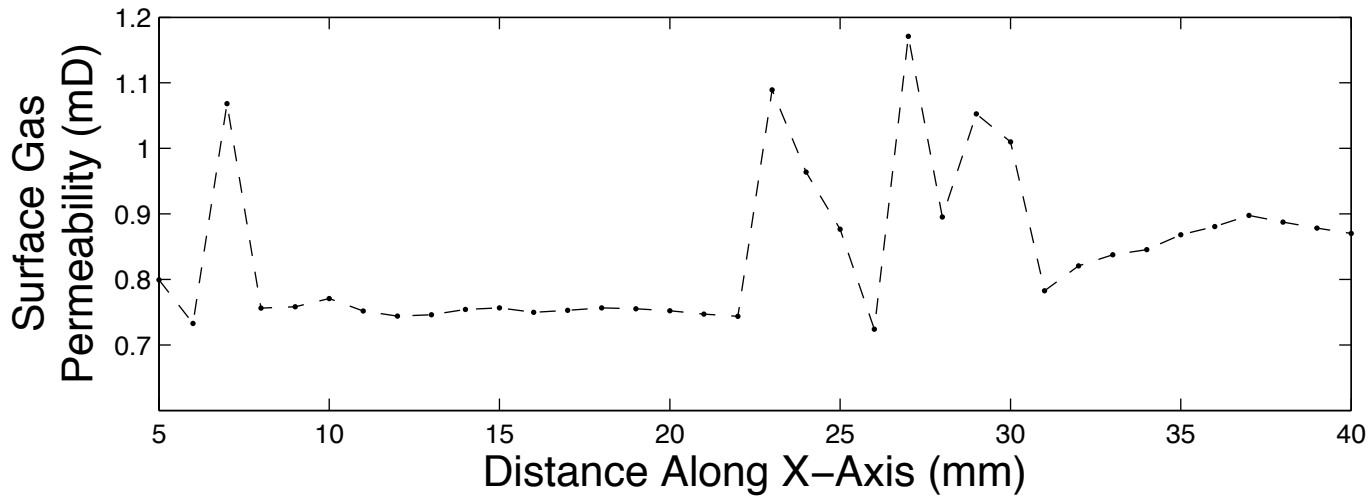


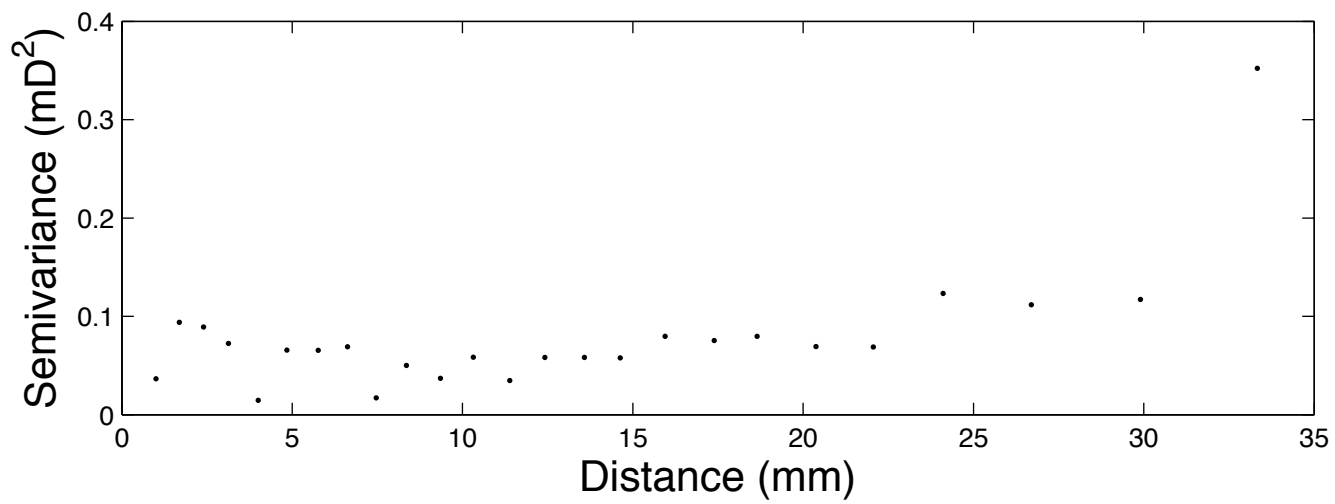
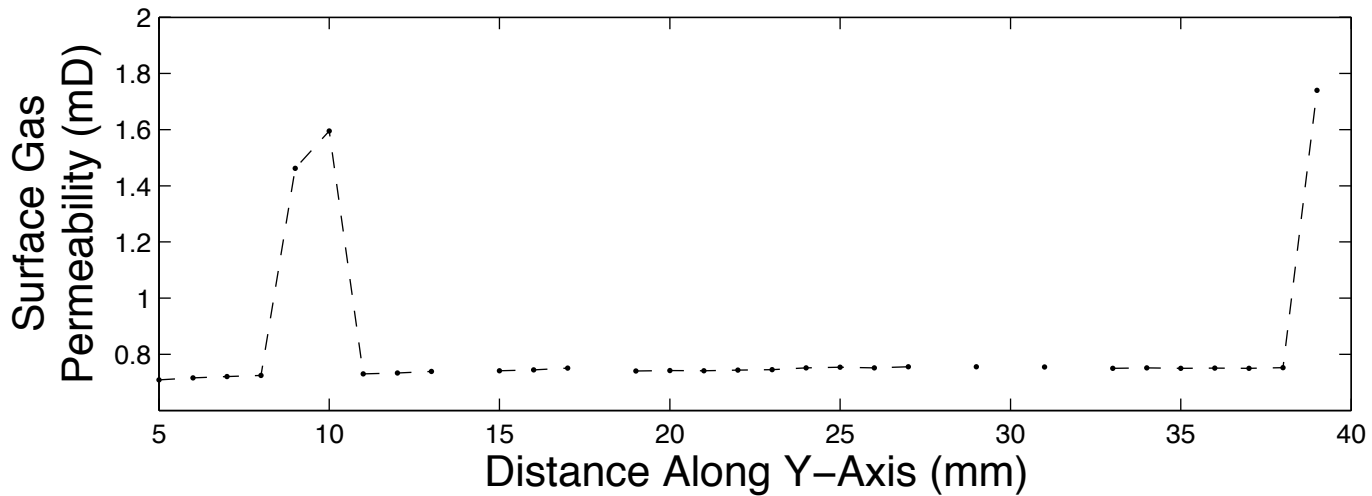


Bluestone

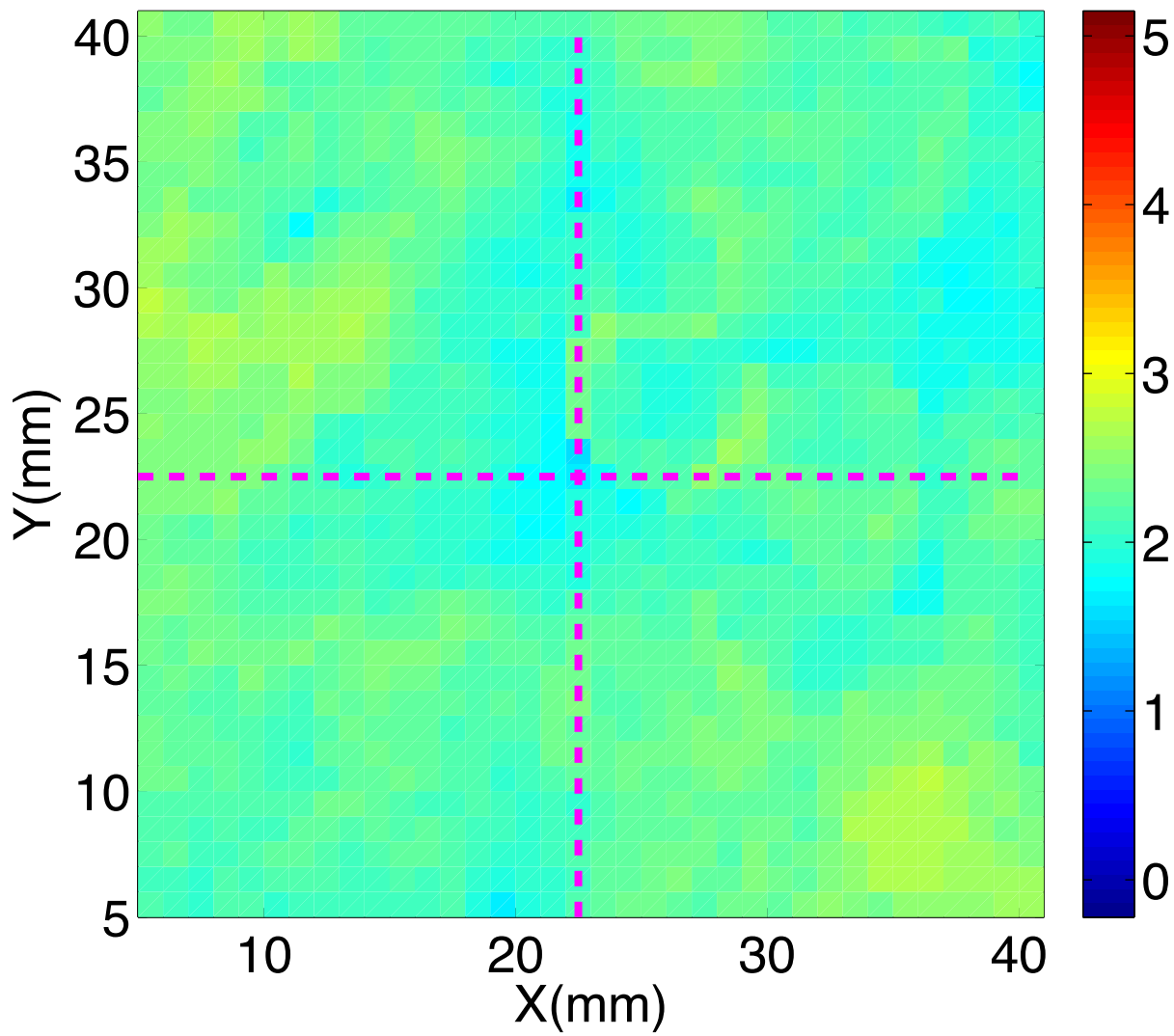


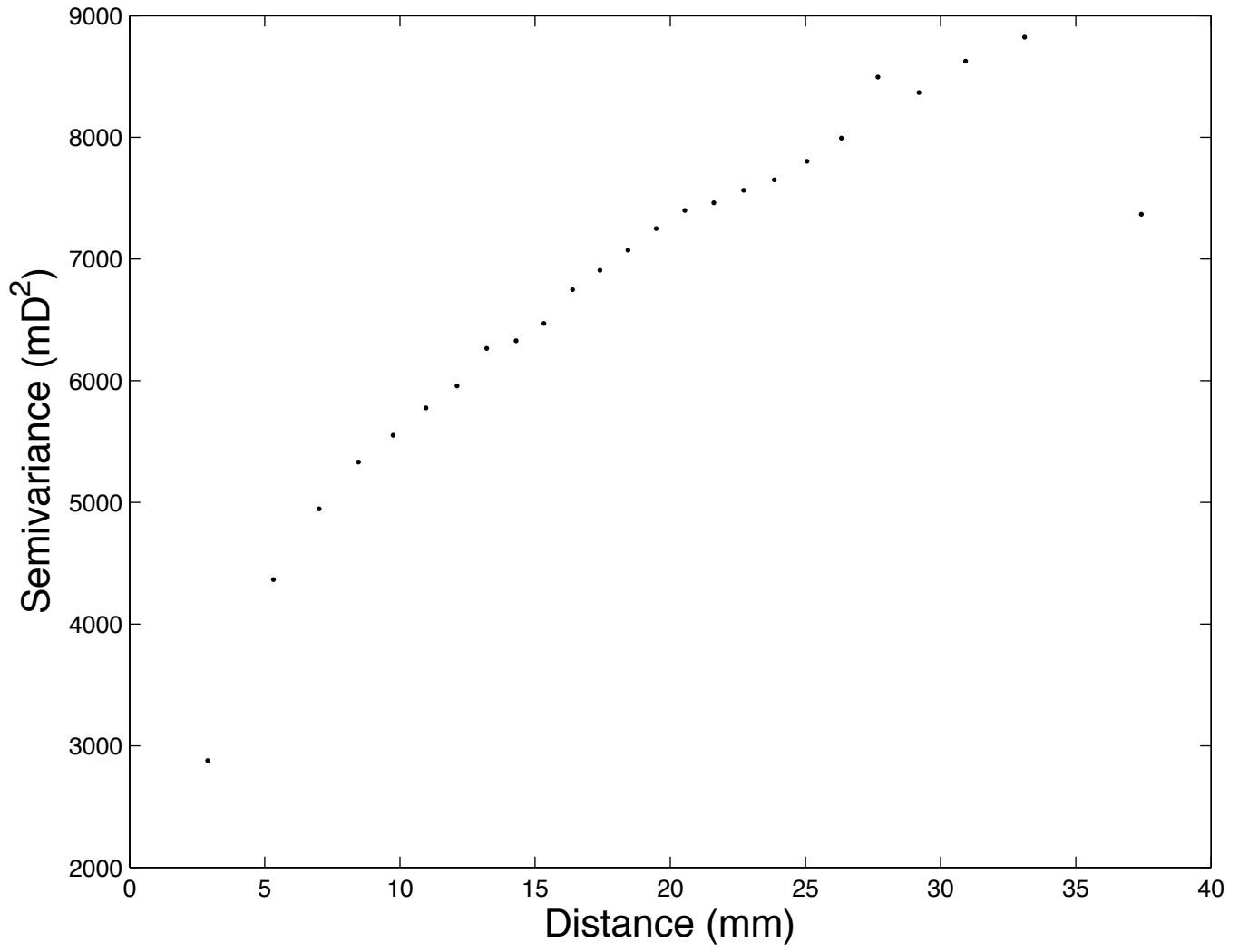


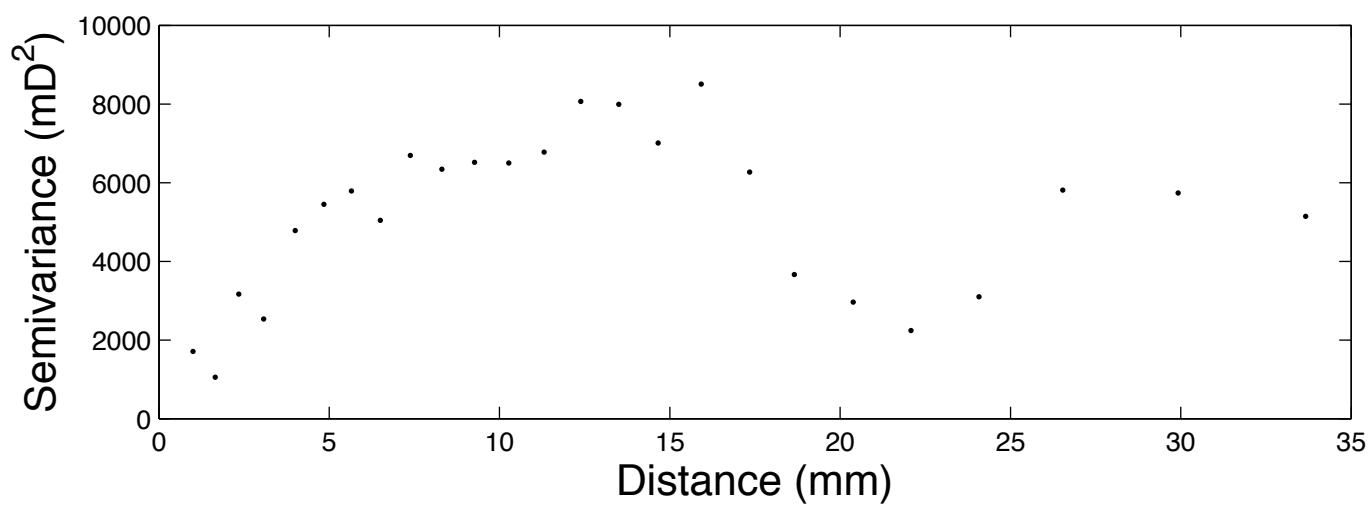
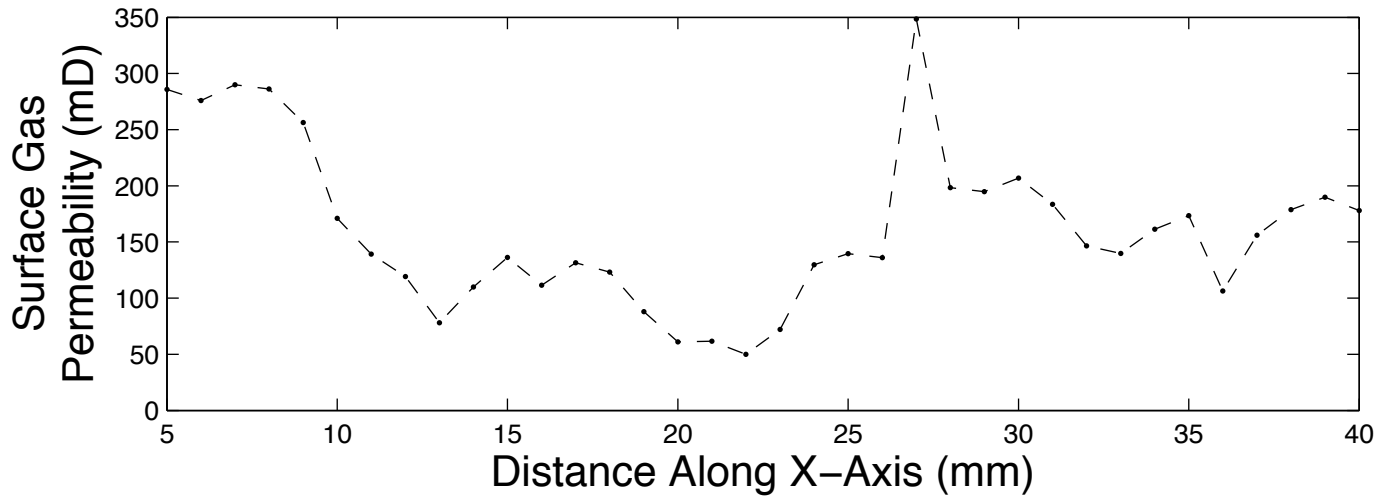


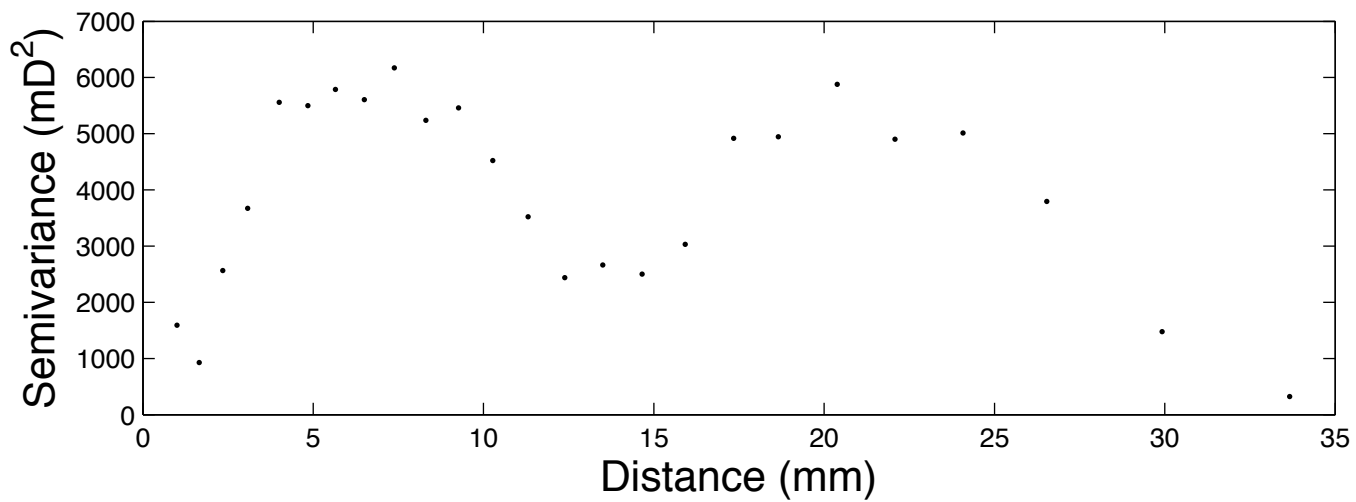
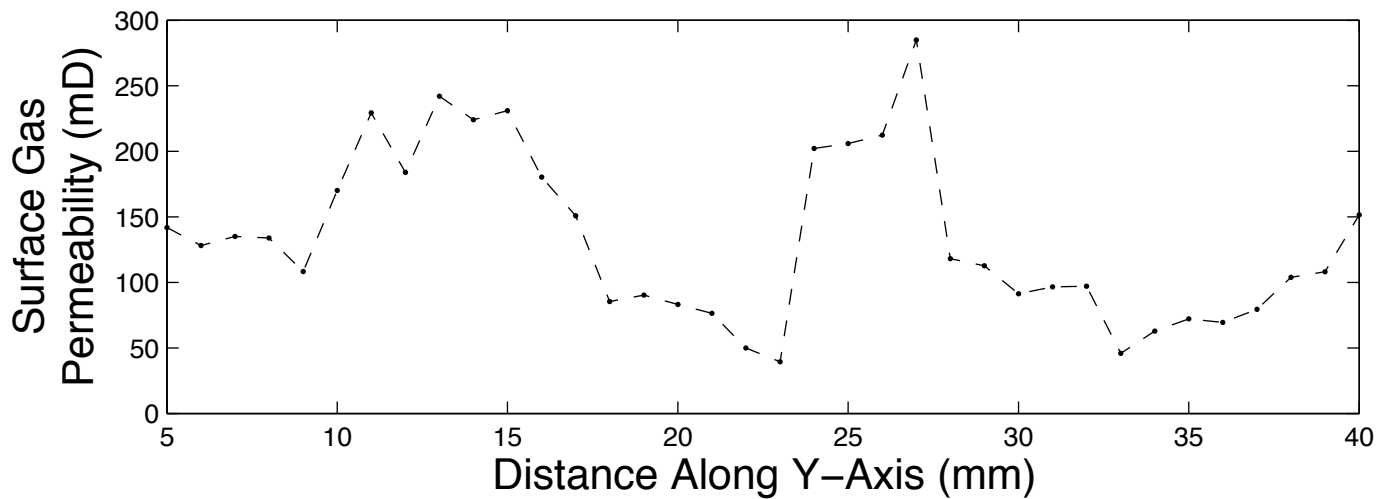


Buff Indiana Limestone

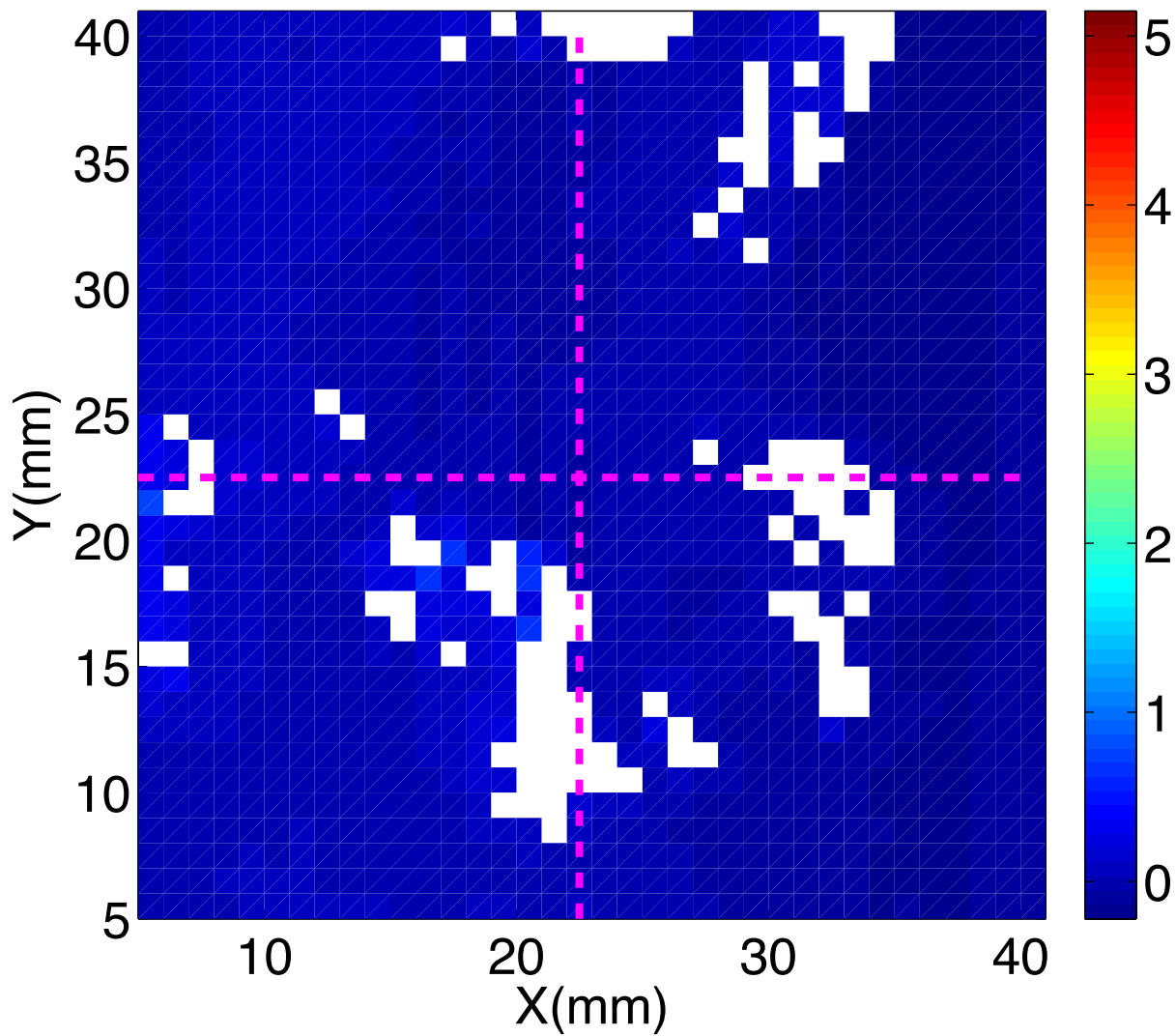


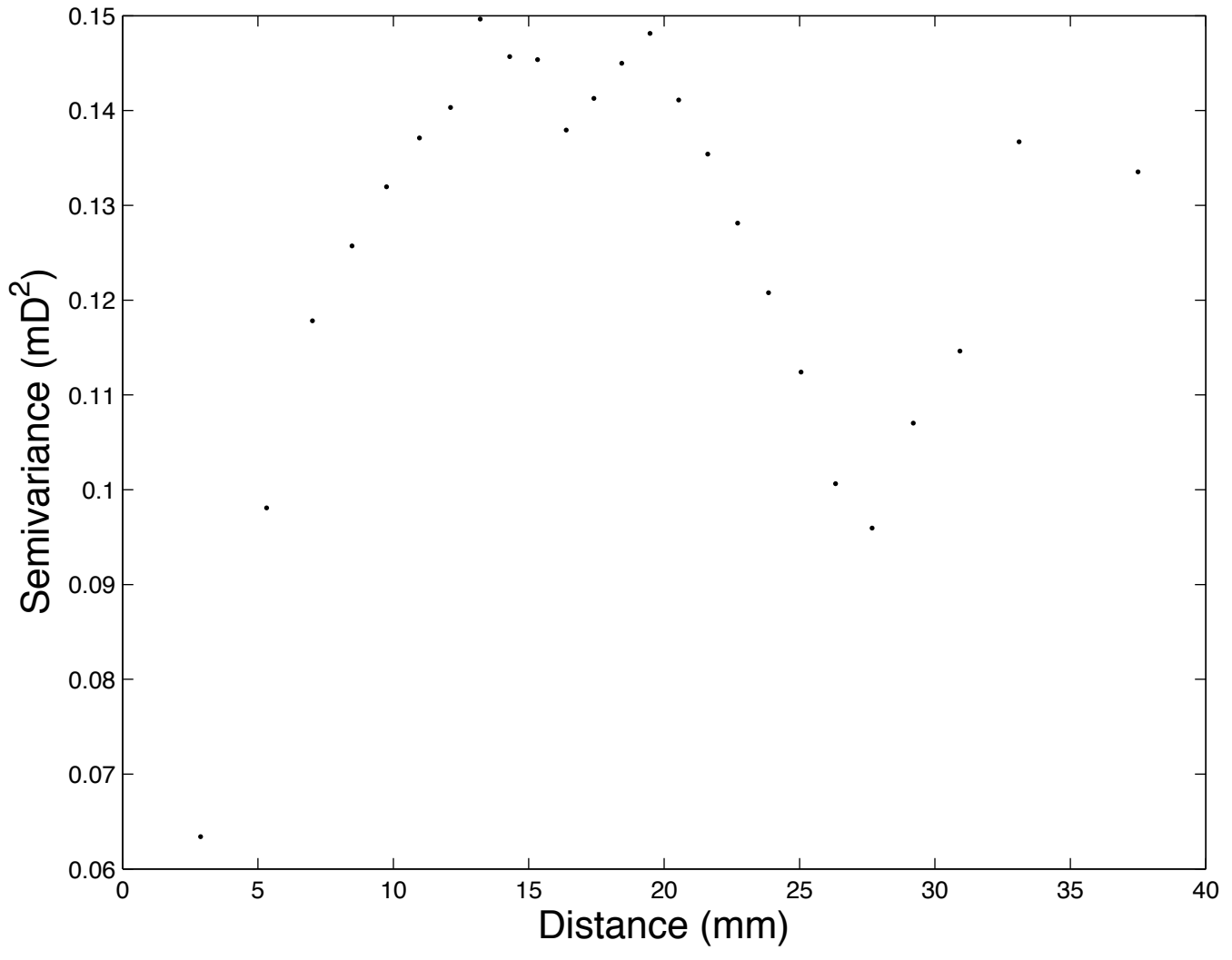


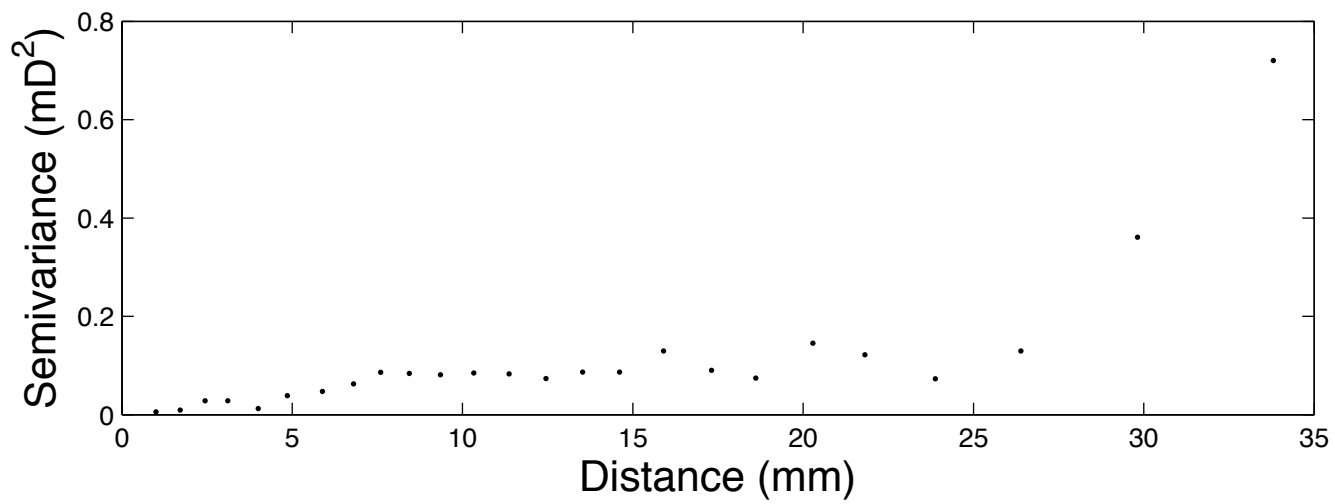
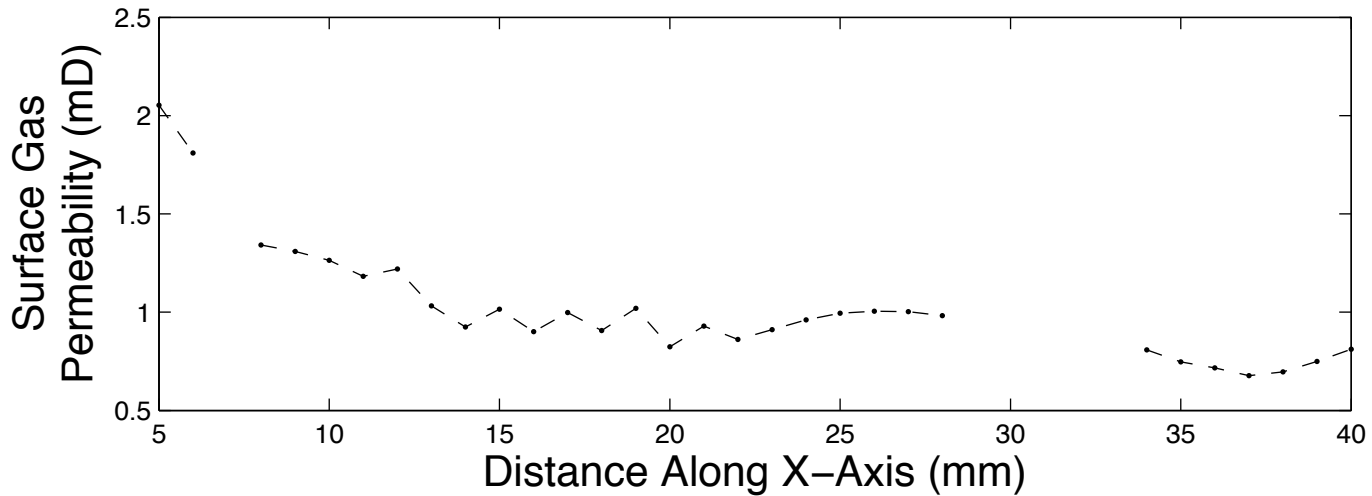


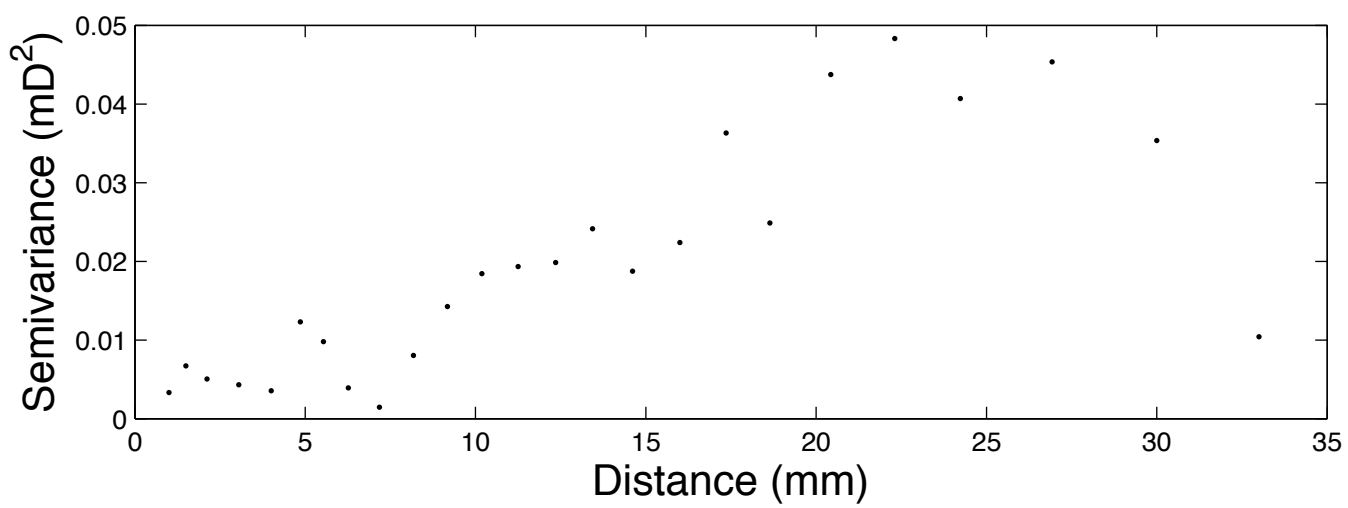
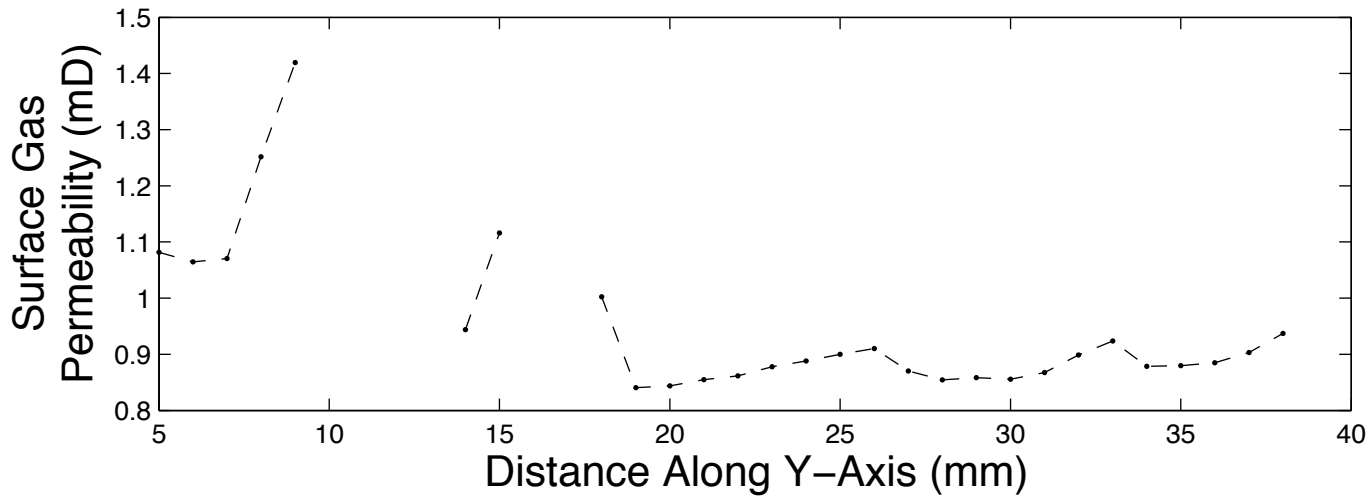


Concrete 3k PSI

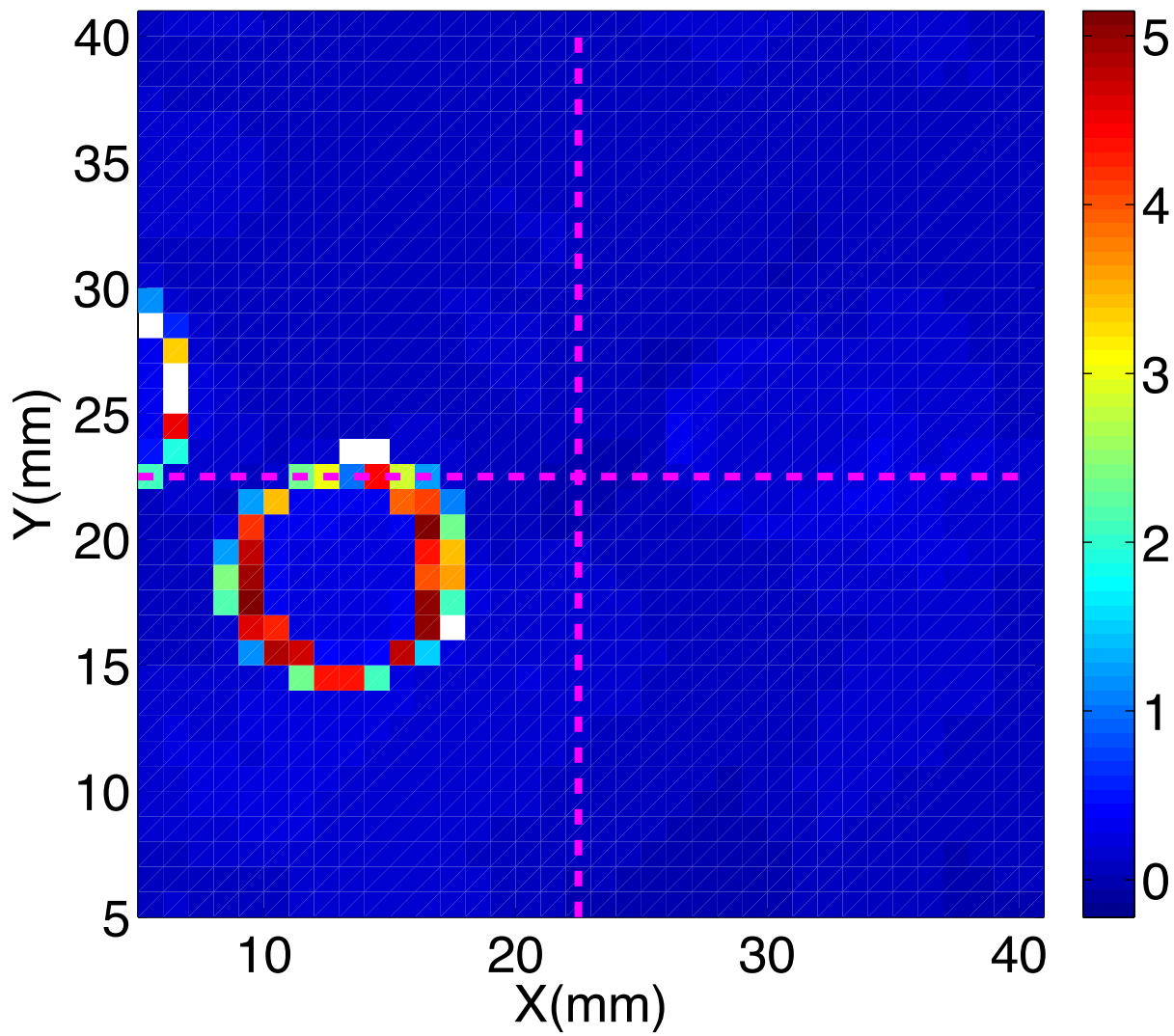


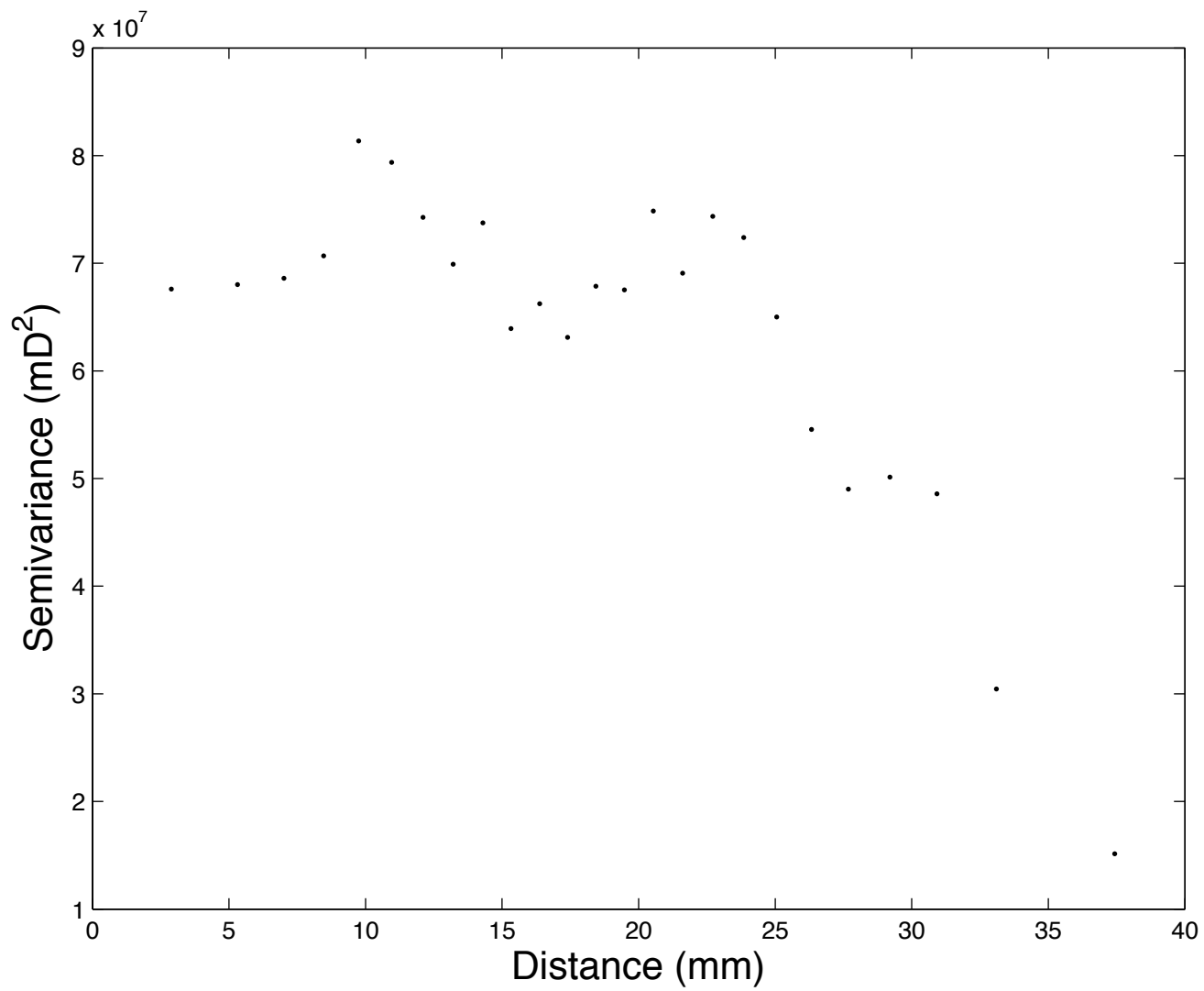


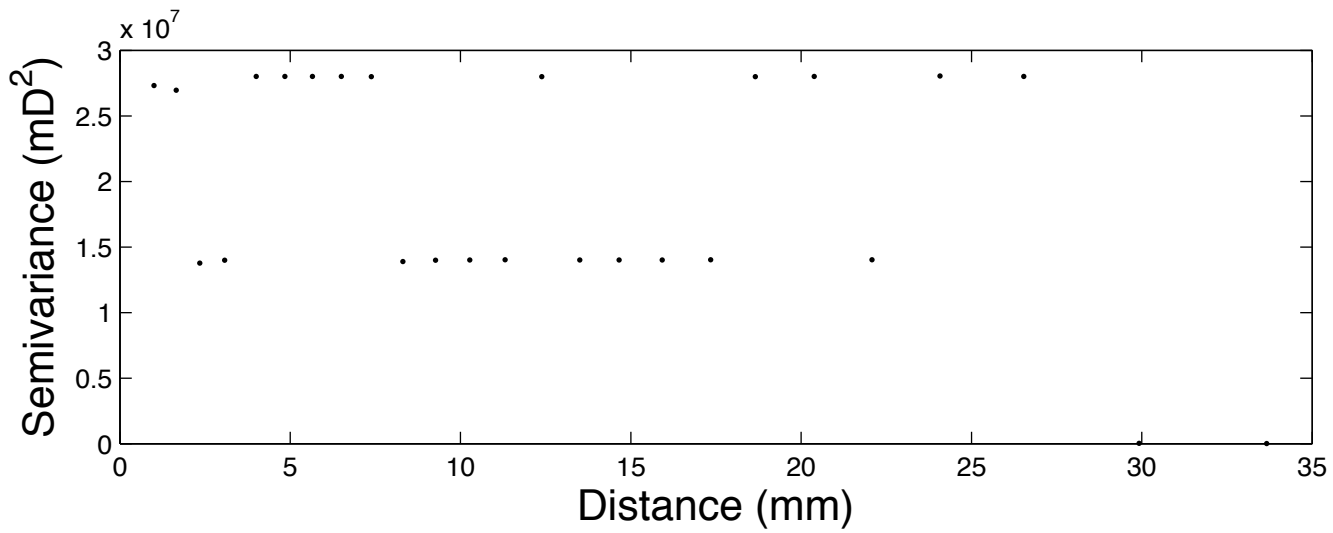
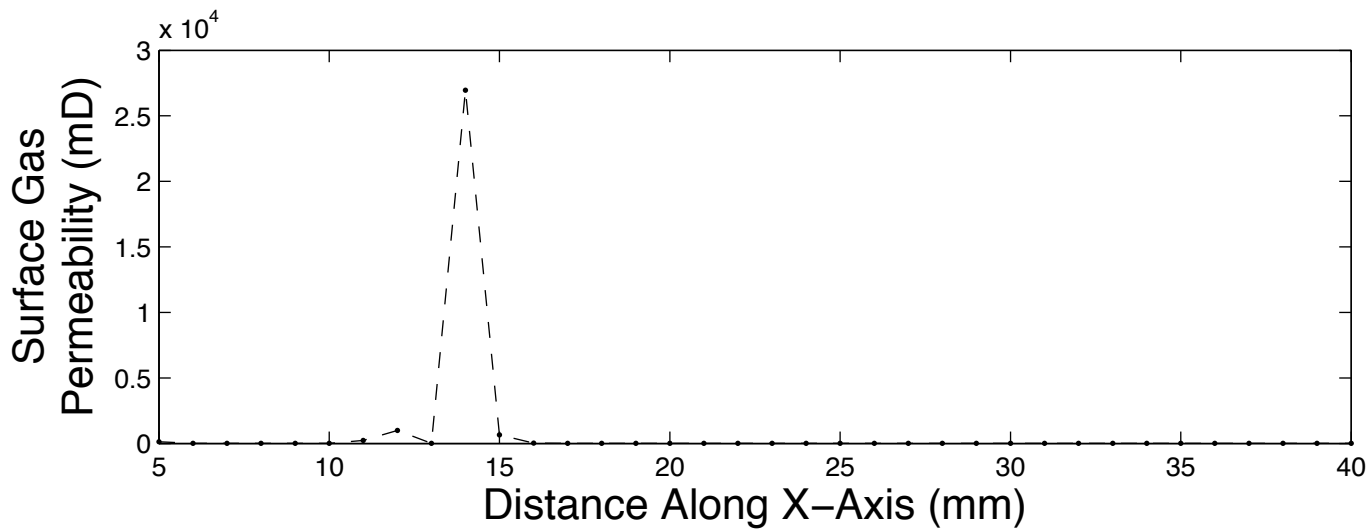


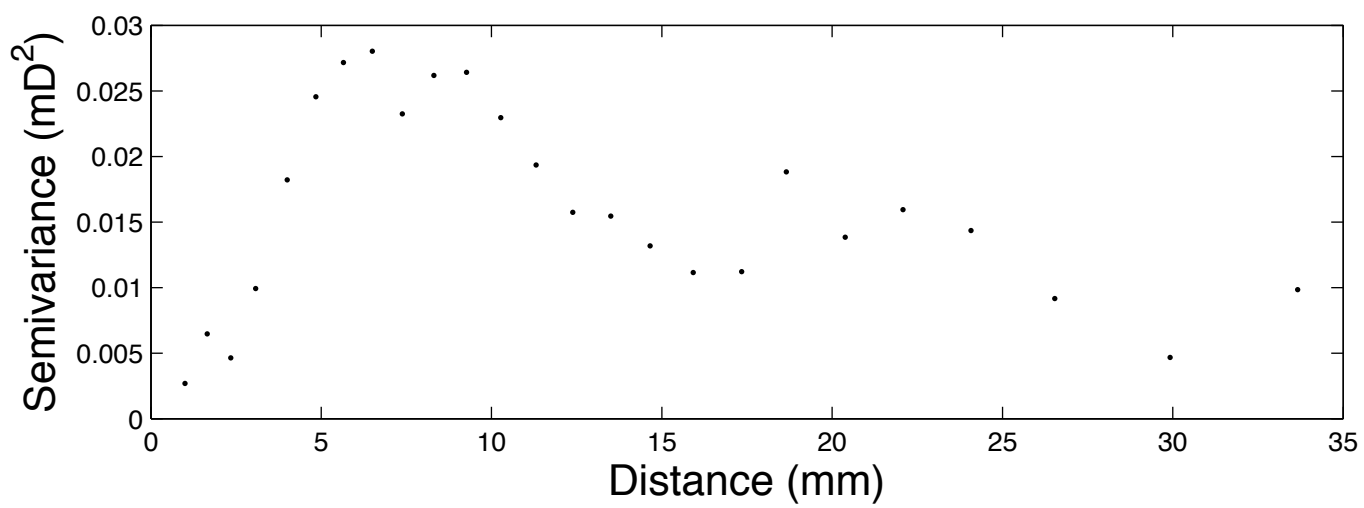
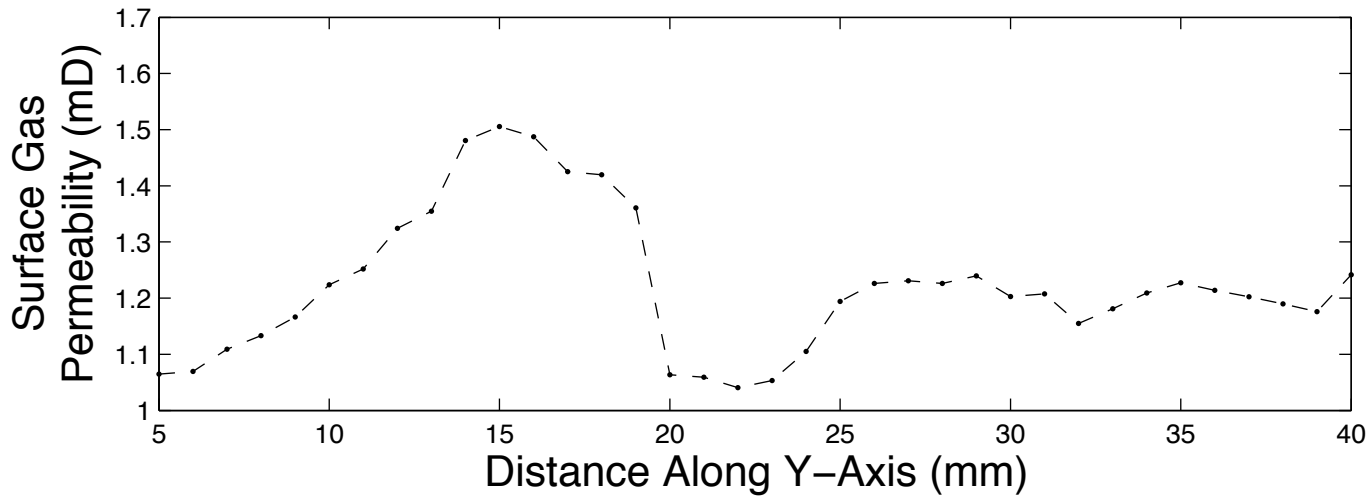


Concrete 5k PSI

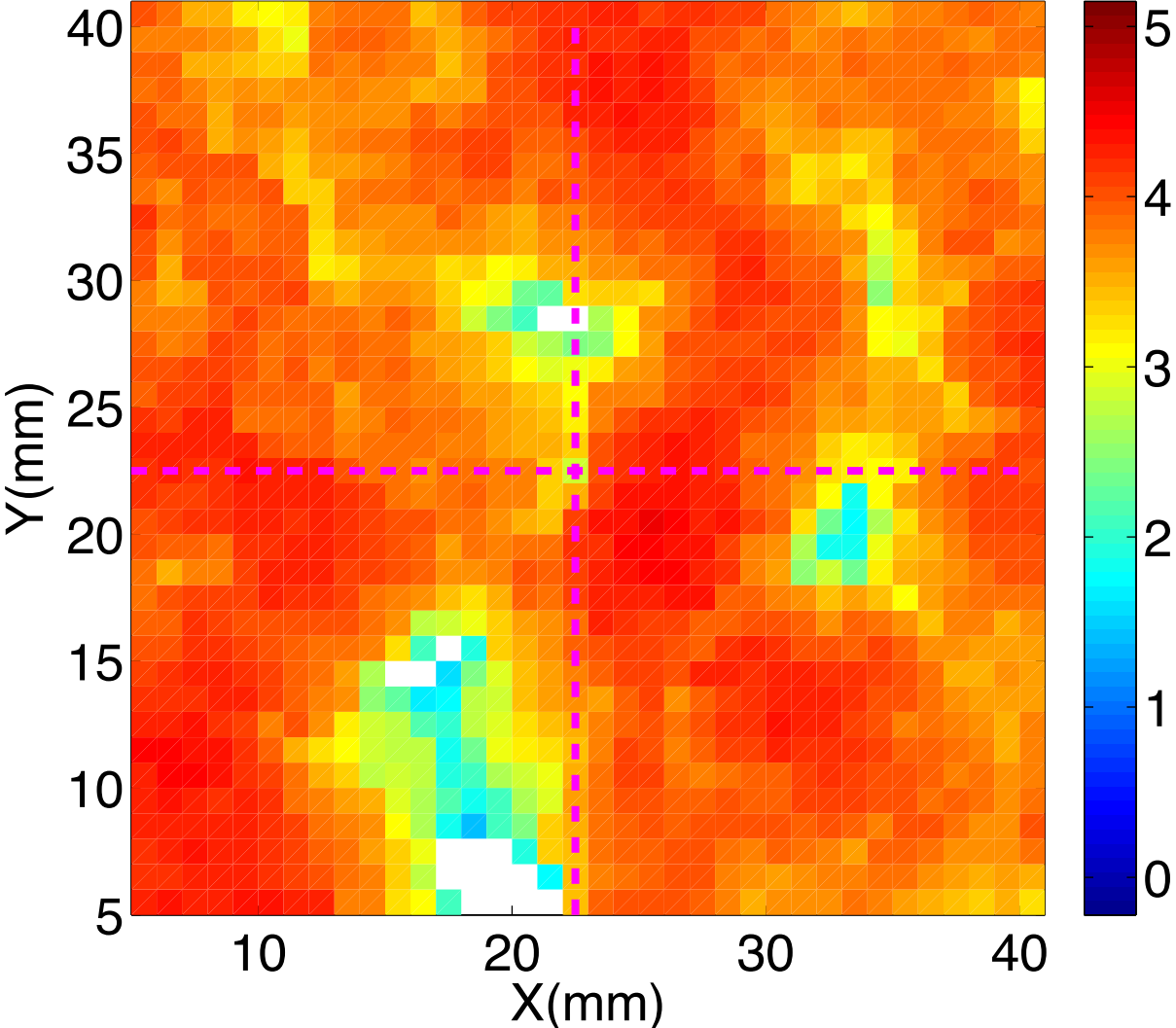


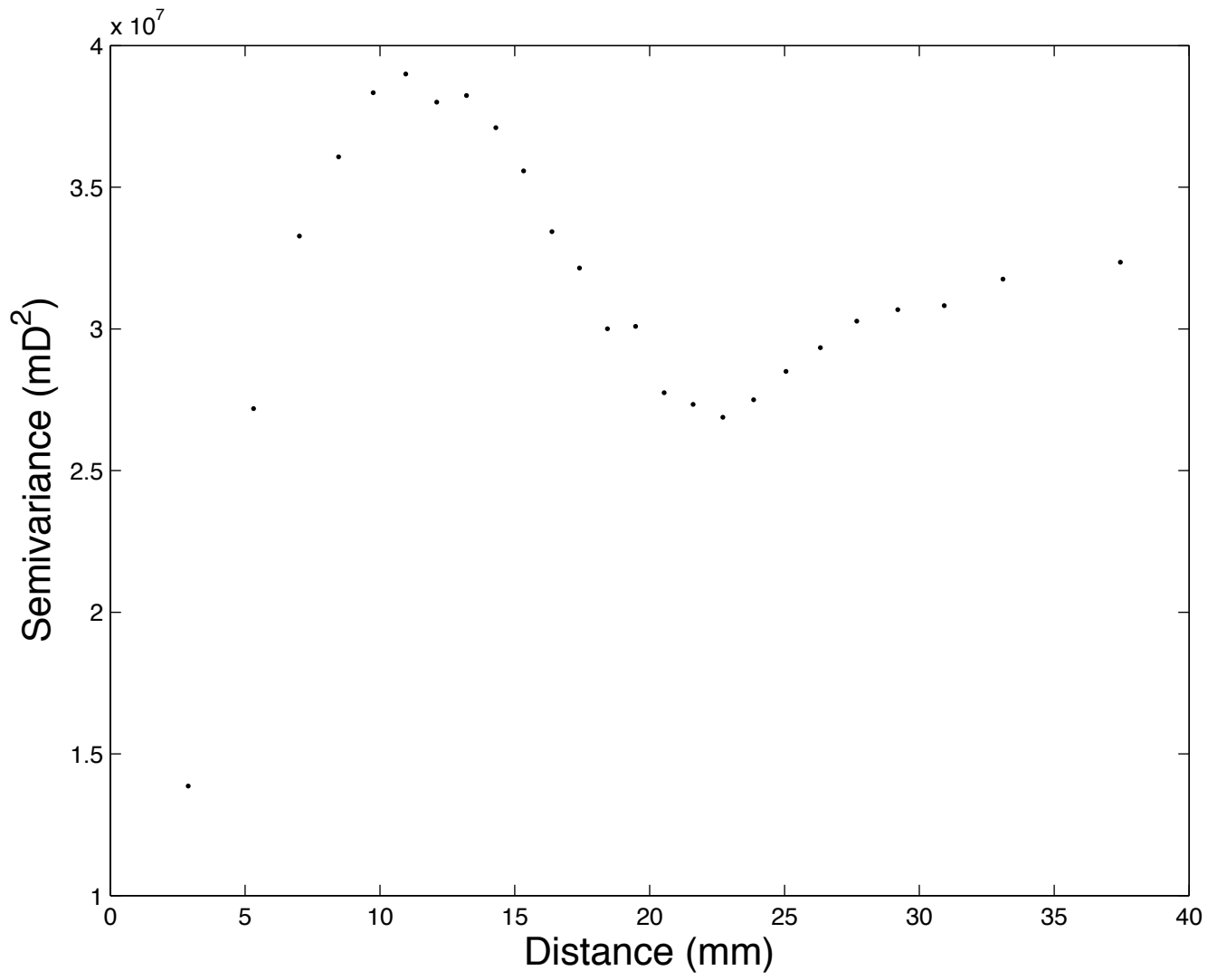


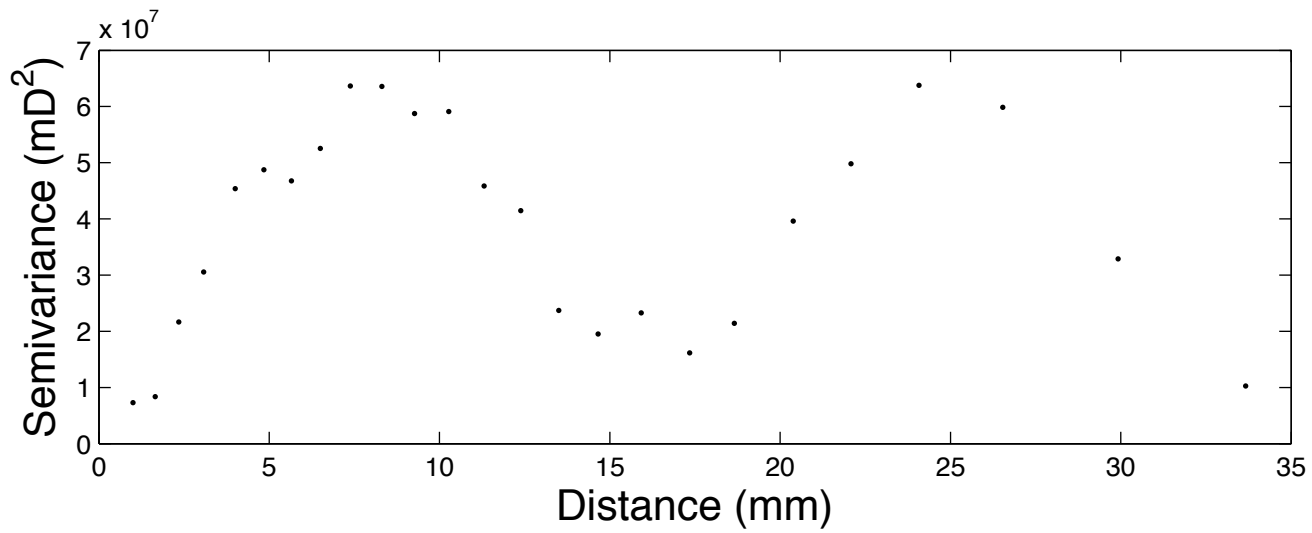
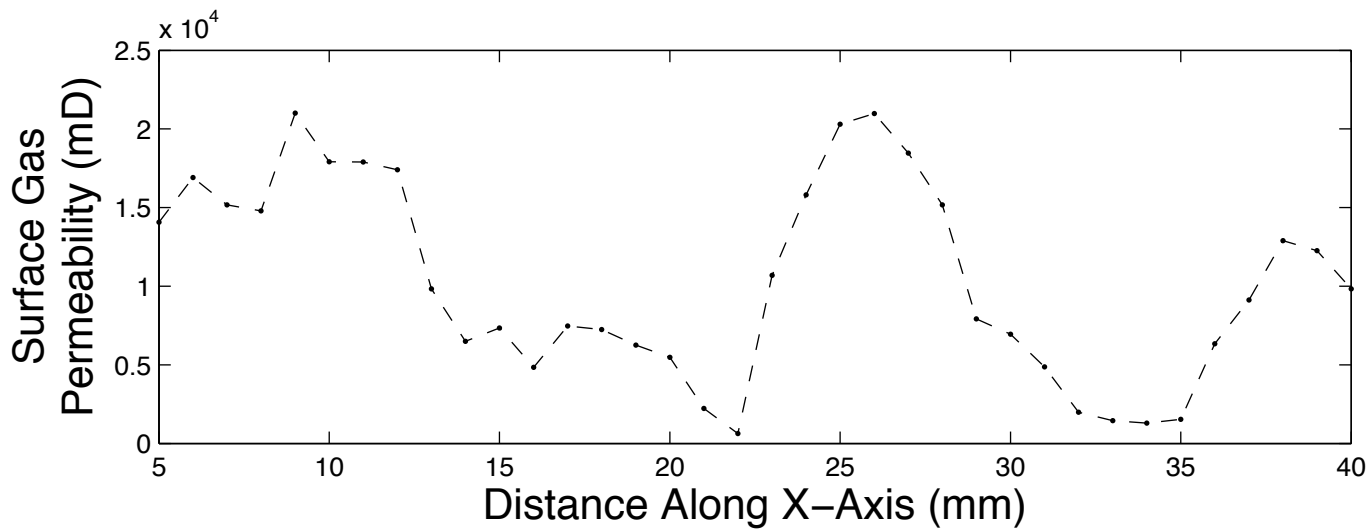


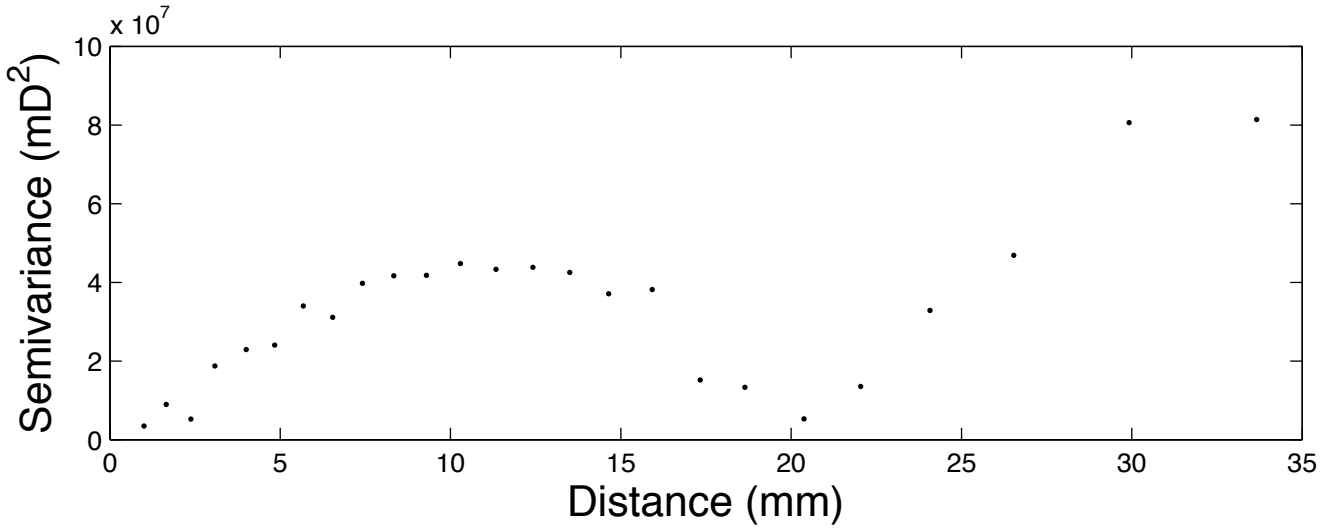
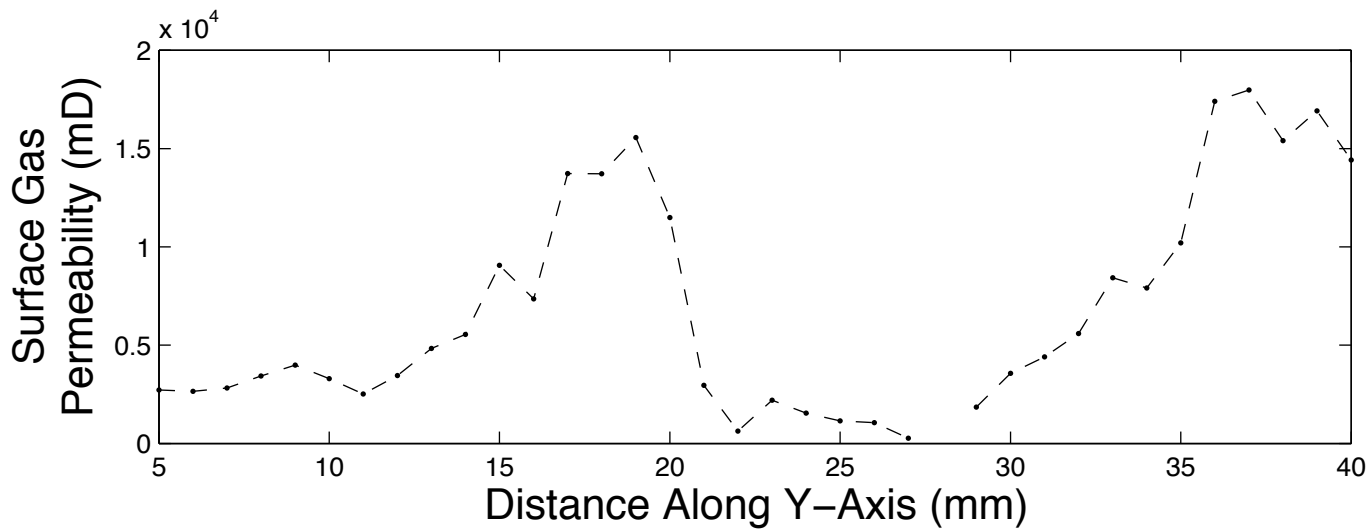


Concrete Paver 1

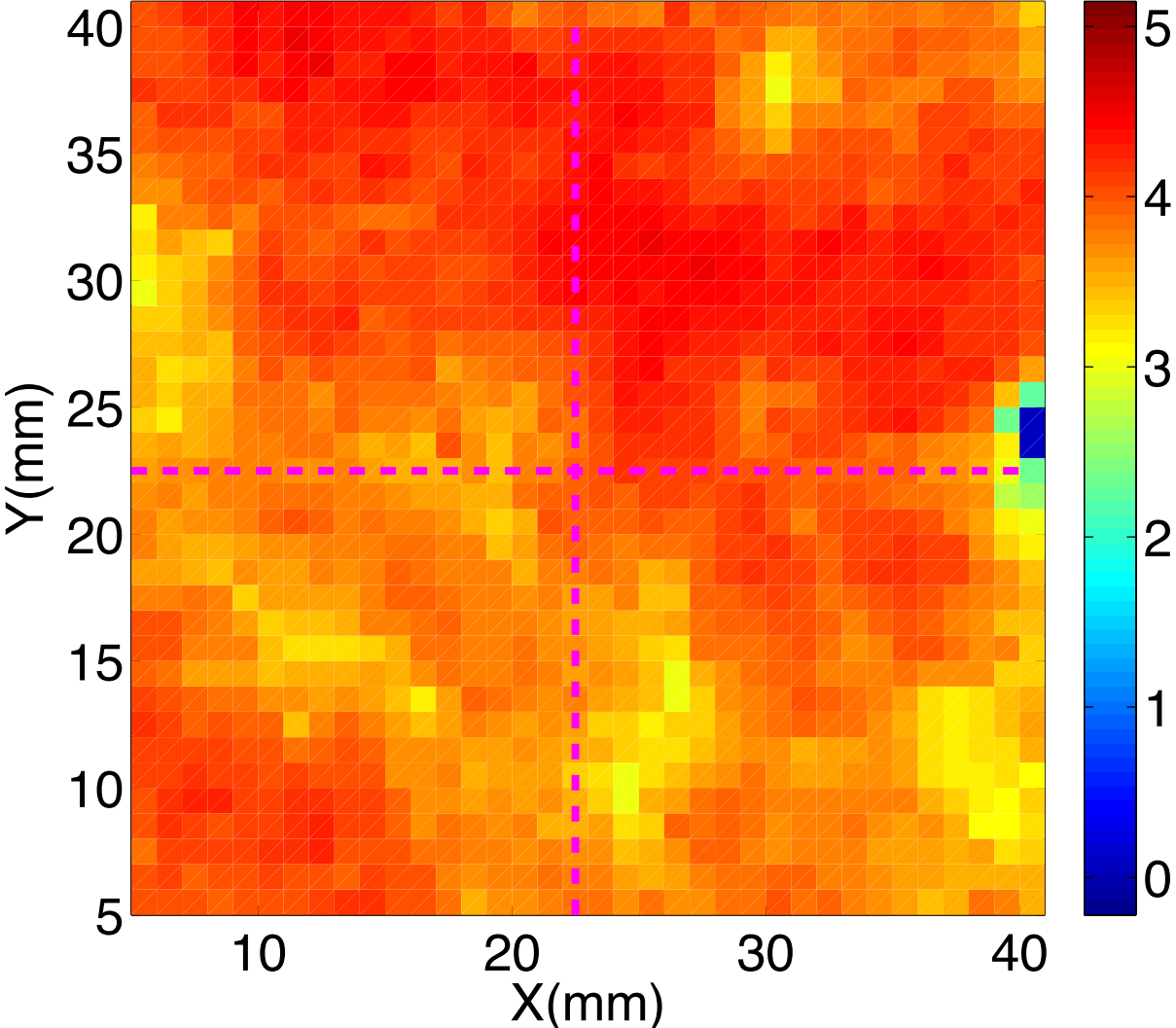


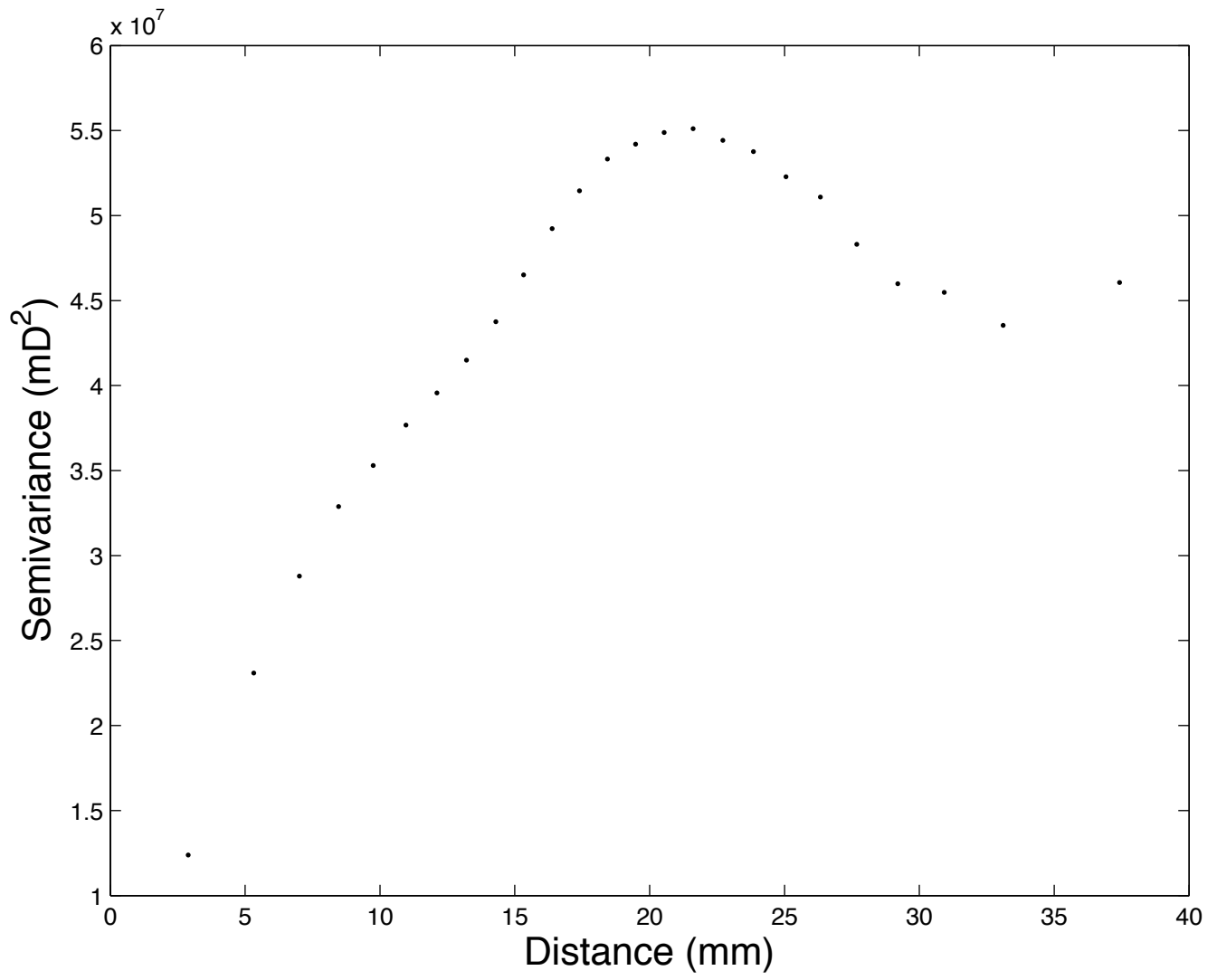


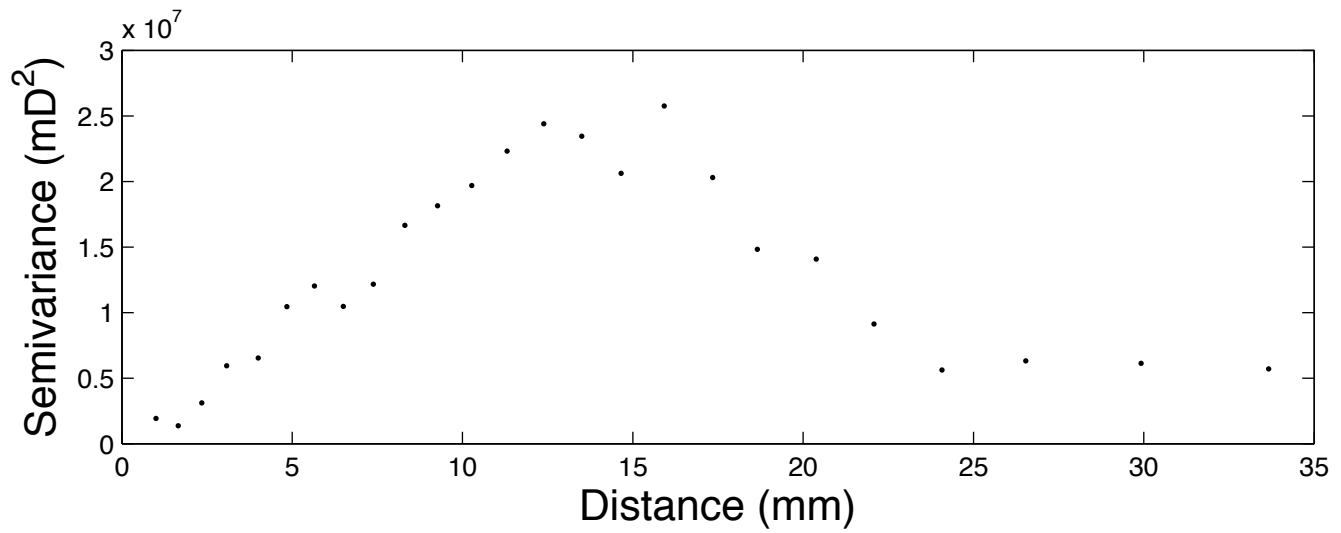
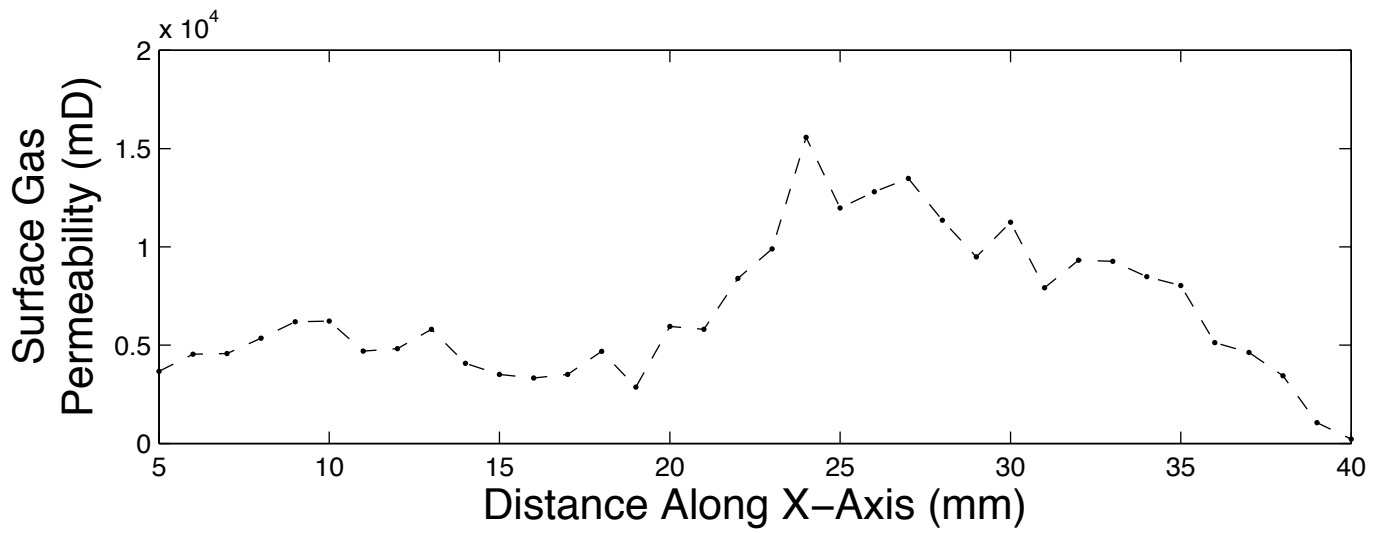


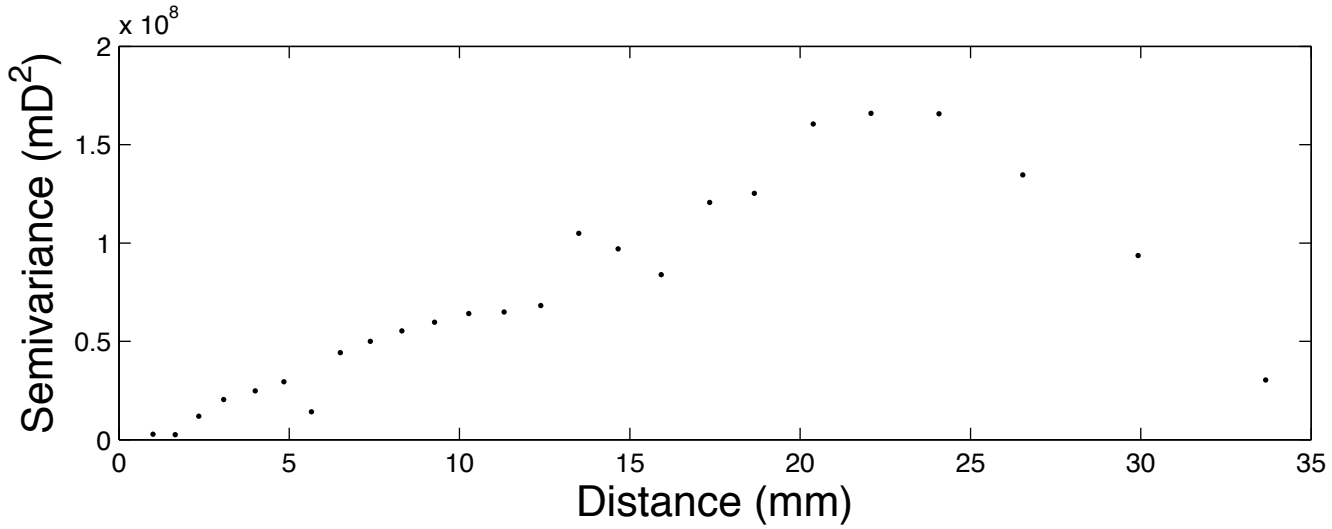
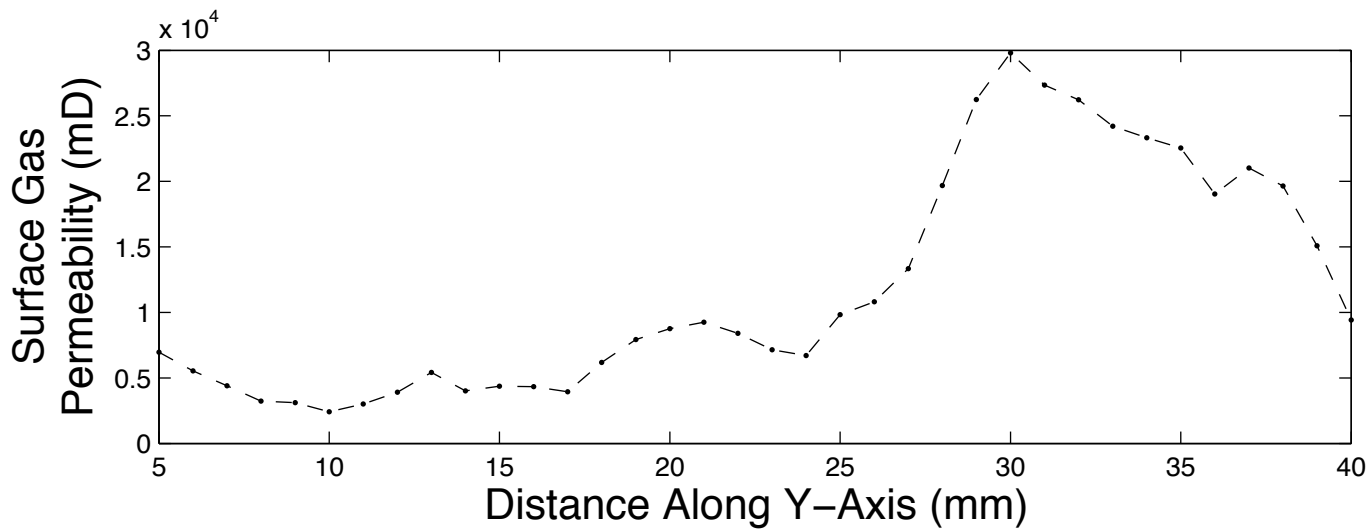


Concrete Paver 2

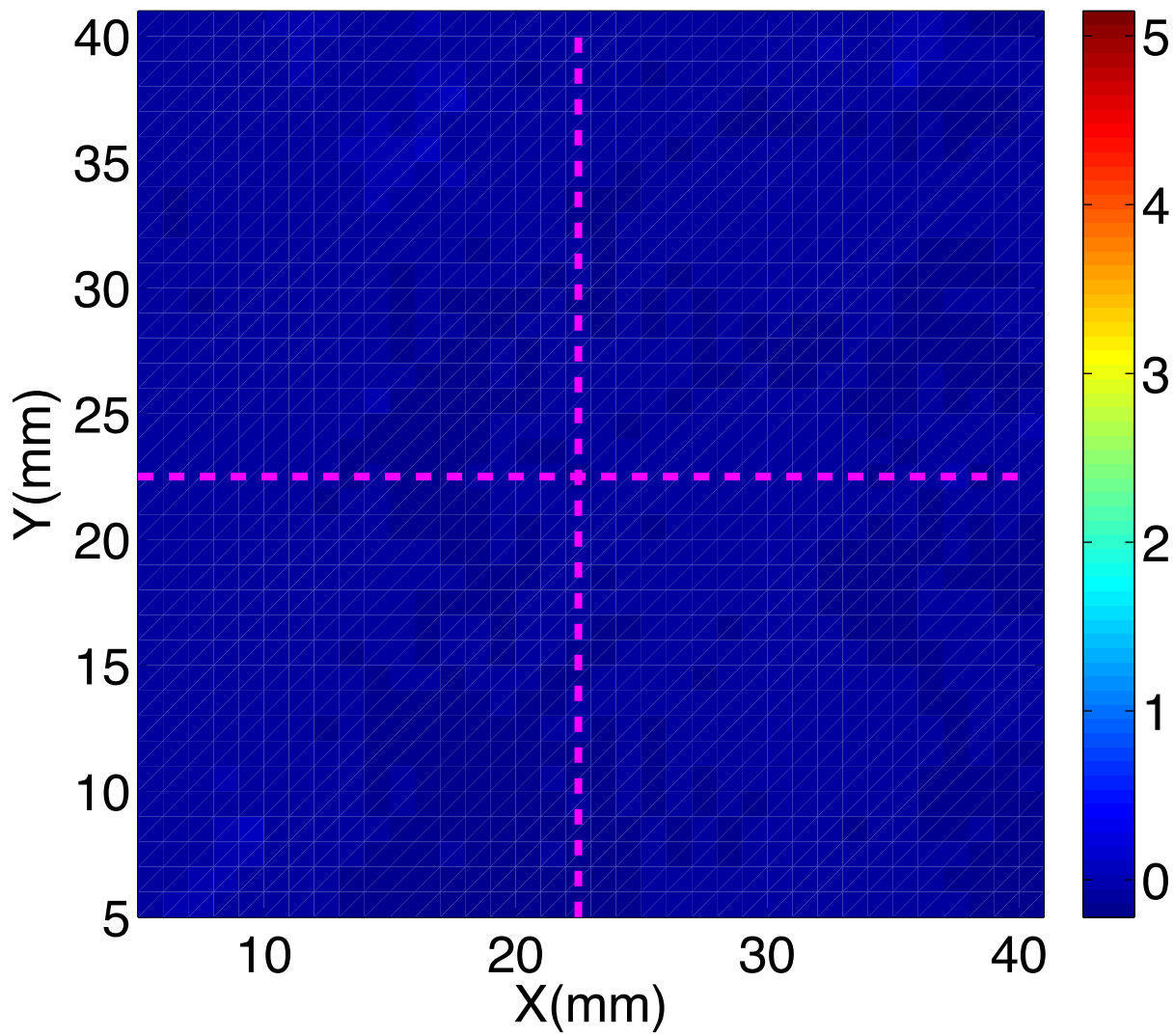


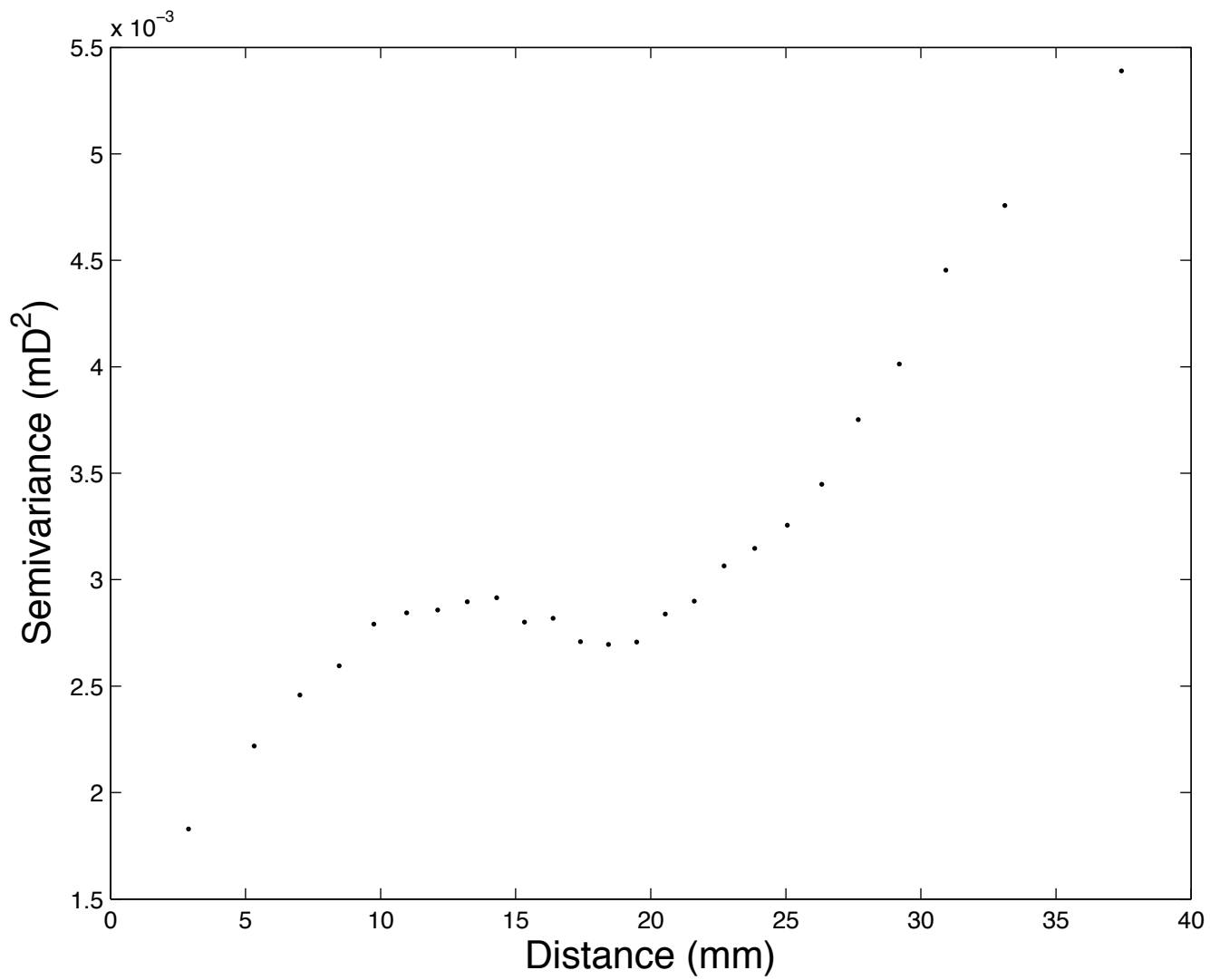


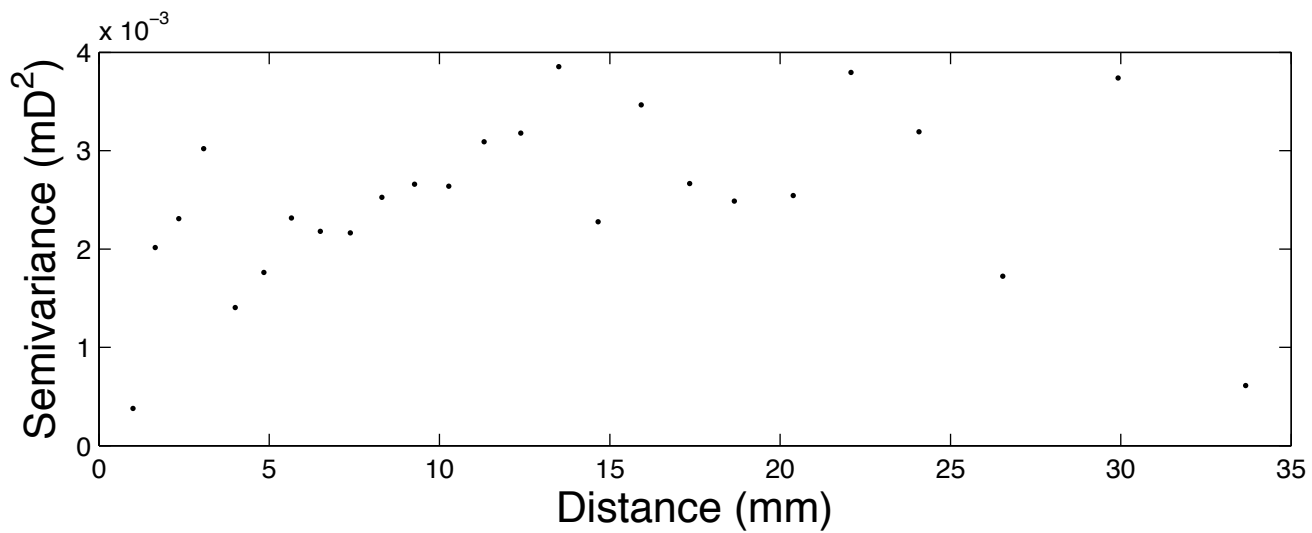
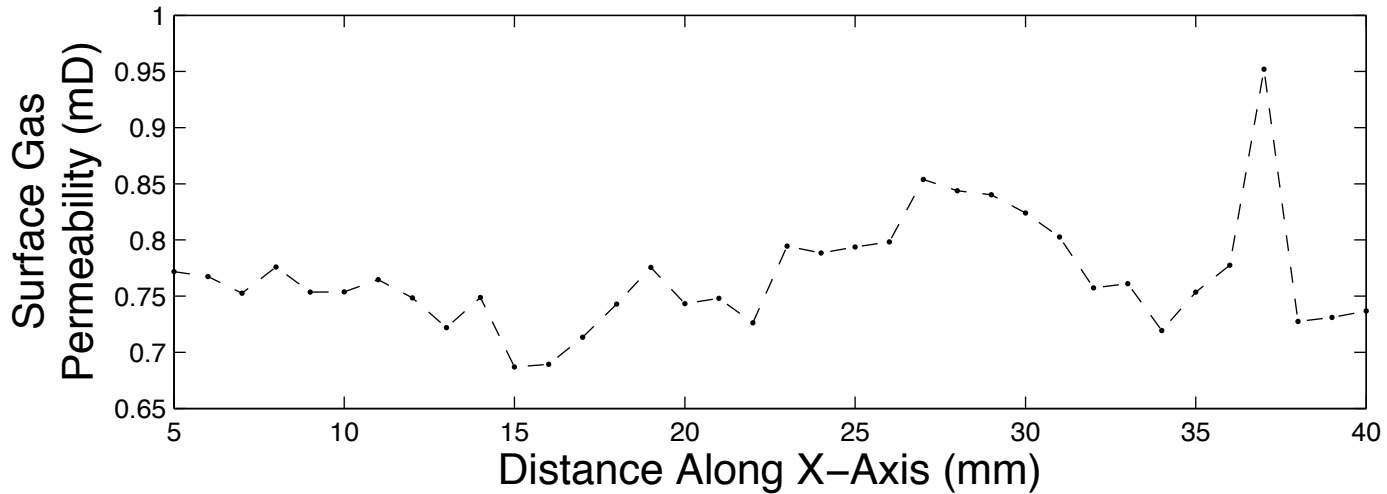


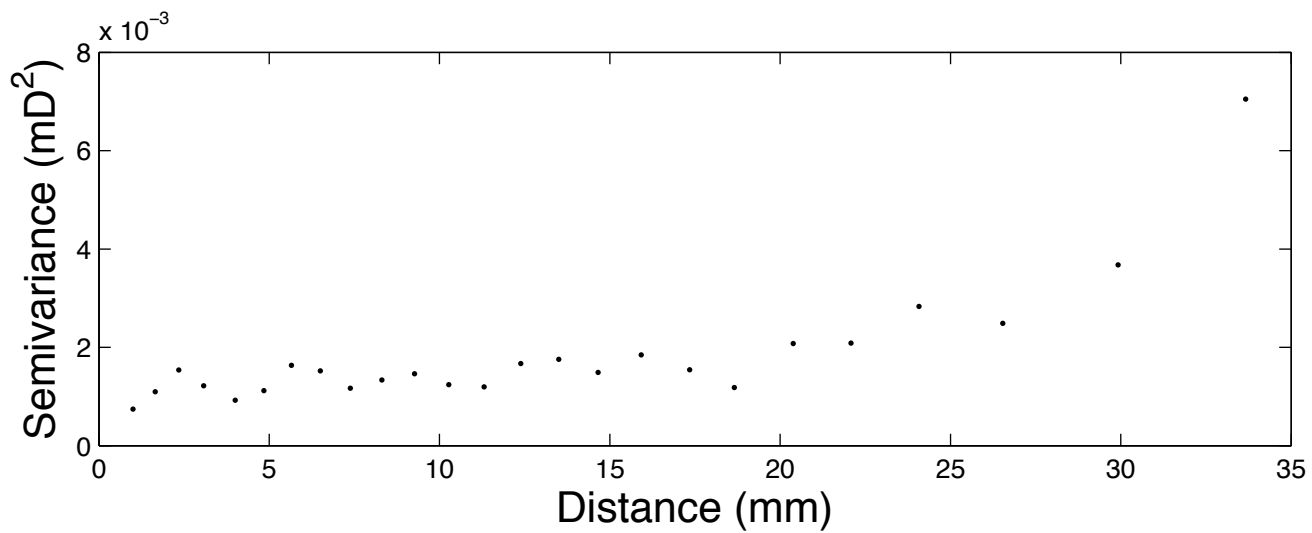
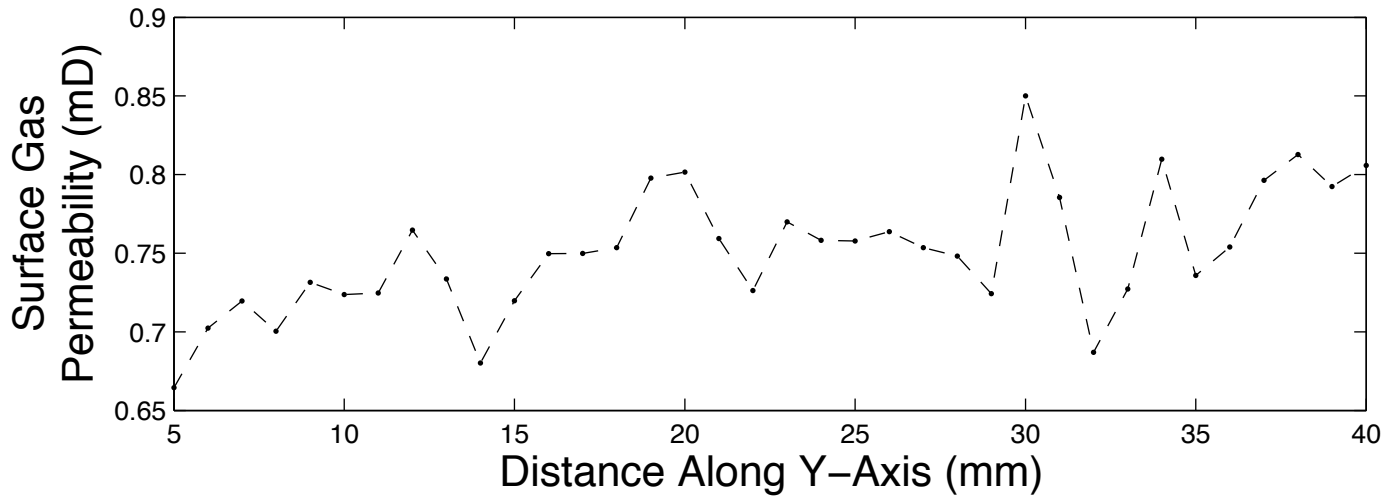


Granite

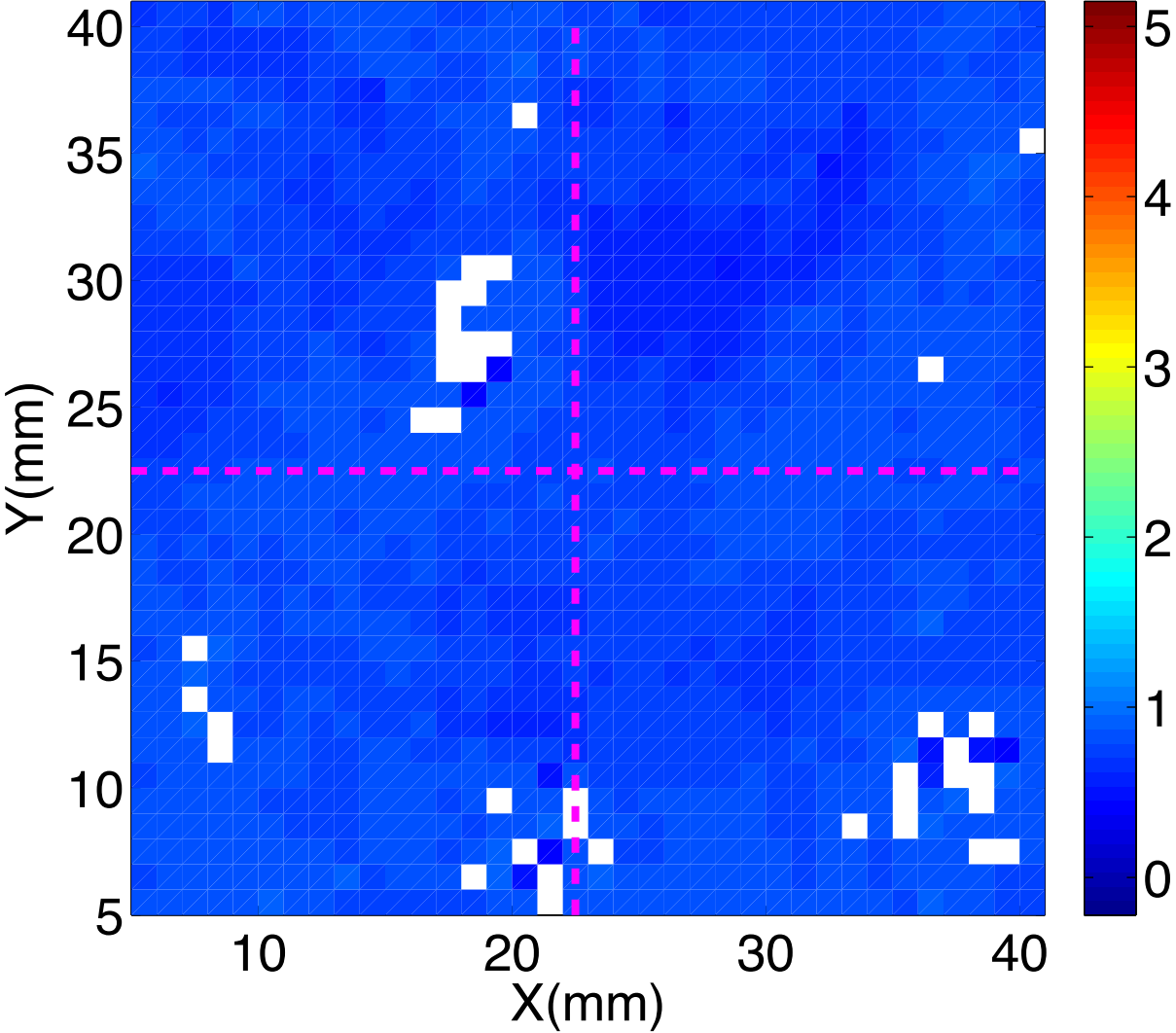


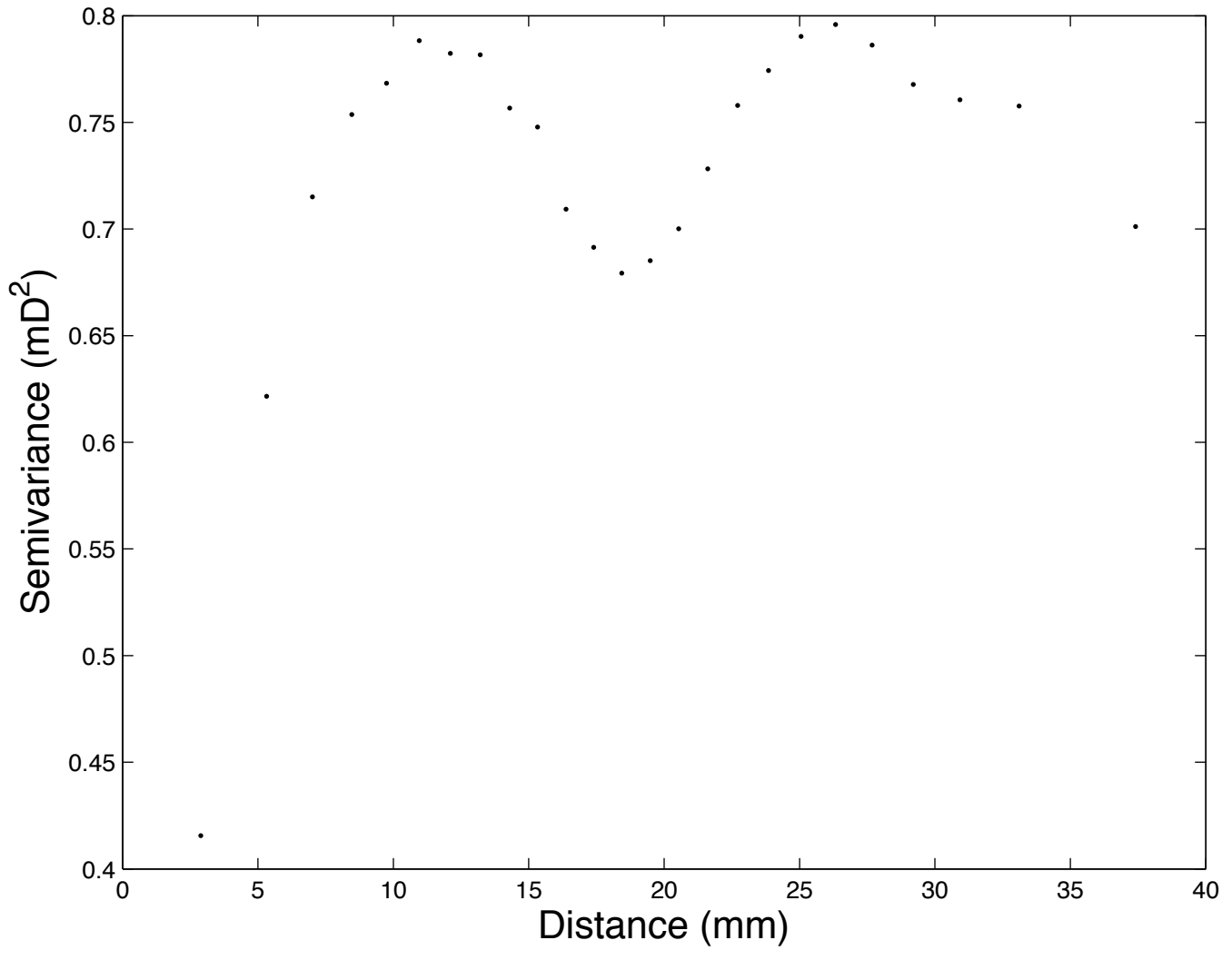


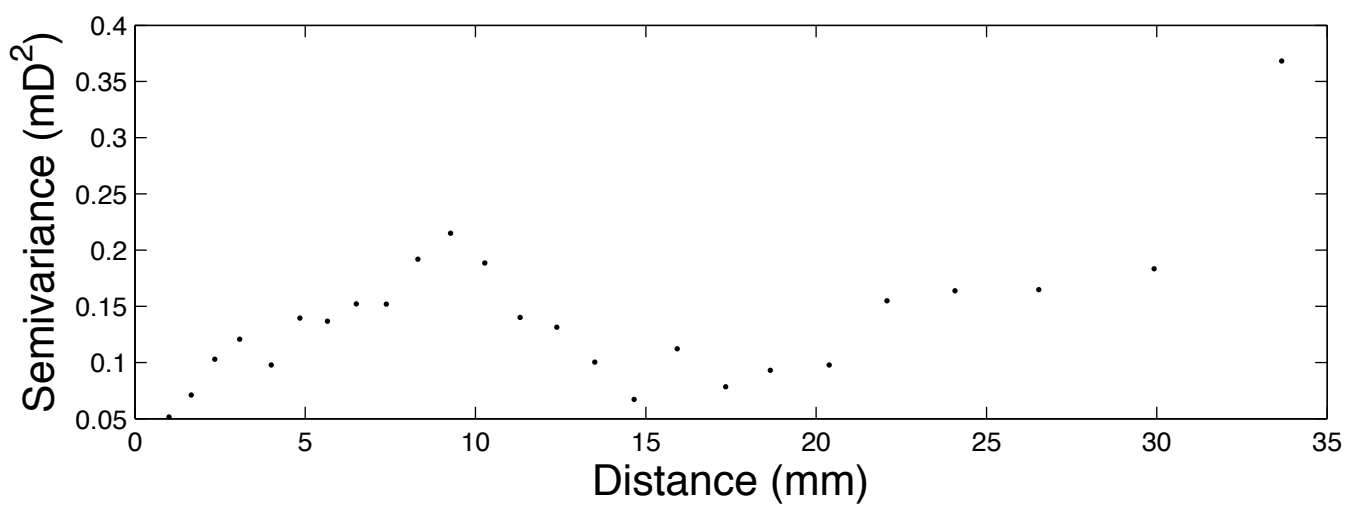
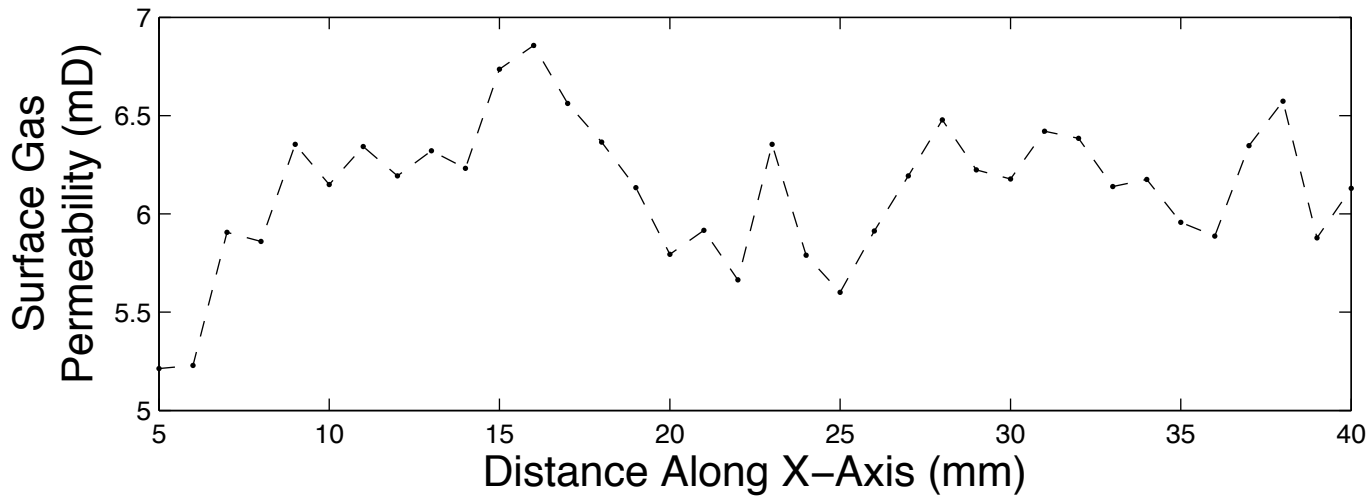


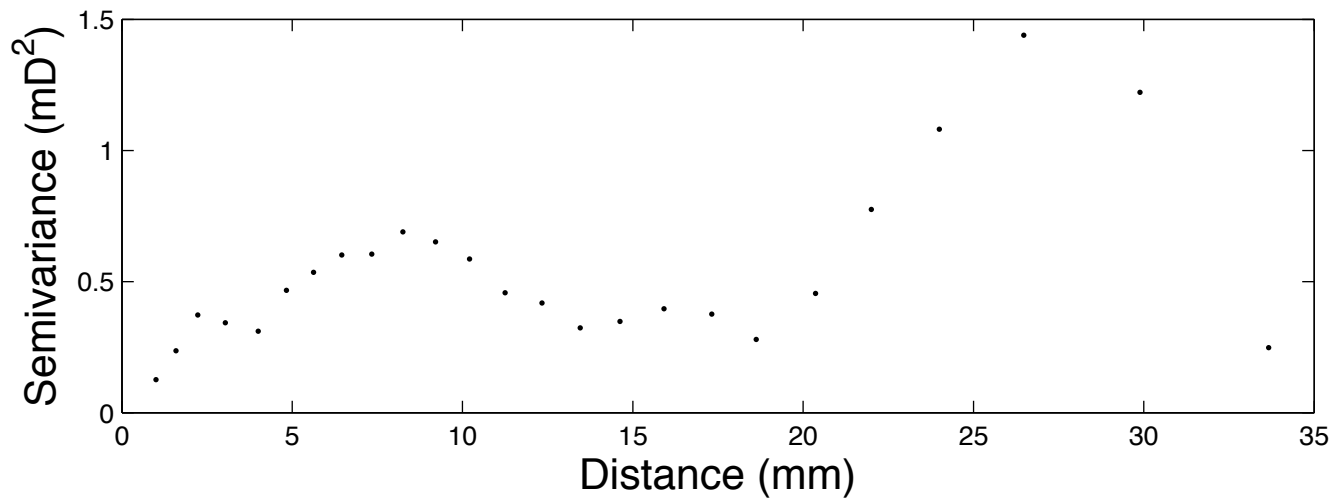
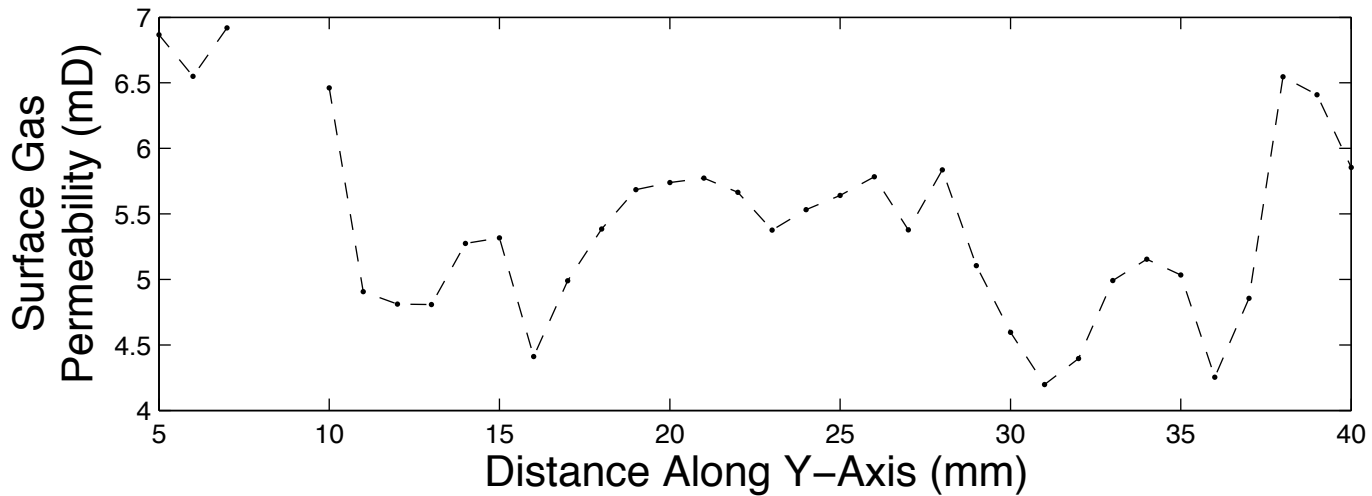


Gray Indiana Limestone 1

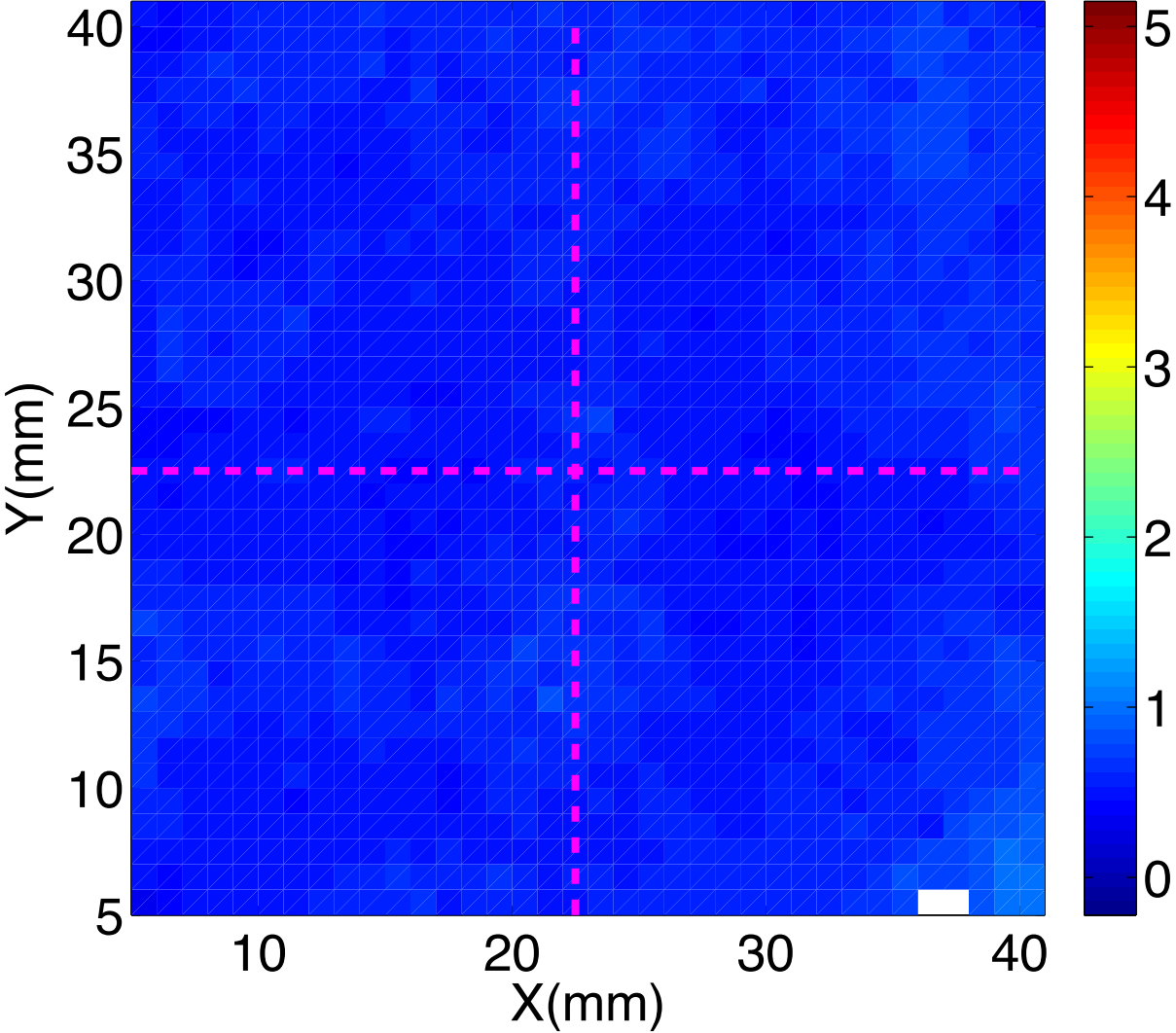


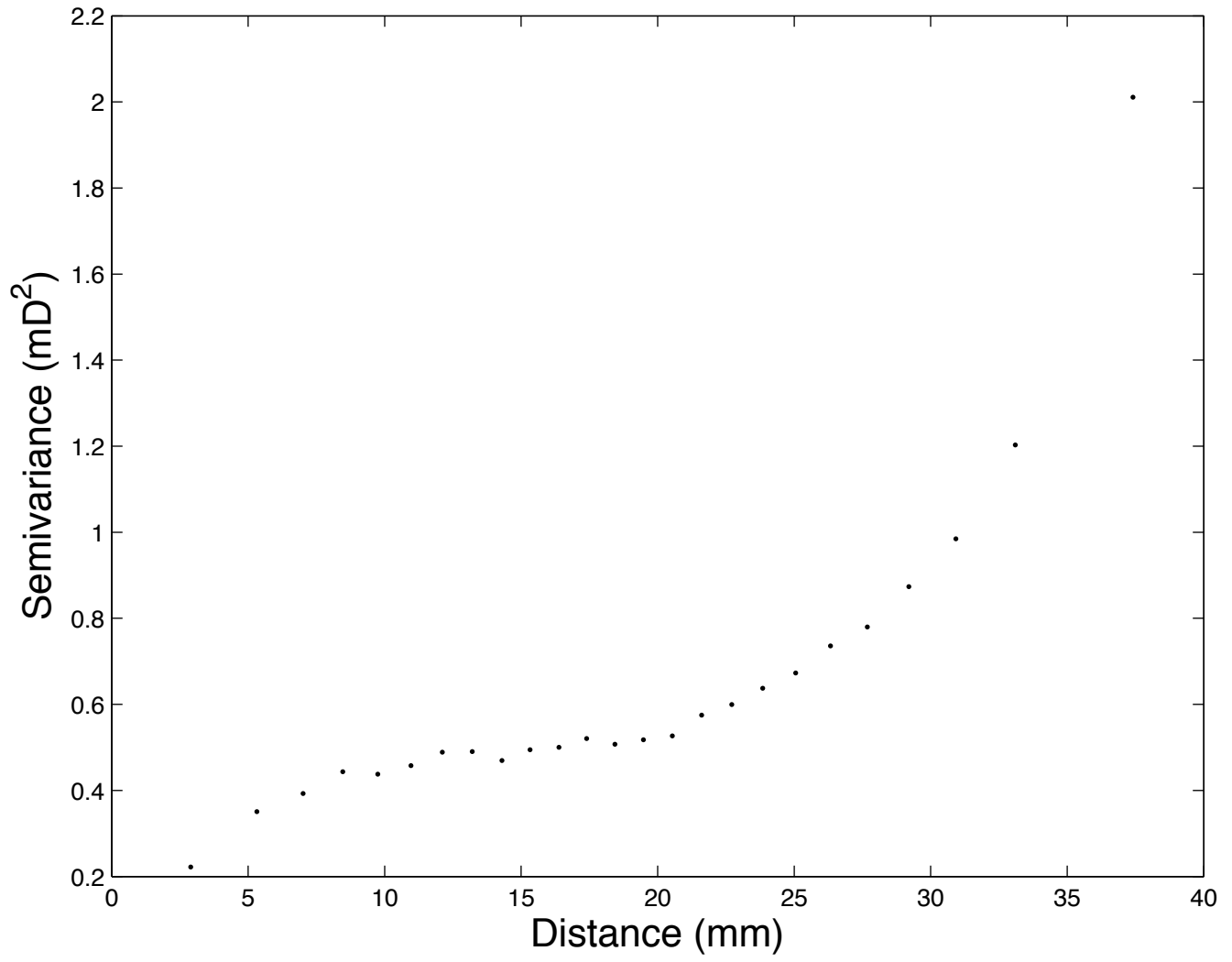


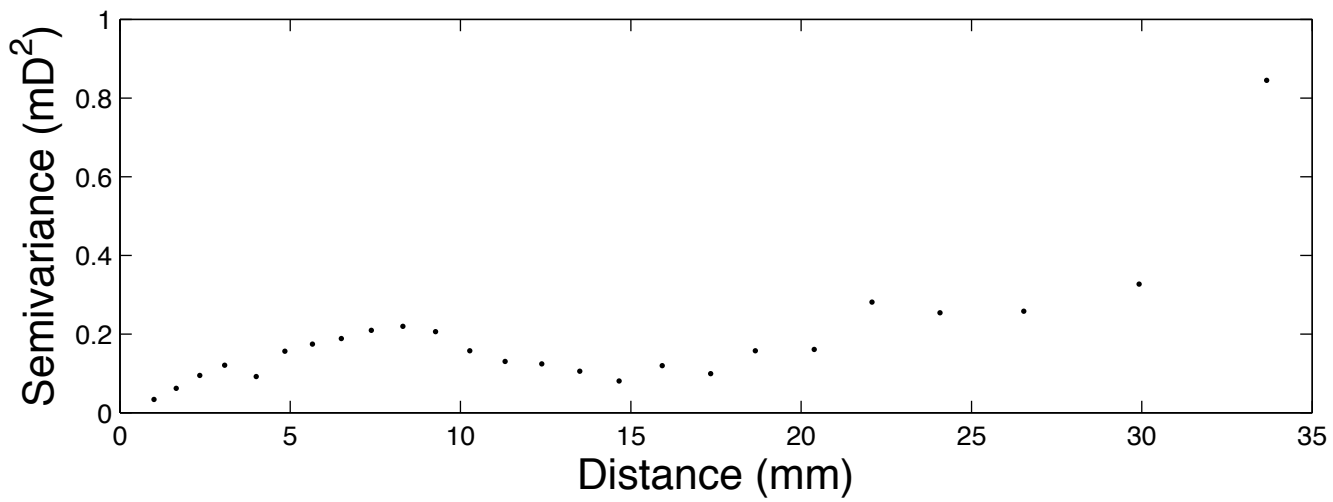
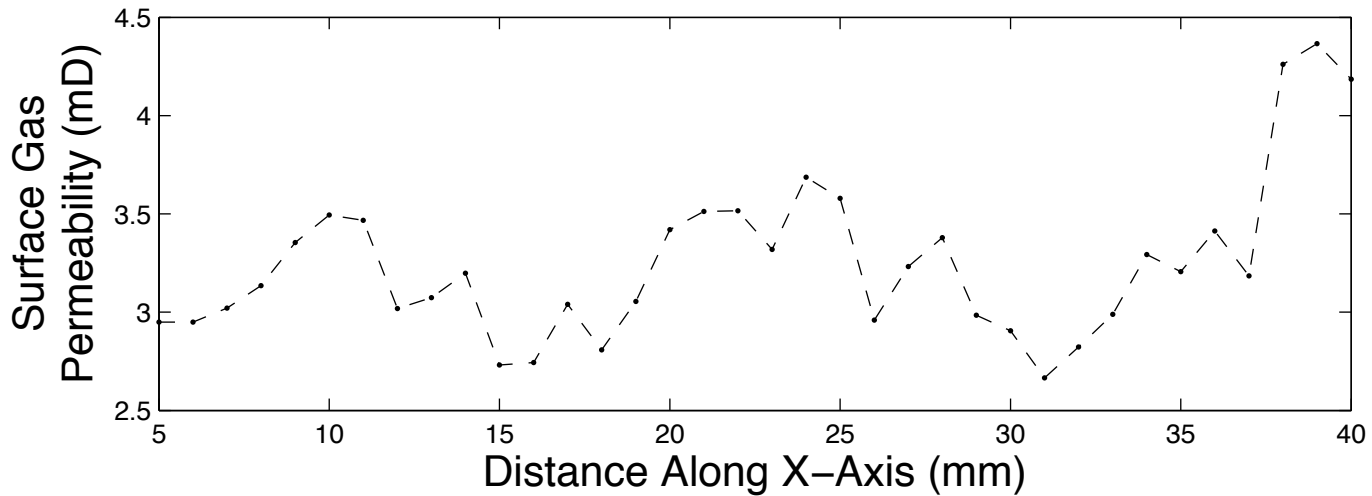


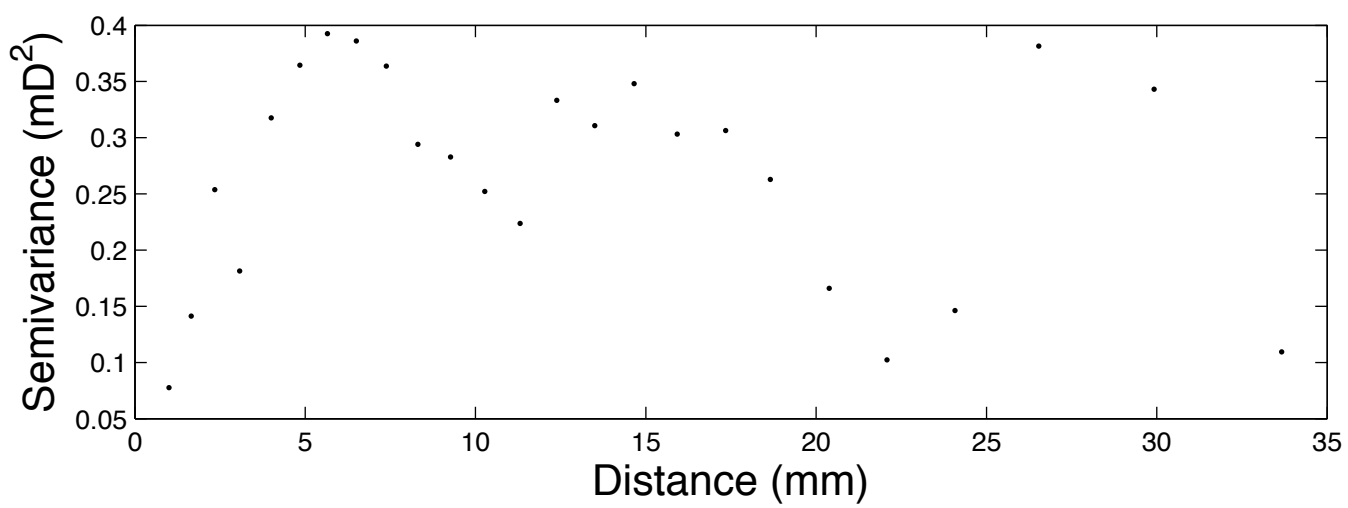
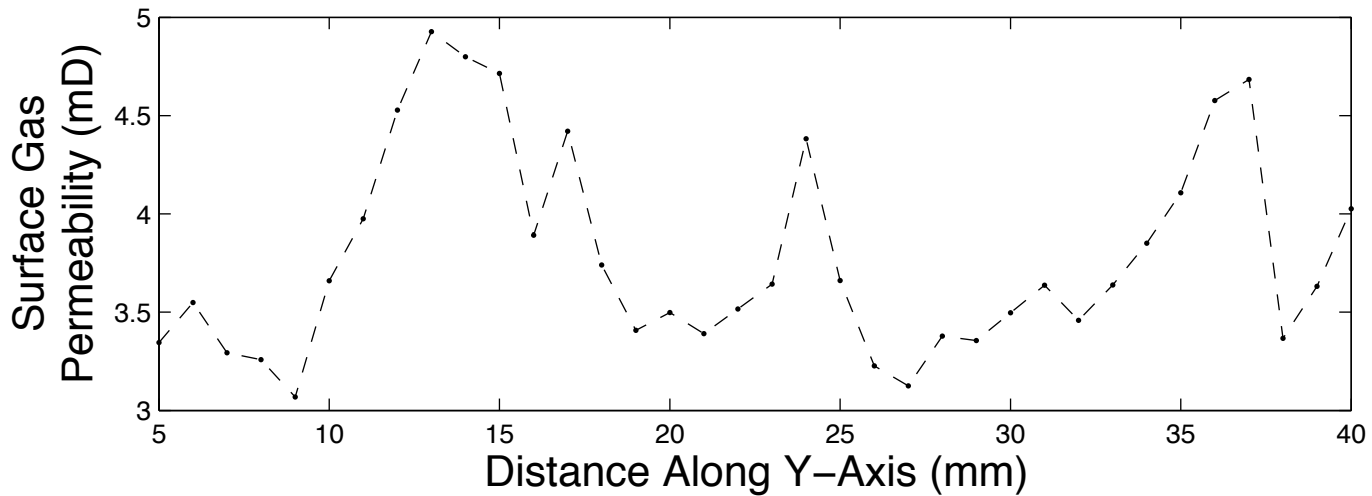


Gray Indiana Limestone 2

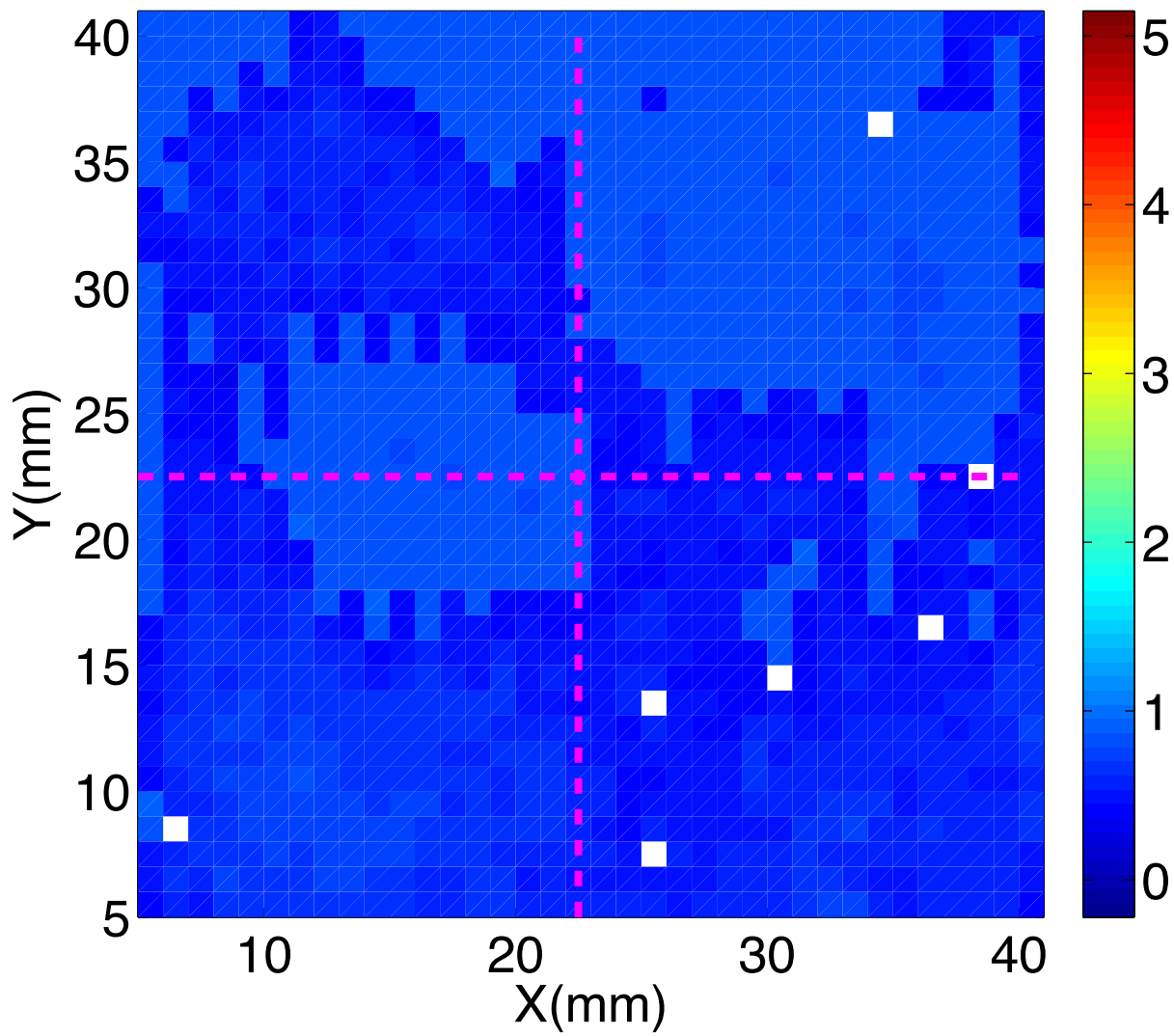


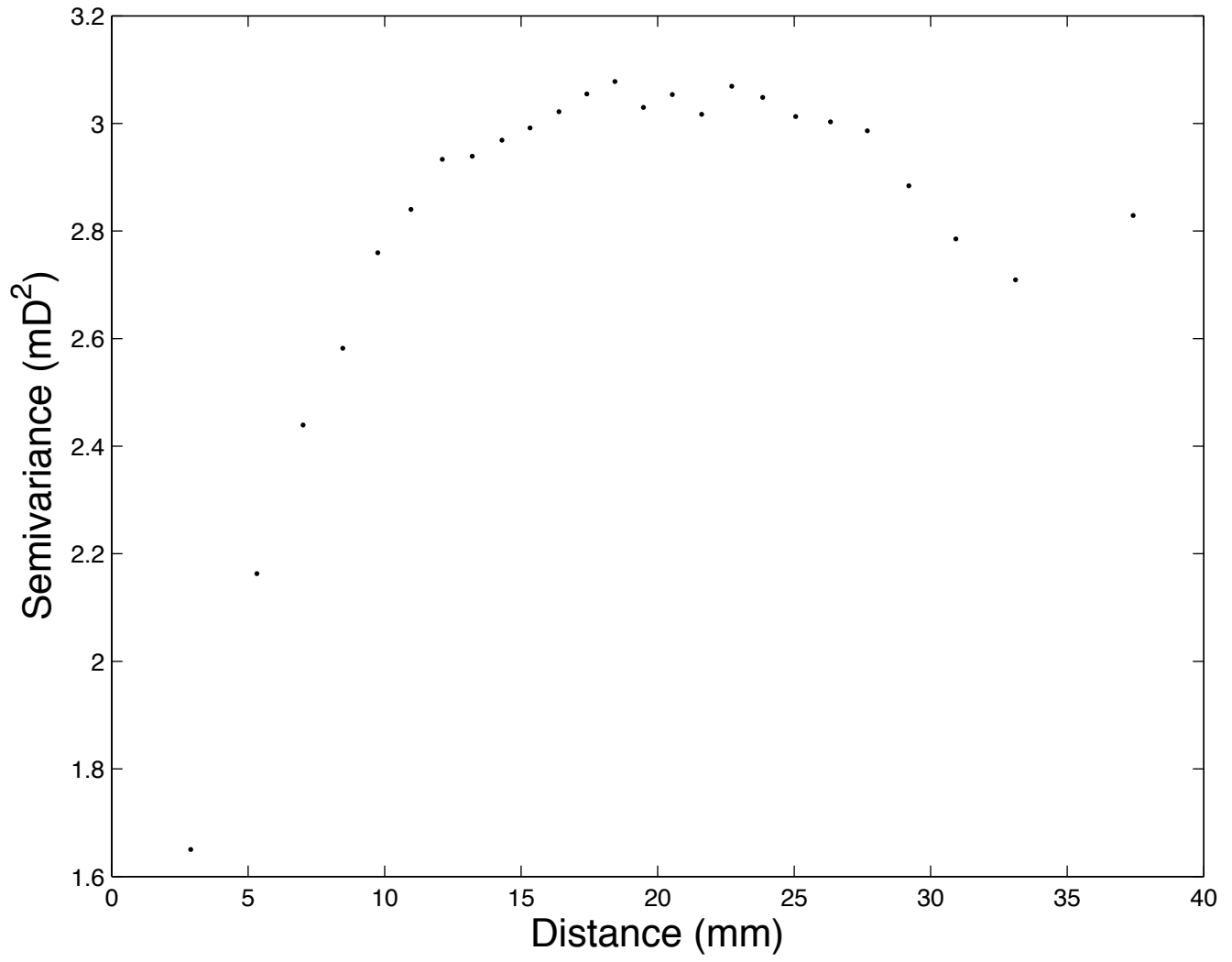


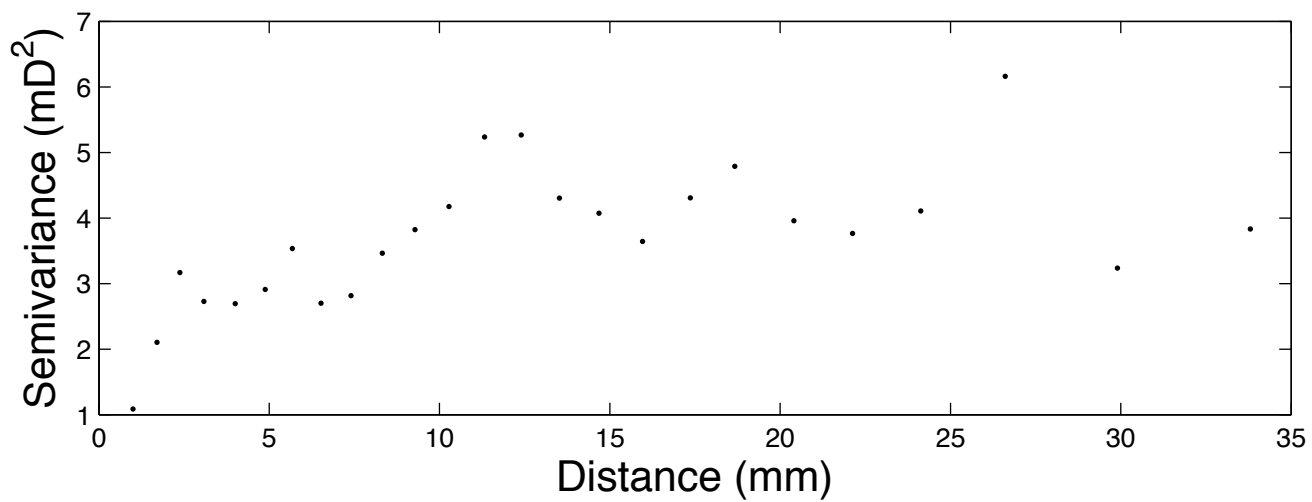
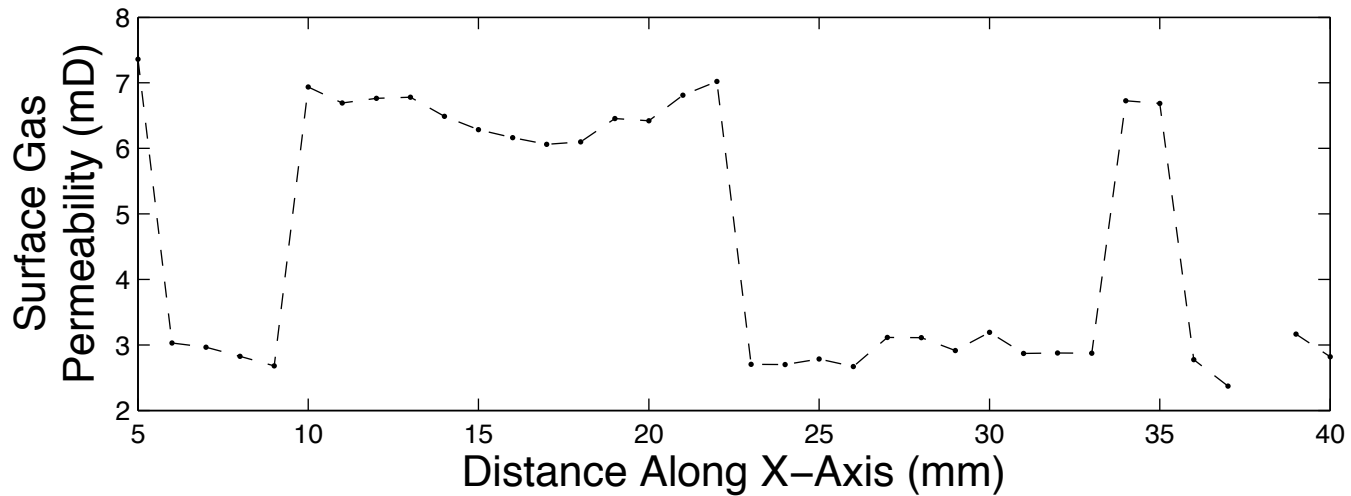


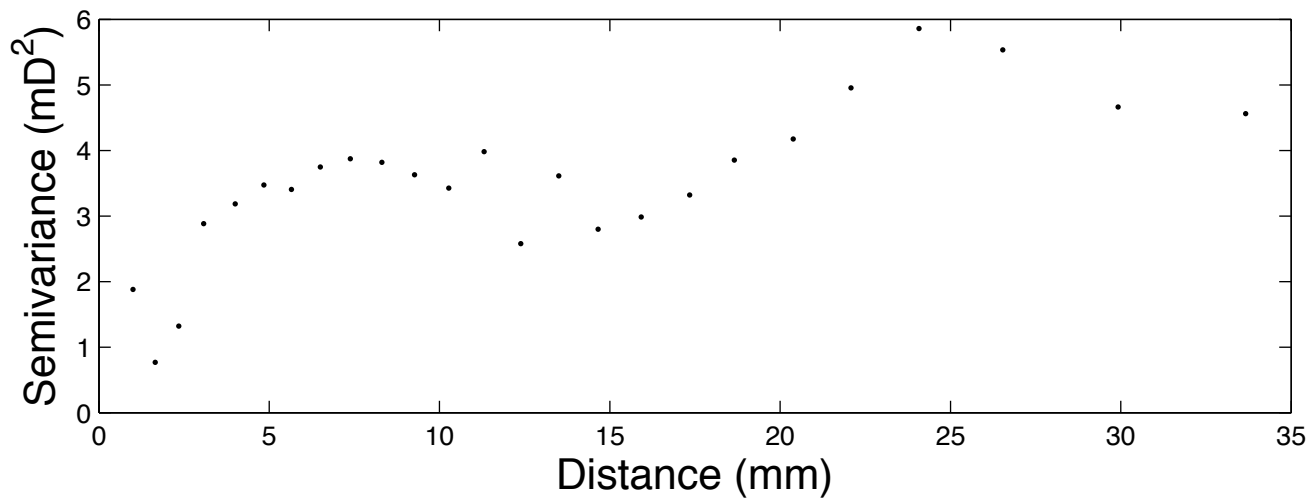
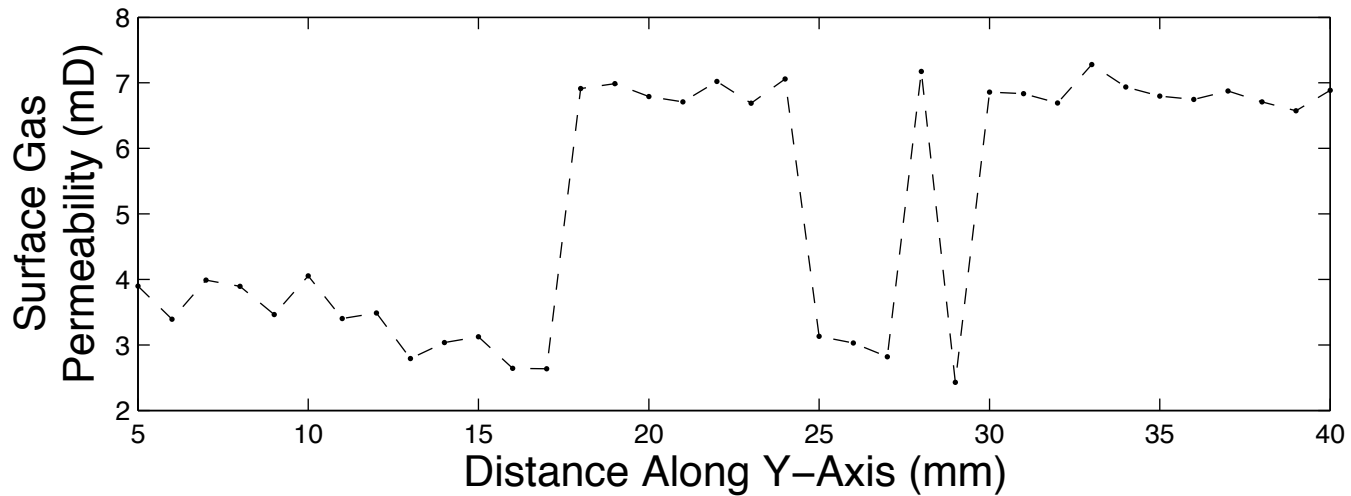


Ohio Sandstone

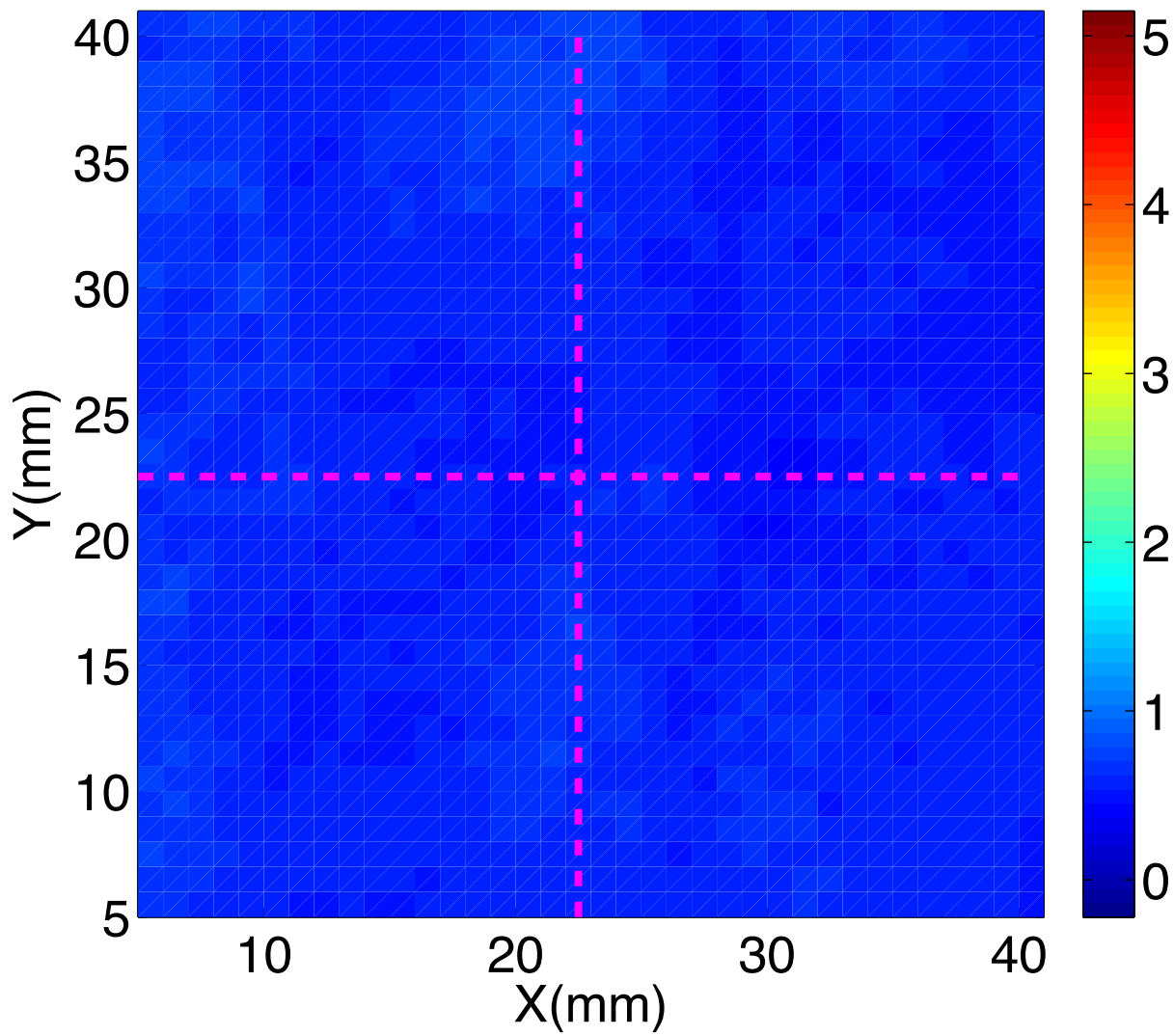


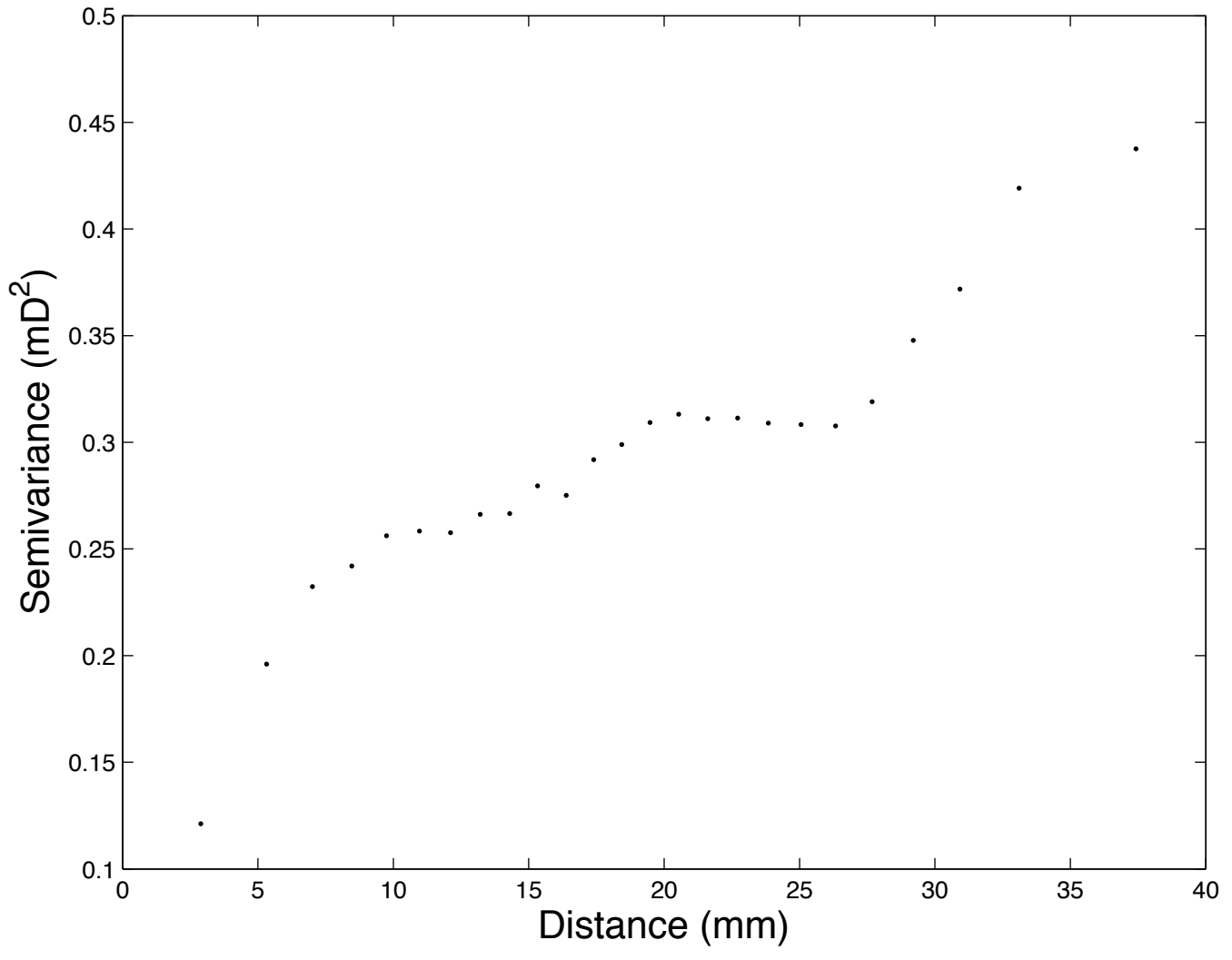


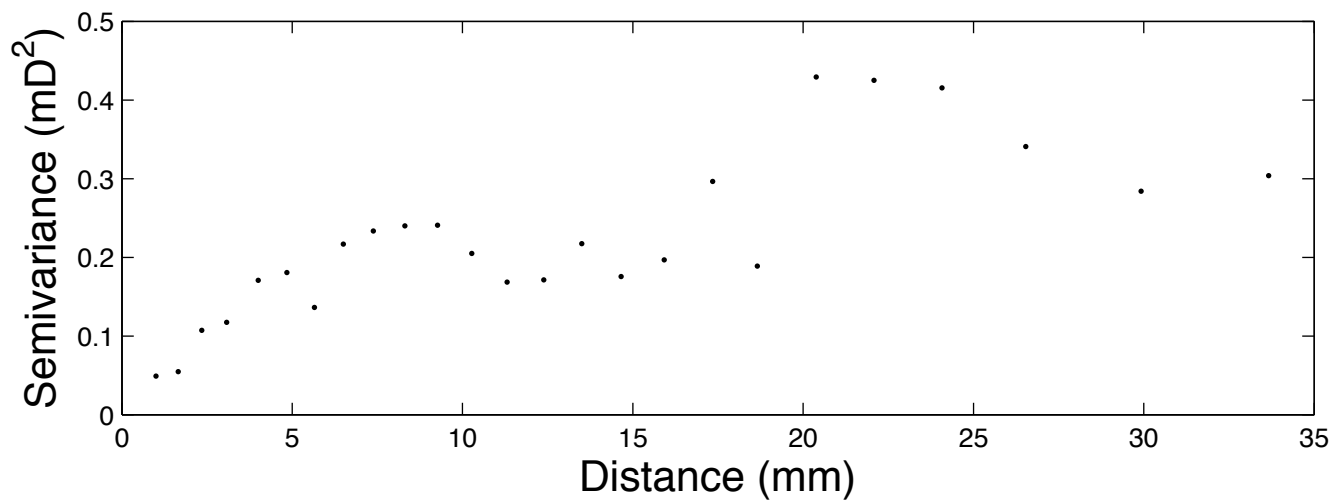
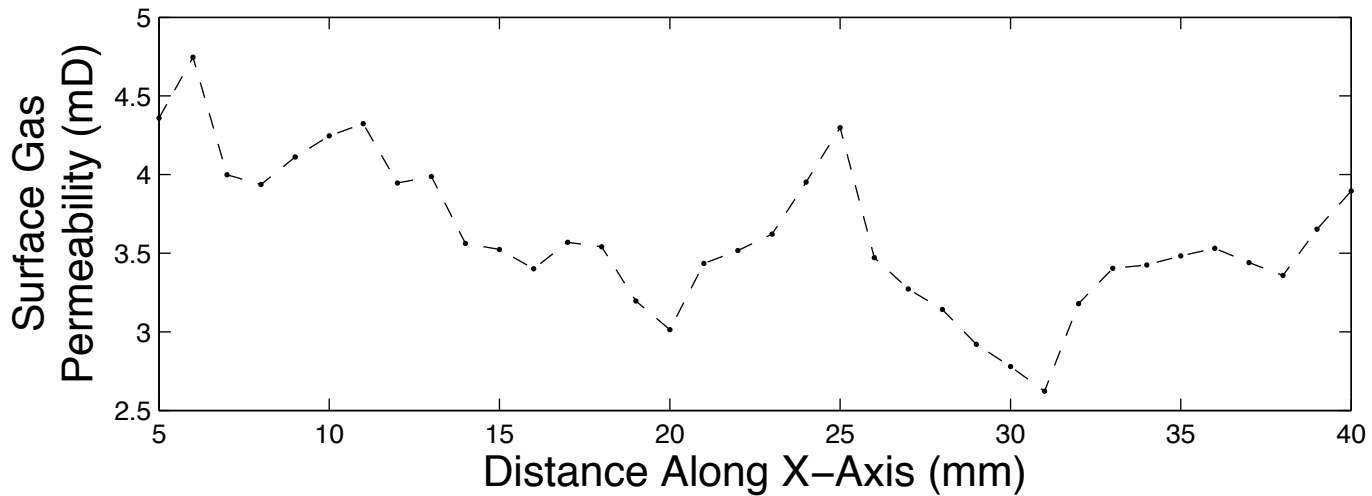


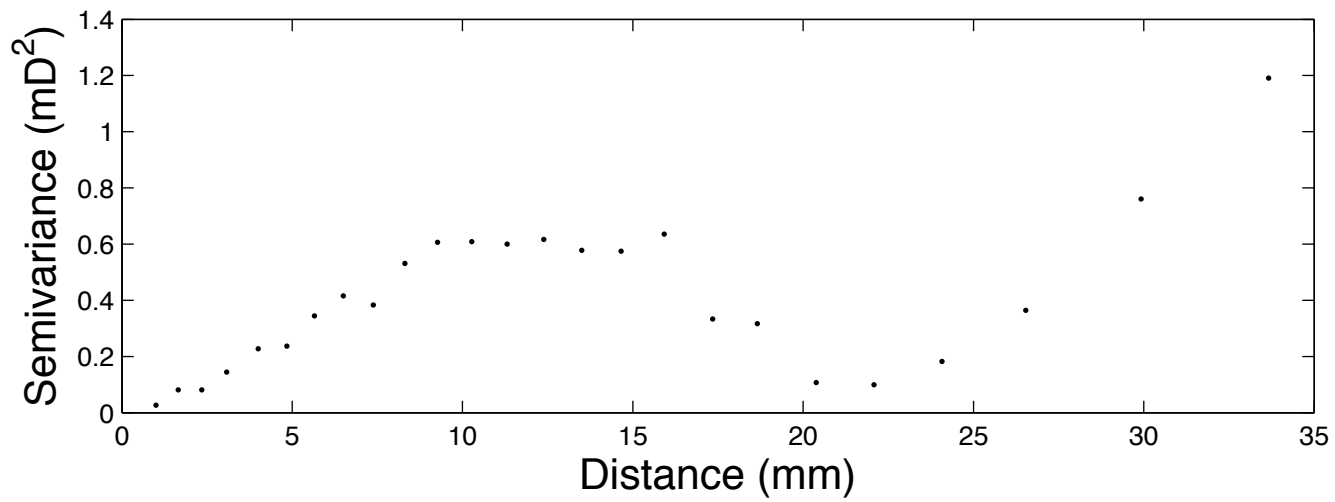
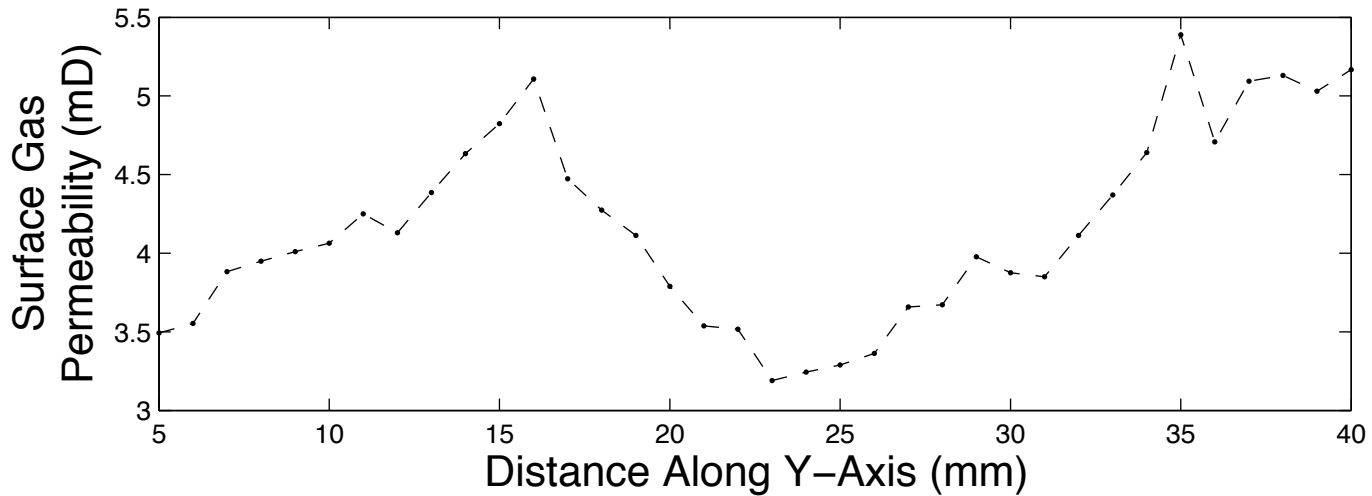


Portland Brownstone

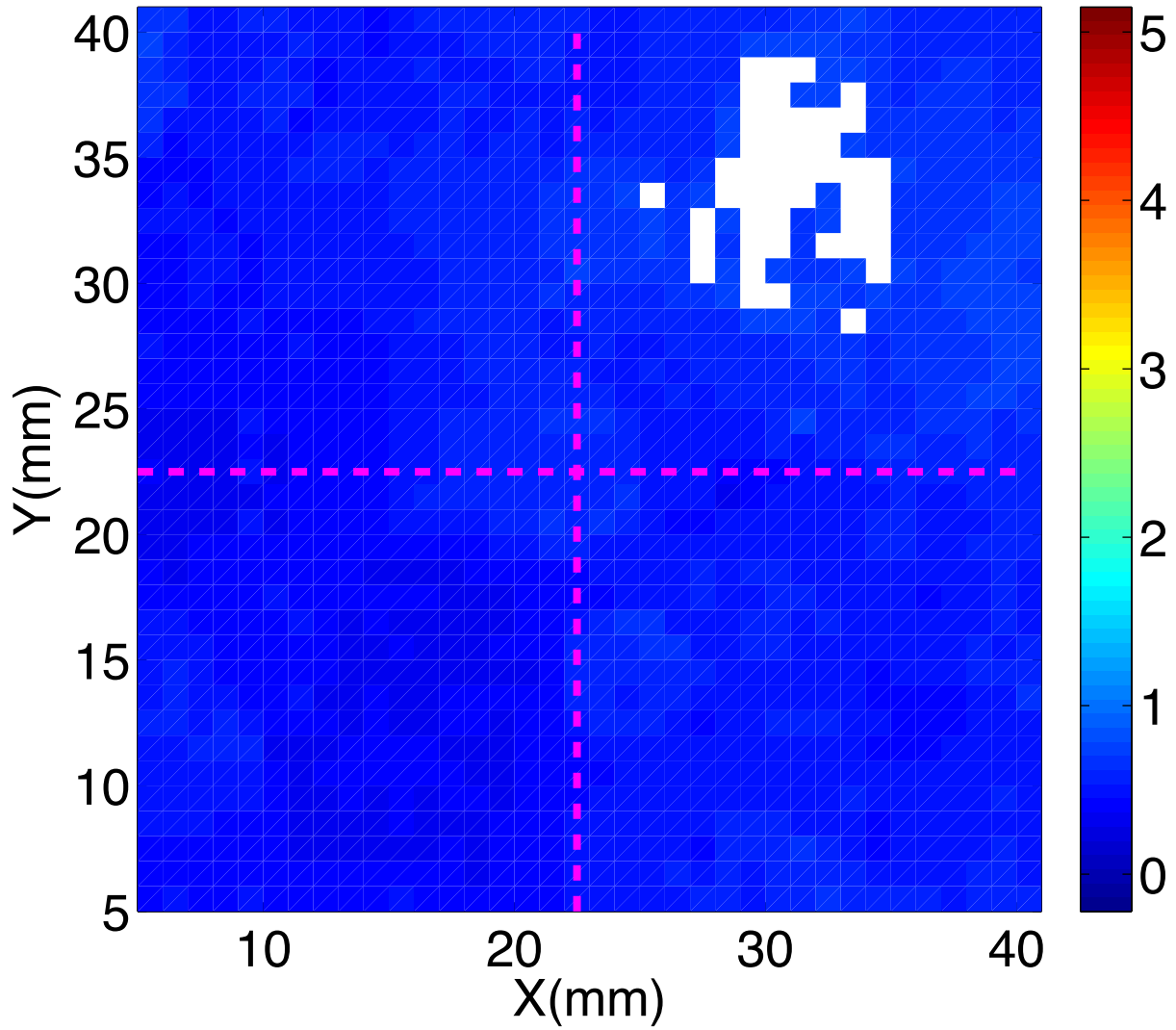


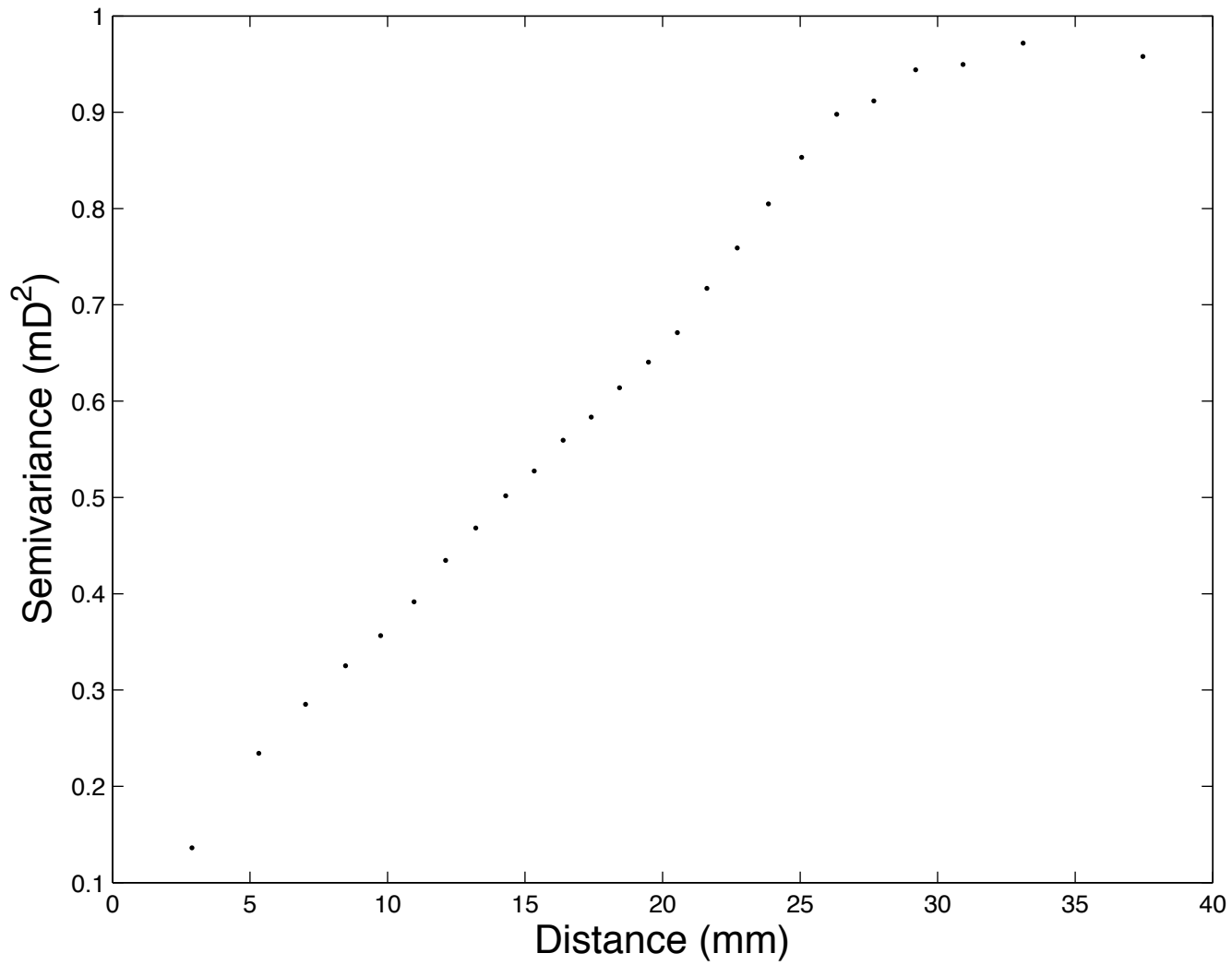


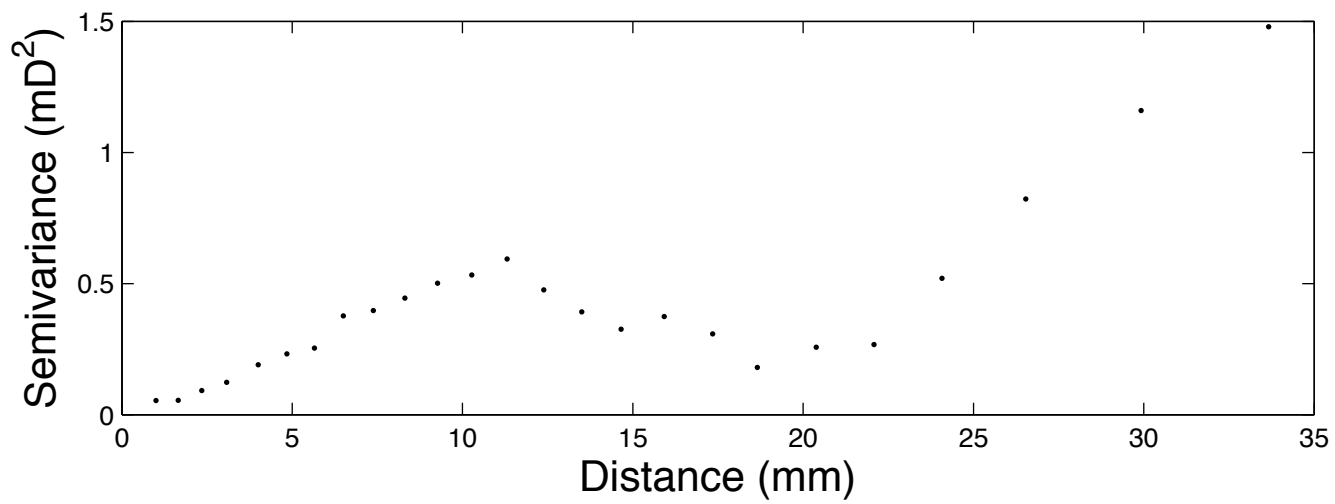
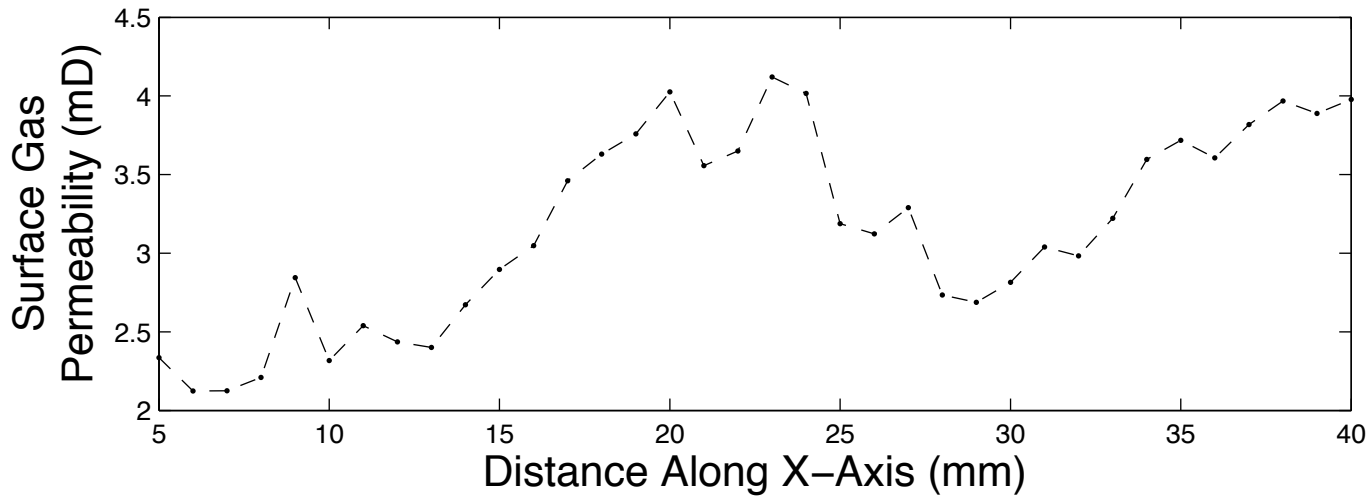


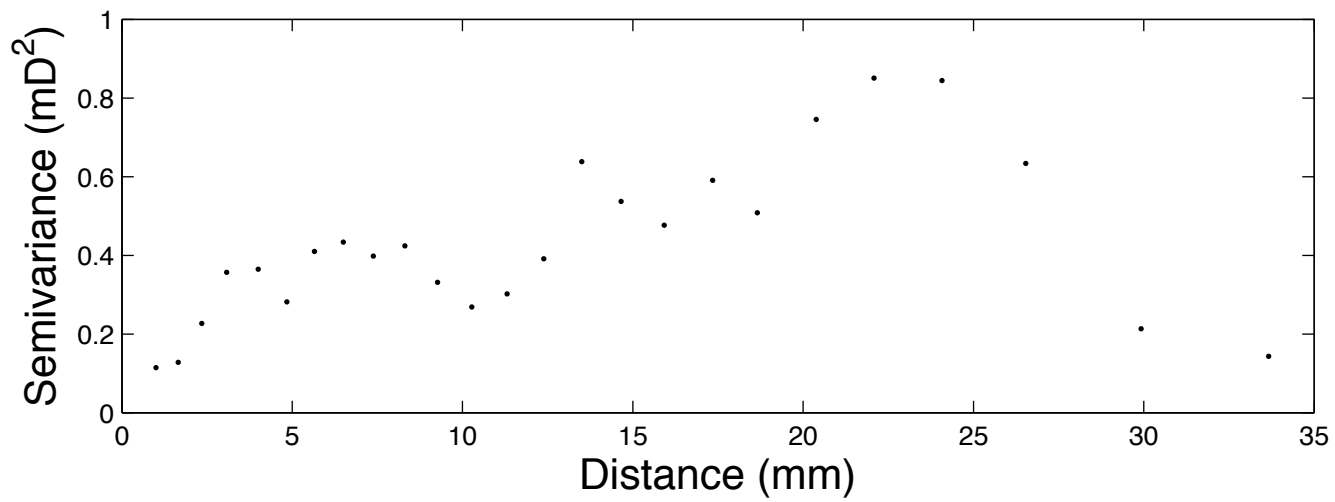
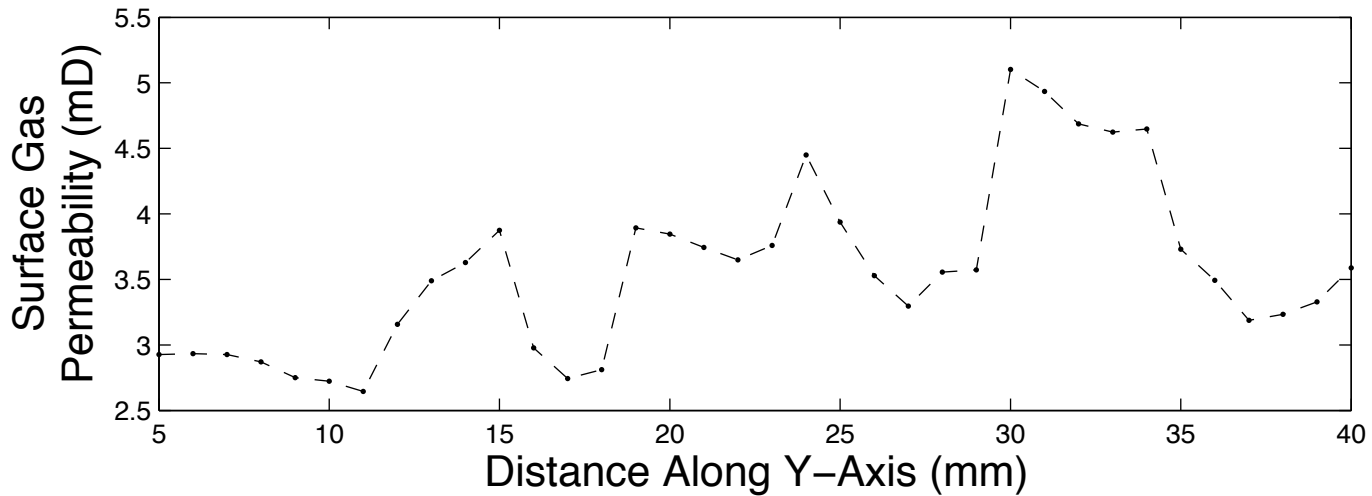


Red Clay Brick

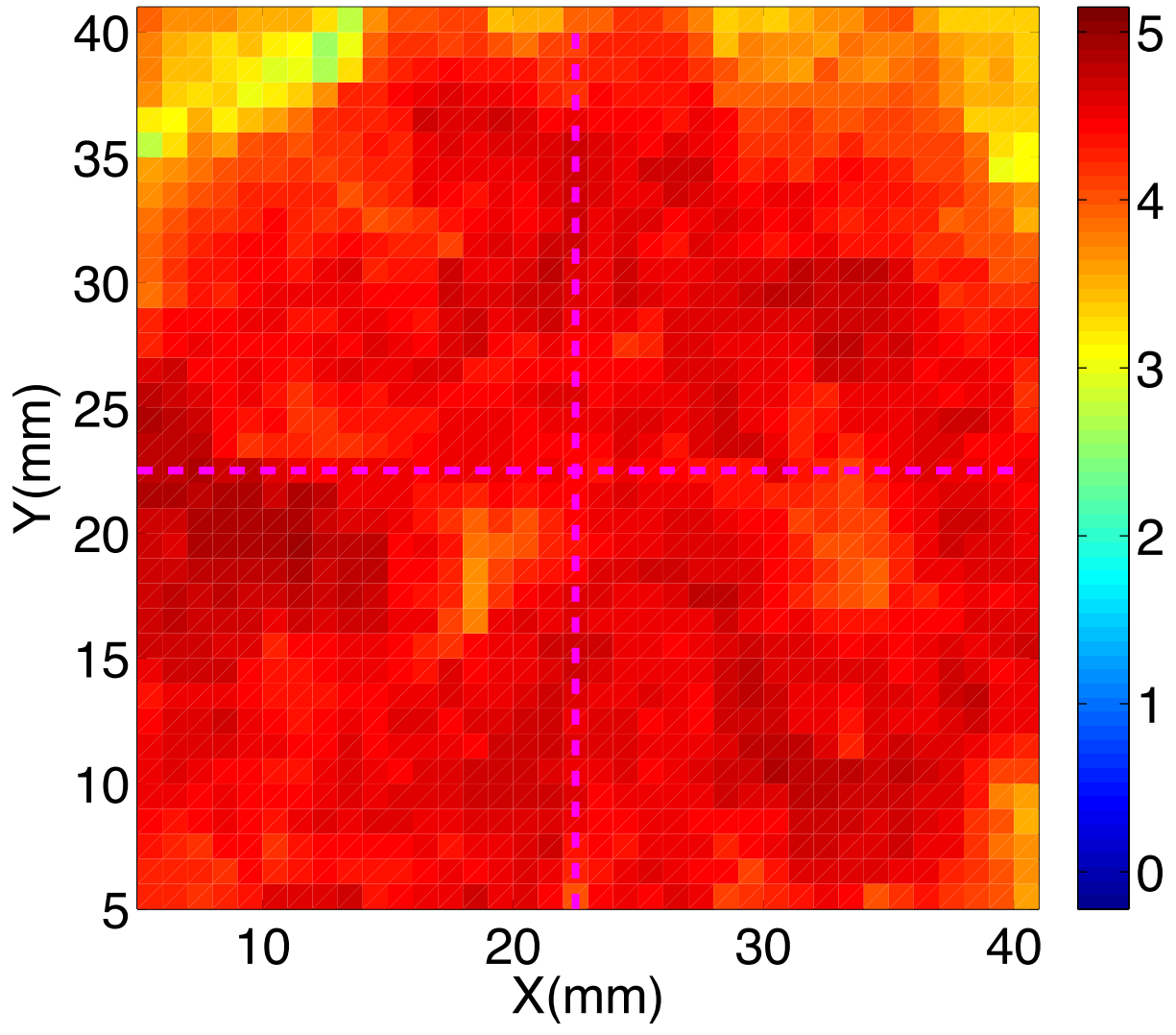


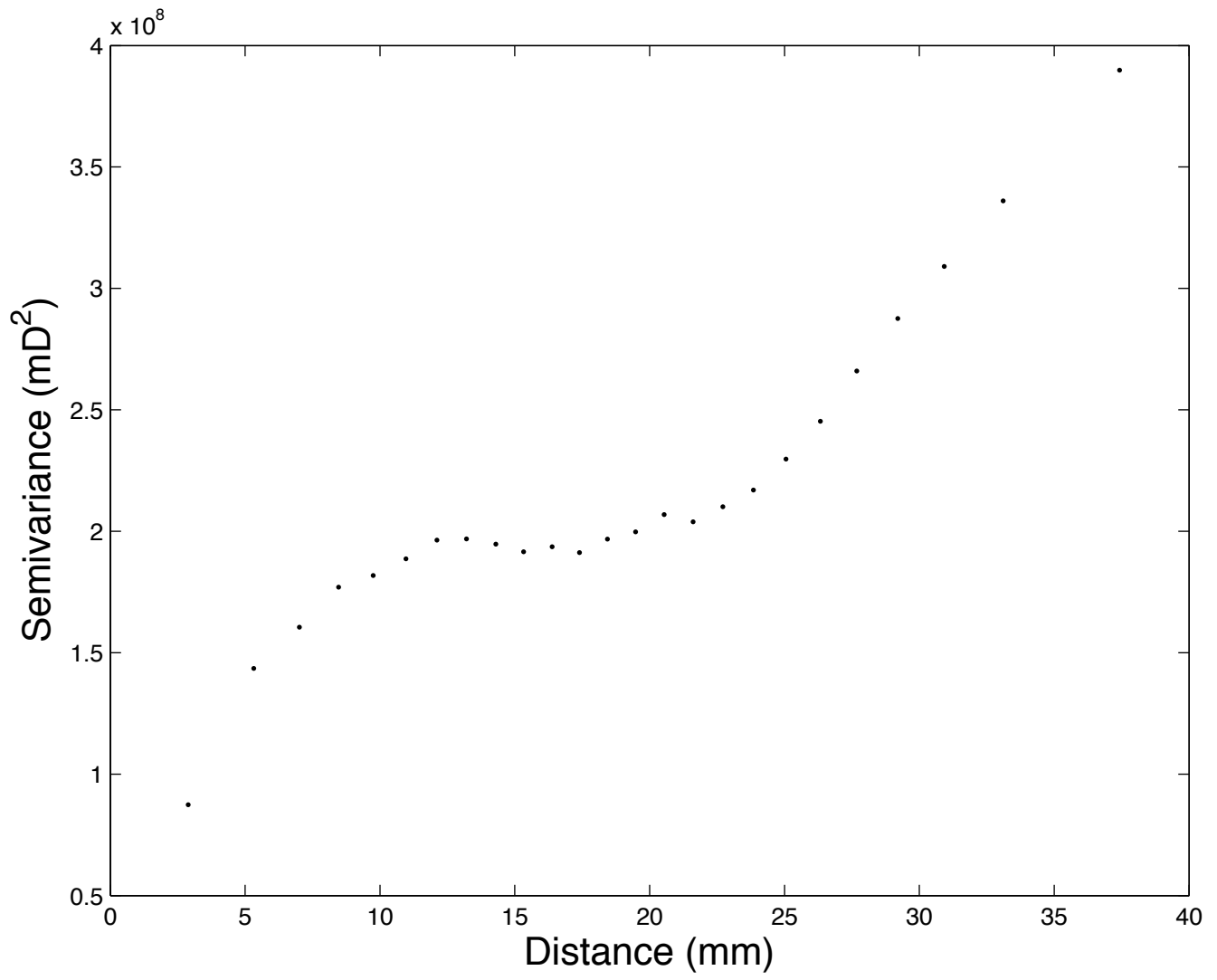


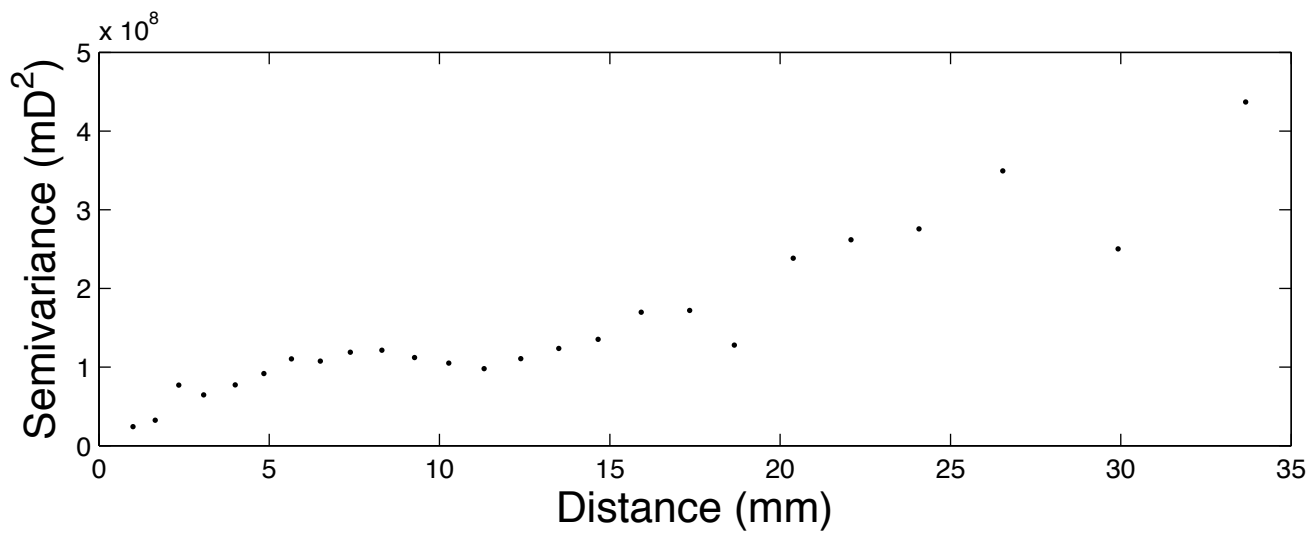
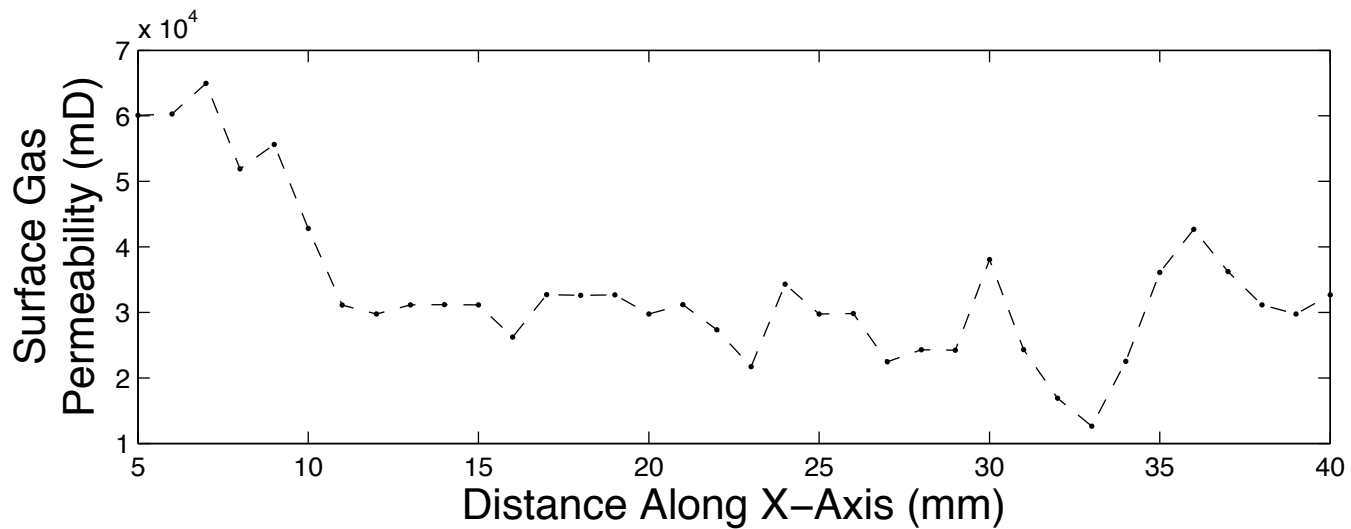


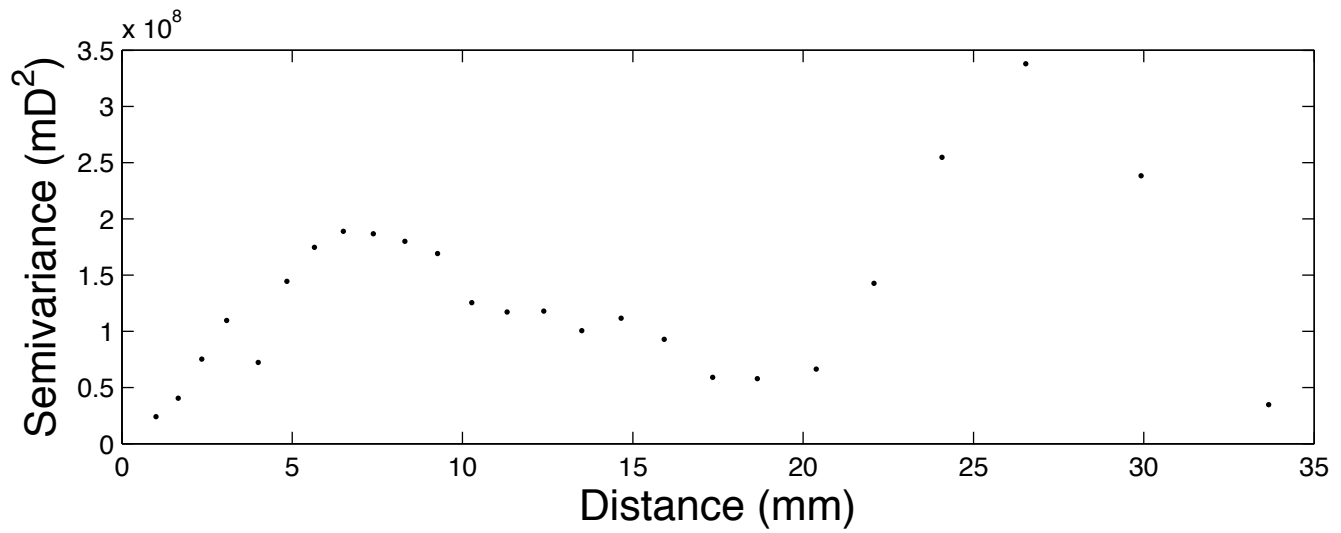
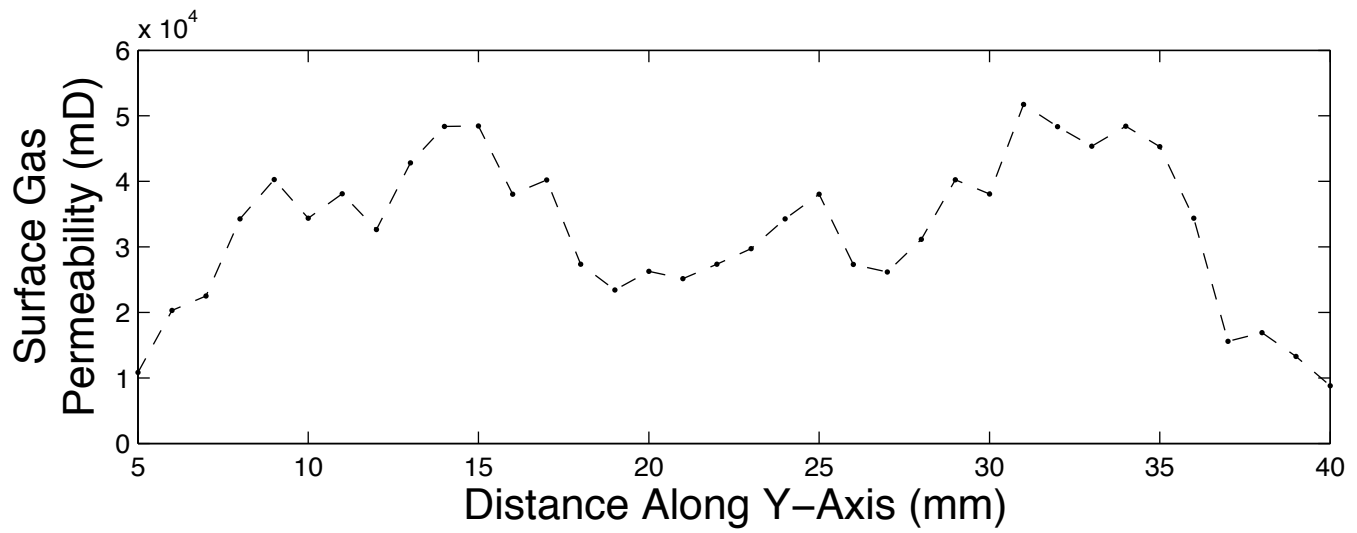


Red Colored Brick Paver

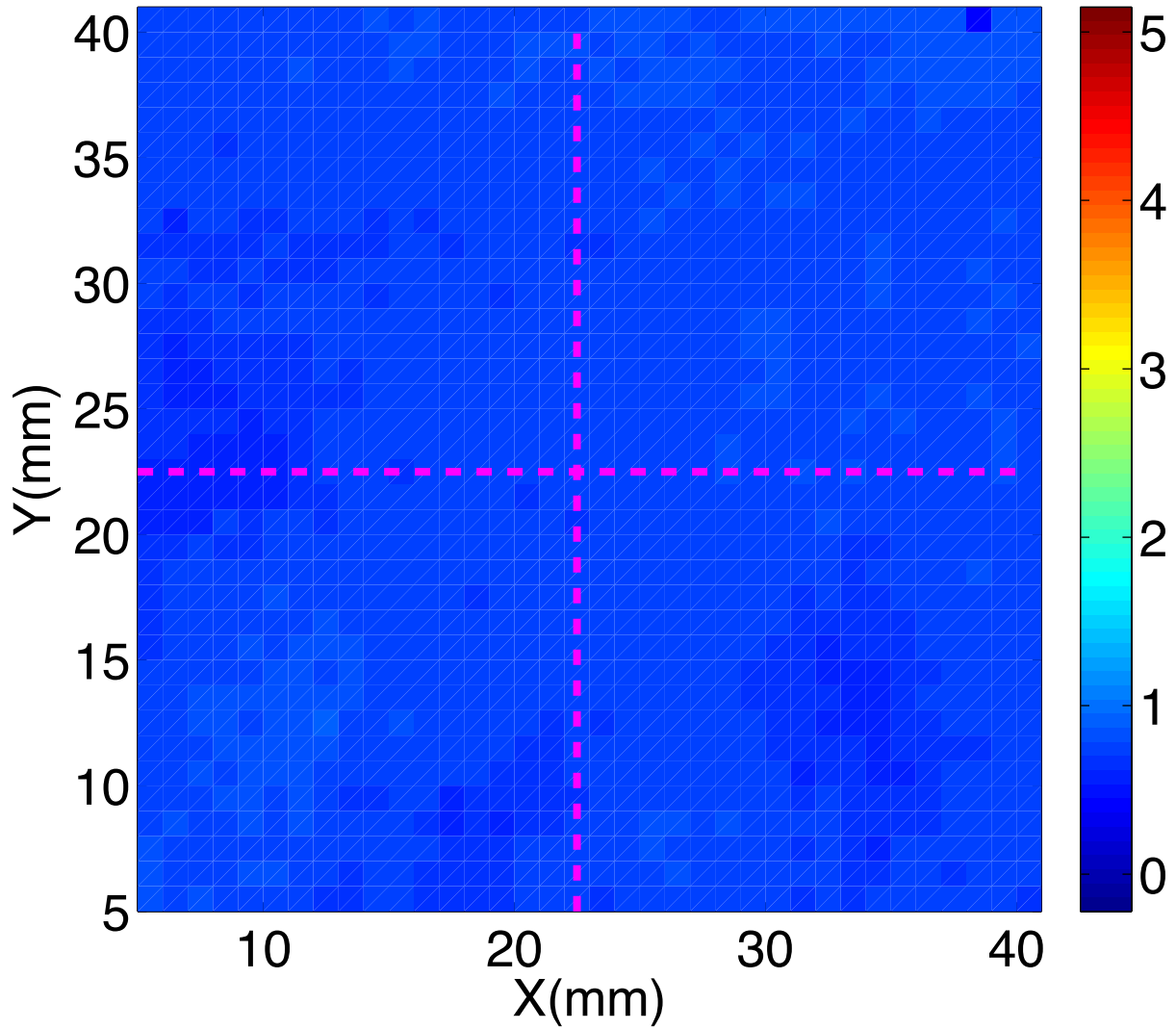


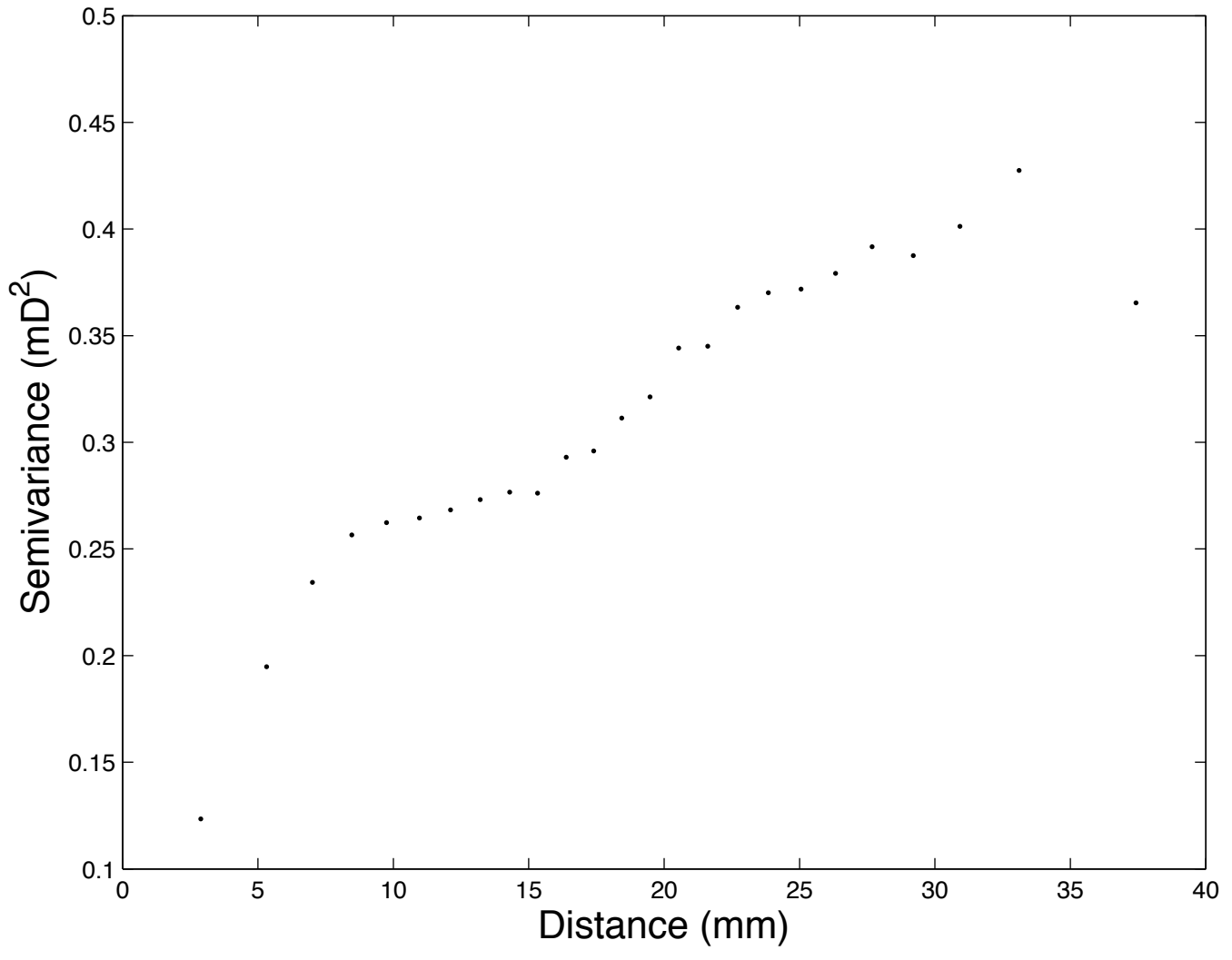


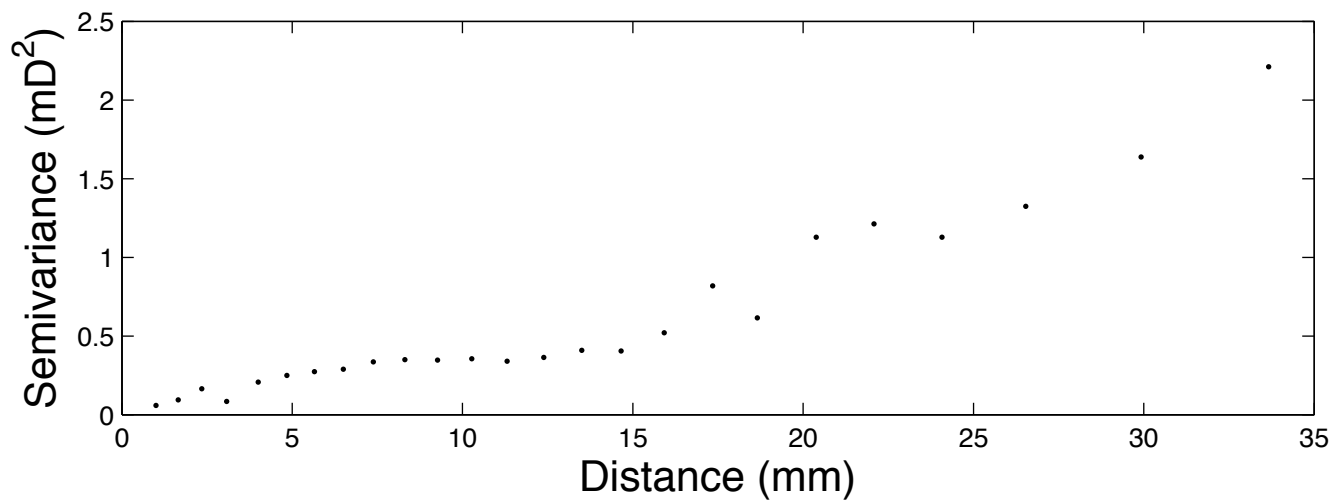
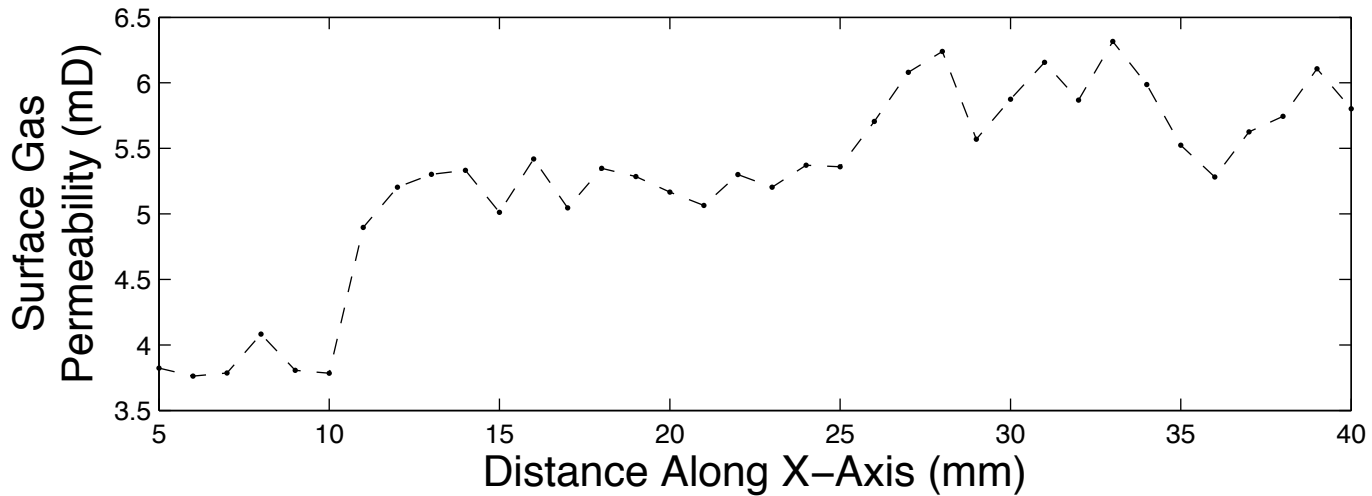


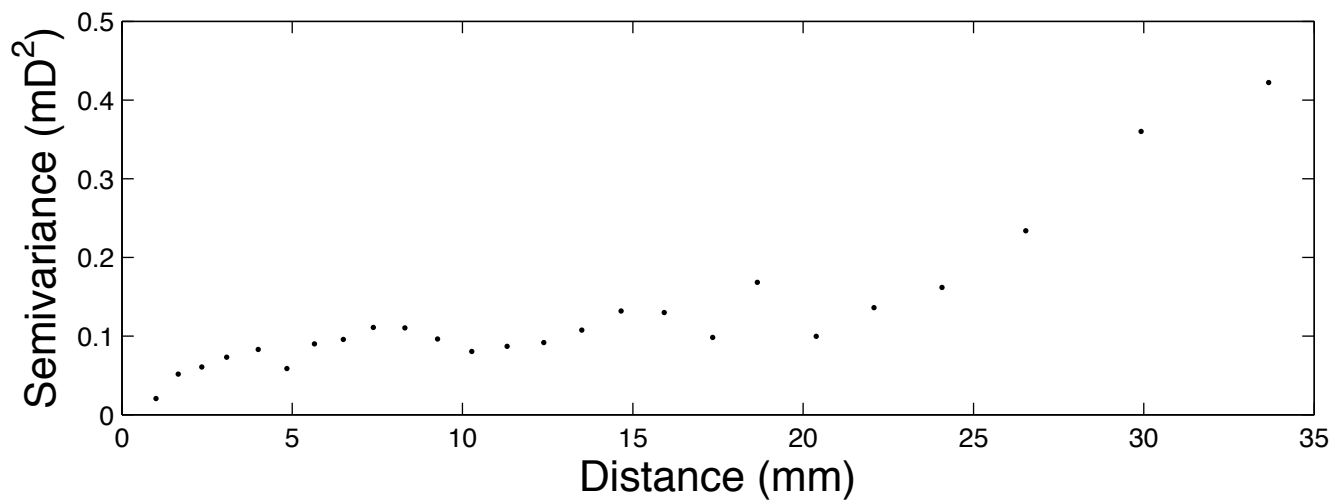
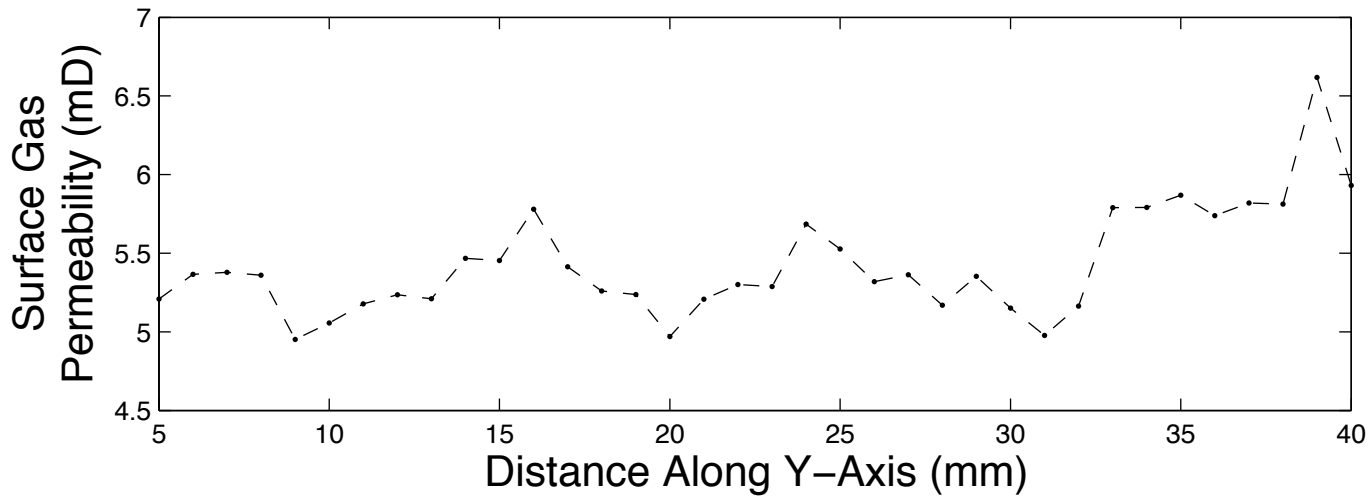


Silver Indiana Limestone









Tan Colored Brick Paver

